

COLLECTIVE ATOM-CAVITY INTERACTIONS IN A HIGH-FINESSE  
DUAL-WAVELENGTH CAVITY

A DISSERTATION  
SUBMITTED TO THE DEPARTMENT OF APPLIED PHYSICS  
AND THE COMMITTEE ON GRADUATE STUDIES  
OF STANFORD UNIVERSITY  
IN PARTIAL FULFILLMENT OF THE REQUIREMENTS  
FOR THE DEGREE OF  
DOCTOR OF PHILOSOPHY

Jongmin Lee  
August 2011

© 2011 by Jongmin Lee. All Rights Reserved.  
Re-distributed by Stanford University under license with the author.



This work is licensed under a Creative Commons Attribution-  
Noncommercial 3.0 United States License.  
<http://creativecommons.org/licenses/by-nc/3.0/us/>

This dissertation is online at: <http://purl.stanford.edu/hv723jp4713>

I certify that I have read this dissertation and that, in my opinion, it is fully adequate in scope and quality as a dissertation for the degree of Doctor of Philosophy.

**Mark Kasevich, Primary Adviser**

I certify that I have read this dissertation and that, in my opinion, it is fully adequate in scope and quality as a dissertation for the degree of Doctor of Philosophy.

**Hideo Mabuchi**

I certify that I have read this dissertation and that, in my opinion, it is fully adequate in scope and quality as a dissertation for the degree of Doctor of Philosophy.

**Jelena Vuckovic**

Approved for the Stanford University Committee on Graduate Studies.

**Patricia J. Gumpert, Vice Provost Graduate Education**

*This signature page was generated electronically upon submission of this dissertation in electronic format. An original signed hard copy of the signature page is on file in University Archives.*

# Abstract

We developed a high-finesse single-wavelength cavity with a large collective cooperativity to achieve pseudospin squeezing and study collective atom-cavity interactions. We observed collective normal mode splitting, providing evidence for a large collective cooperativity that can result in better spin-squeezing. We observed  $\sim 13$  dB large anti-spin-squeezing but little spin-squeezing because of the inhomogeneous atom-cavity coupling, limiting the atomic coherence.

In order to achieve identically coupled atoms to a cavity mode, we developed a high-finesse dual-wavelength cavity with a 1560 nm cavity lattice and a 780 nm cavity probe. Optically trapped atoms in the lattice are in-phase with the cavity probe at the cavity center, and we obtained spatially identical atom-cavity coupling.

We studied macroscopic self-trapping behavior of two hyperfine levels experimentally and theoretically, and in-phase atom registration in the dual-wavelength cavity enables us to treat the trapped atoms as one macroscopic ensemble of atoms. At the mid-point of a full Rabi oscillation, the collective atom-cavity interaction interrupts the coherent evolution of the macroscopic ensemble of atoms.

We demonstrated a free-running Raman laser in our cavity system using  $^{87}\text{Rb}$  atoms as the gain medium, which has atypical lasing threshold behavior and tunable gain properties. The intermode laser linewidth is as low as 80 Hz.

To all my family, all my mentors, and all my friends

# Acknowledgement

I am deeply appreciative of my advisor Mark Kasevich who showed me the world of atomic physics and led me to be an independent researcher; his scientific insight inspired me a lot. During my graduate days, I had a great opportunity to work with very talented and friendly project members. I am very thankful for all post-docs, graduate students, and visiting scholars. I learned many things from all of them, and I enjoyed sharing many ideas with them. I had also great memories of K-team about fun ski trips and group activities. I would like to thank to all current and former Kasevich group members. In addition, I was so pleased to discuss quantum optics with Mabuchi group members. Finally, I sincerely thank to my parents who encouraged me to be a solid scientist, and I heartily thank to my lovely wife who devoted herself to me and shared all my days in Stanford.

# Contents

<b>Abstract</b>	<b>iv</b>
<b>Acknowledgement</b>	<b>vi</b>
<b>1 Introduction</b>	<b>1</b>
<b>2 Background</b>	<b>5</b>
2.1 Cavity QED systems . . . . .	5
2.2 Spin-Squeezed State . . . . .	7
2.3 Macroscopic Self-Trapping . . . . .	16
2.4 Raman Lasing . . . . .	19
2.5 Conclusion . . . . .	26
<b>3 Cold Atoms in a Cavity</b>	<b>28</b>
3.1 Lasing Cooling and Trapping . . . . .	28
3.2 Cavity System . . . . .	32
3.3 Apparatus . . . . .	50
<b>4 Review and Motivation</b>	<b>55</b>
4.1 Collective Normal Mode Splitting . . . . .	55
4.2 Anti-Spin-Squeezing . . . . .	63
<b>5 Cavity QED System with Identically Coupled Atoms</b>	<b>71</b>
5.1 Introduction . . . . .	71
5.2 Identical Atom-Cavity Coupling . . . . .	75

5.3	Atomic Coherence Times . . . . .	77
5.4	Conclusion . . . . .	80
<b>6</b>	<b>Macroscopic Self-trapping</b>	<b>82</b>
6.1	Introduction . . . . .	82
6.2	Simulation . . . . .	83
6.3	Readout after or during the interaction . . . . .	90
6.4	Conclusion . . . . .	93
<b>7</b>	<b>Raman Laser</b>	<b>95</b>
7.1	Introduction . . . . .	95
7.2	Lasing Threshold . . . . .	98
7.3	Lasing Linewidth and Frequency Shift . . . . .	101
7.4	Semi-classical Model . . . . .	103
7.5	Conclusion . . . . .	106
<b>8</b>	<b>Conclusion</b>	<b>107</b>
<b>A</b>	<b>Cavity-lock servo circuits</b>	<b>109</b>
<b>Bibliography</b>		<b>112</b>

# List of Tables

3.1 Cavity parameters . . . . .	33
---------------------------------	----

# List of Figures

2.1	Cavity quantum electrodynamics . . . . .	6
2.2	Examples of cQED systems . . . . .	8
2.3	$^{87}\text{Rb}$ atom and its atomic clock state . . . . .	9
2.4	Coherent spin state and Spin-squeezed state . . . . .	9
2.5	Spin-squeezed state for atom interferometry . . . . .	10
2.6	Three-level atom model . . . . .	11
2.7	Macroscopic superposition state . . . . .	16
2.8	Rabi oscillation to self-trapping . . . . .	17
2.9	Coherence of macroscopic superposition state . . . . .	17
2.10	$\text{TEM}_{00}$ lasing mode . . . . .	20
2.11	Three level atom model of Raman lasing . . . . .	20
2.12	Lasing-induced ac Stark shift . . . . .	22
2.13	Lasing output vs. pump intensity . . . . .	23
2.14	Lasing output vs. two-photon detuning . . . . .	24
3.1	Optical molasses . . . . .	30
3.2	Magneto-optical trap . . . . .	32
3.3	Cavity design . . . . .	34
3.4	Cavity mode's waist . . . . .	35
3.5	Cavity chambers . . . . .	38
3.6	Pictures of cavity chambers . . . . .	39
3.7	Cavity tubes and mirror-ends . . . . .	39
3.8	Cavity ring-down and cavity spectrum . . . . .	41
3.9	Single- $\lambda$ cavity lock scheme with one master laser . . . . .	42

3.10	Injection lock . . . . .	43
3.11	Atom-induced cavity shift . . . . .	45
3.12	Dual- $\lambda$ cavity lock scheme with two master laser . . . . .	47
3.13	Dual- $\lambda$ cavity lock scheme with one master laser . . . . .	48
3.14	Compact laser system . . . . .	51
3.15	Control system . . . . .	52
3.16	Sensor hardware . . . . .	54
4.1	Normal mode splitting setup . . . . .	59
4.2	Normal mode splitting vs. atom number . . . . .	61
4.3	Normal mode splitting vs. detuning . . . . .	63
4.4	Anti-spin squeezing vs. microwave rotation angle . . . . .	67
4.5	Anti-spin-squeezing vs. atom number . . . . .	69
5.1	Dual-wavelength cavity setup . . . . .	74
5.2	In-phase and out-of-phase atom registration . . . . .	76
5.3	Lifetime and Coherence time of optically trapped atoms . . . . .	78
5.4	Differential ac Stark shift of two hyperfine ground state . . . . .	80
6.1	Macroscopic self-trapping setup . . . . .	84
6.2	Atom-cavity interaction vs. incident cavity photons . . . . .	87
6.3	Self-trapping and macroscopic superposition state . . . . .	88
6.4	Evolution of the collective atomic state and cavity photon state . . . . .	89
6.5	Macroscopic superposition state generation . . . . .	90
6.6	Atom-induced cavity shifts vs. the incident cavity power . . . . .	91
6.7	Readout after the atom-cavity interaction . . . . .	91
6.8	Readout during the atom-cavity interaction . . . . .	93
7.1	Raman lasing setup . . . . .	97
7.2	Effective atom number fit . . . . .	99
7.3	Lasing output vs. atom number, pump intensity . . . . .	100
7.4	Lasing profile vs. pump intensity . . . . .	100
7.5	Lasing Linewidth . . . . .	101

7.6	Lasing frequency shift vs. atom number . . . . .	102
7.7	Atypical lasing threshold . . . . .	104
A.1	Cavity-lock servo 1 . . . . .	110
A.2	Cavity-lock servo 2 . . . . .	111

# Chapter 1

## Introduction

This dissertation presents research on the collective atom-cavity interactions between many atoms and a cavity mode (1; 2; 3; 4; 5; 6). We demonstrated a many-atom-cavity system with a high-finesse single-wavelength cavity and studied collective normal mode splitting and spin-squeezing. To overcome spatially inhomogeneous atom-cavity coupling of the single-wavelength cavity, we developed a dual-wavelength many-atom-cavity system to trap atoms with a 1560nm cavity mode and probe atoms with a 780nm cavity mode. At the central region of the cavity, in-phase atom registration where atoms are localized at the maxima of the probe mode enables spatially identical atom-cavity coupling for sufficiently cold atoms, and the in-phase atom registration allows us to achieve macroscopic self-trapping behavior of two hyperfine levels due to the collective atom-cavity interaction. We also demonstrated a Raman laser with atypical threshold behavior using cold atoms as the gain medium.

In the process of measuring atoms, atomic shot noise always exists and introduces uncertainty in the result of the atomic state decision process. Reaching the atomic sub-shot noise limit will improve the precision of atomic clocks and atom interferometry (7; 8; 9; 10; 11; 12; 13; 14; 15; 16). For two-level atoms of atomic clock states, there are only two projectable states for atomic state decision. If the statistical uncertainty of the atomic state decision follows the binomial distribution for  $N$  atoms, the atomic state is called the coherent spin state (CSS). When we have all atoms in the ground state, a  $\frac{\pi}{2}$

microwave pulse transfers the atomic state to a coherent spin state. If the statistical uncertainty of atomic state decision is less than that of coherent spin states, the atomic state is referred to as a spin-squeezed state (SSS). Generally, a larger number of atoms results in a better signal-to-noise ratio in atomic sensors. Given the current state of technology, there are practical limits to the number of atoms. Hence, the spin-squeezed state could improve the sensitivity of atomic sensors with a finite atom number. We have used cavity-aided non-demolition measurement to generate this spin-squeezed state.

Nondemolition measurement of cold atoms (17), in particular, cavity-enhanced non-demolition measurement, is a promising method to generate atomic spin-squeezed states. Substantial sensitivity improvements can be achieved using the techniques developed in cQED (cavity quantum electrodynamics) (18; 19). Since an optical cavity increases optical depth, the degree of spin-squeezing in the cavity is larger than for free space atoms. Thus, benefiting from a high finesse as well as large numbers of atoms, a high finesse cavity with a large-enough mode volume overlapped with many atoms enables us to achieve a better spin-squeezing (5). In a high-finesse cavity, the collective atomic states couple with far-detuned and weak cavity photons. The detection of transmitted cavity photons affects the collective atomic state, and the uncertainty of the atom number difference between ground and excited states, i.e. two hyperfine states, is reduced by the conditional measurement process.

We implemented a high-finesse single-wavelength optical cavity for studying collective pseudospin squeezing of atomic clock states of  $^{87}\text{Rb}$  atoms because a more optical depth from a high cavity finesse and a proper cavity mode volume to overlap most of the atoms and have an appropriately strong collective atom-cavity coupling result in more spin squeezing; our cavity has a large collective cooperativity, which has the potential to generate better spin-squeezing. Using a 780 nm high-finesse hemispherical cavity and a spin-squeezing sequence, we observed 13 dB anti-spin-squeezing in the variance after rotating a spin-squeezed state by  $90^\circ$  along the collective spin vector, but we observed only a few dB of spin-squeezing in the variance (4). Spatially inhomogeneous atom-cavity coupling and inhomogeneous light shift resulted in a smaller degree of spin-squeezing than expected. Therefore, we built a high-finesse dual-wavelength cavity to overcome these limitations, and we demonstrated in-phase atom registration with a 1560 nm cavity optical lattice and a

780nm cavity probe (1). In the cavity, we can trap atoms in the cavity optical lattice, and we are able to probe atoms in-phase at the cavity center. This system has the potential to have a spatially identical atom-cavity coupling when regularly spaced atoms get in-phase with the probe at the dual-wavelength cavity center.

In cQED research (20; 21; 22; 23; 24; 25; 26; 27; 28; 29; 30; 31), identical atom-cavity coupling has been one of the primary issues in the study of light and matter interaction. In optical cQED, a standing wave cavity has been used for many delicate cQED experiments, but identical atom-cavity coupling cannot be realized in such a cavity because of the cavity nodes and anti-nodes of the standing wave cavity. In addition, the photon momentum transfer to the atoms prevents localization of all the atoms. A 780nm cavity probe and a 1560nm cavity lattice enable us to probe the trapped atoms homogeneously in each lattice site. Atoms at low enough temperatures can be registered homogeneously because the beam profile of the cavity probe and the distribution of trapped atoms are uniform in each lattice site. At the cavity center, we can have in-phase atom registration, in which the atoms are localized at the anti-nodes of the 1560nm lattice and are registered by the anti-nodes of the cavity probe. The in-phase atom registration with a spatially identical atom-cavity coupling is a unique property of our dual-wavelength cavity system, which allows us to extend cQED research to high degrees of spin-squeezed state generation and to macroscopic self-trapping of two hyperfine levels by collective atom-cavity interaction. This system also has the potential to implement cavity-aided atomic magnetometry and atomic thermometry and to improve the performance of cavity optomechanics.

The macroscopic self-trapped state of  $^{87}\text{Rb}$  atom's two hyperfine ground state was studied in our dual-wavelength high-finesse cavity (2). At the central region of the cavity, where MOT (magneto-optically trapped) atoms are trapped, the anti-node of the 780nm cavity probe gets in-phase with the 1560nm cavity lattice beam. Because of the spatially identical atom-cavity coupling, we can regard these regularly spaced atoms in the lattice as one macroscopic ensemble of atoms that interact with a cavity mode. When we set the cavity resonance at the mid-point of the full atom-induced cavity shifts, the collective atom-cavity interaction, i.e. the probe-induced ac Stark shift on the microwave transition, interrupts the collective Rabi oscillation of  $\sim 10^4$  trapped atoms between two hyperfine ground states at the mid-point of the full cavity shifts.

We also realized a continuous wave (CW) Raman laser using a MOT cloud of  $^{87}\text{Rb}$  atoms as the Raman gain medium at the central region of high-finesse standing wave cavity (3). Tunable Raman gain media properties in atomic systems, such as gain bandwidth, index of refraction or dispersion can be controlled precisely through variations in the pumping mechanism. Our Raman laser also operates in a regime where the effect of single atoms on the cavity field exists. This regime manifests itself with strong nonlinearities in the gain properties even at 100 pW lasing output levels. The nonlinearities result in an atypical lasing threshold behavior involving jumps in the lasing power. We experimentally determined the intrinsic half-width-half-maximum (HWHM) intermode linewidth of the laser to be 80 Hz.

The rest of this dissertation is organized as follows: Chapter 2 is devoted to the research background. Chapter 3 explains cold atoms and our cavity systems. Chapter 4 reviews the single-wavelength cavity experiments of the collective normal mode splitting and the anti-spin-squeezing. Chapter 5 discusses the identical atom-cavity coupling of the dual-wavelength cavity, and Chapter 6 discusses the macroscopic self-trapping of two hyperfine levels. Chapter 7 discusses the Raman lasing. Finally, Chapter 8 presents conclusions.

# Chapter 2

## Background

Our cavity QED research is mainly focused on the study of the collective atom-cavity interactions in a high finesse optical cavity; we studied spin-squeezing toward the Heisenberg limit, macroscopic self-trapping between two hyperfine levels, and Raman lasing with atypical lasing behavior. This chapter presents several types of cQED systems and the theoretical backgrounds of spin-squeezing, macroscopic self-trapping, and Raman lasing.

### 2.1 Cavity QED systems

The essential components for studying cavity QED systems (Fig. 2.1) are cavity photons, atoms, and a cavity. The cavity photons closely resonant to the atomic transition can interact with atoms in a cavity. The degree of the atom-cavity interaction is determined by atom-cavity coupling strength  $g$ . The coupling  $g$  is represented by  $g(\vec{r}) = g_0 \psi(\vec{r}) = \sqrt{\frac{\mu^2 \omega_c}{2\hbar\epsilon_0 V_m}} \psi(\vec{r})$ , where  $V_m = \int d^3x |\psi(\vec{r})|^2$  is the cavity mode volume;  $\mu = \langle e | \mu | g \rangle$ , dipole matrix element;  $\omega_c$ , cavity resonance frequency;  $\psi(\vec{r})$ , spatial component of cavity mode. Therefore, a smaller  $V_m$  and a bigger  $\mu$  increase  $g$ .

The cavity decay rate  $\kappa$  and atomic decay rate  $\gamma$  also affect the degree of an atom-cavity interaction. A smaller  $\kappa$ , i.e. a high cavity finesse  $F$ , results in a longer lifetime of cavity photons and a longer atom-cavity interaction time;  $\kappa = \frac{\Delta v_{\text{fsr}}}{2F} = \frac{\pi c}{2FL_{cav}}$ , where  $L_{cav}$  is a cavity length. A smaller  $\gamma$  means a longer lifetime of excited state atoms and a longer atomic coherence;  $2\gamma = \Gamma = \frac{\omega_A^3 |\mu|^2}{3\pi c^3 \epsilon_0 \hbar}$ , where  $\omega_A$  is the atomic resonance frequency.

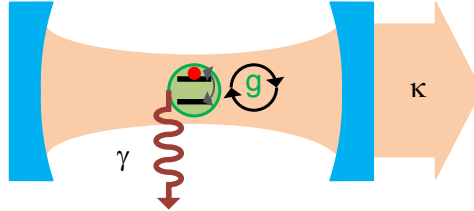


Figure 2.1: Cavity quantum electrodynamics (cQED) study atom-cavity interaction:  $g$  is the atom-cavity coupling strength;  $\kappa$ , cavity decay rate;  $\gamma$ , atomic decay rate. The Hamiltonian of a cavity field and two-level atoms can be described as  $\hat{\mathcal{H}} = \hbar\omega_c \hat{a}^\dagger \hat{a} + \frac{1}{2}\hbar\omega_a \sum_{i=1}^{N_{at}} \hat{\sigma}_{z,i} + \sum_{i=1}^{N_{at}} g(\vec{r})(\hat{a}^\dagger \hat{\sigma}_{-,i} + \hat{\sigma}_{+,i} \hat{a})$ , where  $\hat{\sigma}_+ = |e\rangle\langle g|$  and  $\hat{\sigma}_- = |g\rangle\langle e|$  are the raising and lowering operators of two-level atoms' optical transition,  $\hat{\sigma}_z = |e\rangle\langle e| - |g\rangle\langle g|$ , and  $\hat{a}^\dagger$  and  $\hat{a}$  are the creation and annihilation operators of cavity photons. The first and second terms are the cavity photon energy and the two-level atoms' energy, respectively. The third term is the atom-cavity interaction term.

Therefore, the cQED regime of  $\frac{g^2}{2\kappa\gamma} \gg 1$  has a strong atom-cavity interaction, which is called the (single-atom) strong coupling regime; a high cavity finesse with a small cavity mode volume is required to achieve this regime. For many  $N$  atoms, the cQED regime of  $\frac{Ng^2}{2\kappa\gamma} \gg 1$  (but  $\frac{g^2}{2\kappa\gamma} \lesssim 1$ ) has a strong collective atom-cavity interaction, which is called the collective strong coupling regime; a high cavity finesse with a properly large cavity mode volume is necessary to couple with many atoms. Those coupling regimes can be proved by the normal mode splitting of atom-cavity dressed states, which occurs when the cavity probe closely resonant to the atomic transition. In the single-atom strong coupling regime, the uncoupled system consists of one ground state atom with  $n + 1$  photons and one excited state atom with  $n$  photons. The atom-cavity dressed state can generate normal mode splitting according to the cavity photon number in the detection of fluorescence and cavity transmission. In the regime of the collective strong coupling regime, the uncoupled system consists of all  $N$  ground state atoms with one photon state and  $N - 1$  ground state atoms with zero photon state and one excited state atom. Many-atom-cavity dressed states result in collective normal mode splitting according to the atom number in the detection of fluorescence and cavity transmission.

Several types of the cQED system (Fig. 2.2) have been studied in the above coupling regimes. The ultra-high-Q optical cavity and alkali atoms have been used for studying single-atom strong coupling regime (Fig. 2.2(a), Kimble and Mabuchi groups). Quantum-mechanical cavity photon states have been realized using a sc (super-conducting) microwave Fabry-Perot cavity with a dispersively coupled Rydberg state atomic probe (Fig. 2.2(b), Raymond and Haroche groups). A microwave circuit cQED system has been demonstrated using sc microwave circuit cavity coupled to sc Qubits (Fig. 2.2(c), Schoelkopf group). A micro-post cQED system with quantum dots has been realized for a single photon generation (Fig. 2.2(d), Yamamoto group). Finally, photonic cQED system with quantum dots has been studied (Fig. 2.2(e), Scherer and Vuckovic groups). Especially, circuit cQED and solid state cQED systems have good scalability, and those systems can be mass-produced for quantum information science (32; 33; 34; 35; 36; 37).

However, artificial atoms are not a good reference for precision measurements because fabrication processes for artificial atoms such as sc Qubits and quantum dots tend not to result in identical artificial atoms. Precision measurement applications have therefore used neutral atoms, which not only have homogeneous characteristics but whose two hyperfine ground states have very long coherence time. Furthermore, laser cooled atoms are operated at room temperature.

## 2.2 Spin-Squeezed State

The main goal of this research was to improve the precision of atomic clocks and atom interferometers, whose signal-to-noise ratio increases as atom number increases, but for which it is technically hard to obtain a large number of atoms and probe many atoms uniformly. Spin-squeezing with cavity-aided nondemolition atom measurement is an excellent way of improving the precision of atomic sensors without increasing the atom number by generating entanglement between atoms.

We regard two hyperfine ground states as two-levels of atoms, and in an optical Bloch sphere atoms in the  $|F = 2, m_F = 0\rangle$  state and atoms in the  $|F = 1, m_F = 0\rangle$  state are

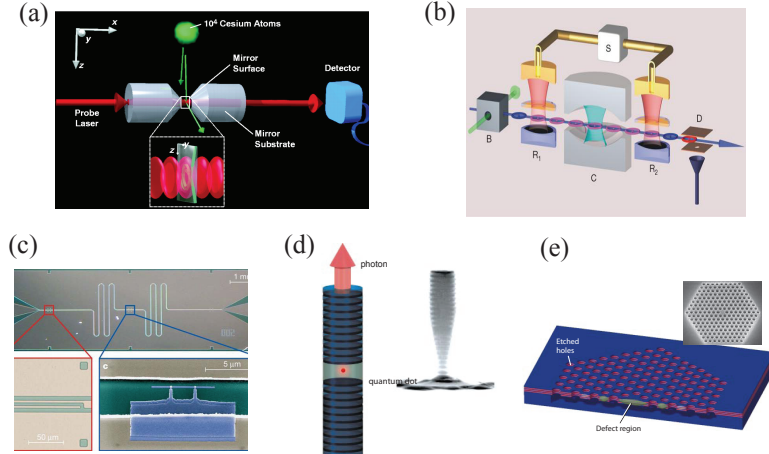


Figure 2.2: Examples of cQED systems. (a) Optical cQED system with alkali atoms (38). (b) Microwave cQED system (sc microwave Fabry-Perot cavity) with Rydberg state atomic probes (39). (c) Microwave sc circuit cQED with sc Qubits (40). (d) Micro-post cQED system with quantum dots (41). (e) Photonic crystal cQED system with quantum dots (42).

regarded simply as an excited state atom  $|2\rangle$  and a ground state atom  $|1\rangle$ , respectively (Fig. 2.3).

Coherent spin state (Fig. 2.4 (a)) is the shot-noise limited and minimum-uncertainty state. We can produce the coherent spin state when a  $\frac{\pi}{2}$  microwave pulse transfers all ground-state atoms to the state. The statistical uncertainty of the state decision process of the coherent spin state follows the binomial distribution.

Spin-squeezed state (Fig. 2.4 (b)) is the sub-shot-noise limited state where the uncertainty distribution of one axis is lower than the shot-noise limit. In order to generate the spin-squeezed state, we need atom-cavity coupling by means of an interaction Hamiltonian ( $\hat{\mathcal{H}}_{int}$ ). The cavity-aided dispersive measurement of many atoms affects the collective atomic state to be the spin-squeezed state. Because of the Heisenberg uncertainty principle ( $\Delta\hat{J}_y\Delta\hat{J}_z \geq \frac{1}{2}|\langle\hat{J}_x\rangle|$ ), the reduced uncertainty of the atom number direction ( $\hat{J}_z$ ) results in increased uncertainty in the phase direction ( $\hat{J}_y$ ).

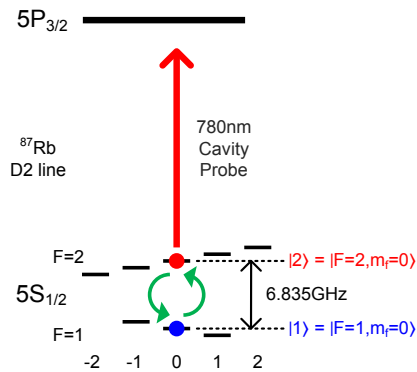


Figure 2.3:  $^{87}\text{Rb}$  atom and its atomic clock state; an excited state atom  $|2\rangle = |F = 2, m_f = 0\rangle$ , a ground-state atom  $|1\rangle = |F = 1, m_f = 0\rangle$  (43).

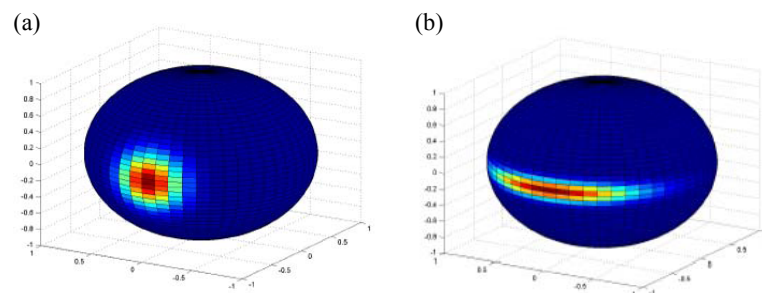


Figure 2.4: (a) Coherent spin state in the optical Bloch sphere. (b) Spin-squeezed state in the optical Bloch sphere.

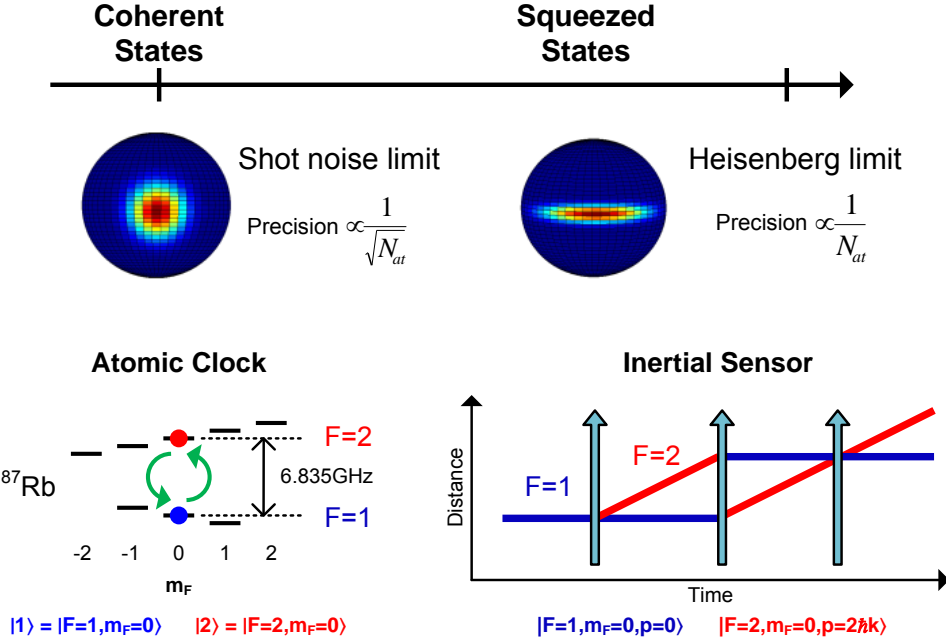


Figure 2.5: Spin-squeezed state for atom interferometry.

The measurement precision of the maximally spin-squeezed state at the Heisenberg limit (Fig. 2.5 (a)) corresponds to  $\frac{1}{N}$ , where  $N$  is the atom number; the uncertainty of spin-squeezed state is  $\frac{1}{N} < \delta N_{sss} < \frac{1}{\sqrt{N}}$ . The measurement precision of coherent spin states at the shot-noise limit corresponds to  $\frac{1}{\sqrt{N}}$  ( $\delta N_{css} = \frac{1}{\sqrt{N}}$ ). In the case of atomic clocks or atom interferometers (44), if we add a squeezing stage during the initial state preparation, we can improve the precision of atomic sensors (Fig. 2.5 (b)).

The degree of spin-squeezing with a cavity-aided nondemolition measurement is increased by coherently scattered photons into a cavity and is decreased by spontaneously emitted photons into free space per atom, and the squeezing factor is determined by collective cooperativity  $C$  as  $\frac{(\delta N)^2}{N} \geq \frac{2}{\sqrt{C}}$ . Based on the above inequality, better spin-squeezing results from a large collective cooperativity which requires a large number of atoms, a high cavity finesse, an optimal mode volume both for strong atom-cavity coupling and for homogeneous coupling to many atoms.

For a high degree of spin-squeezing, we need an appropriately high number of coherently scattered photons because more coherently scattered photons increase the number

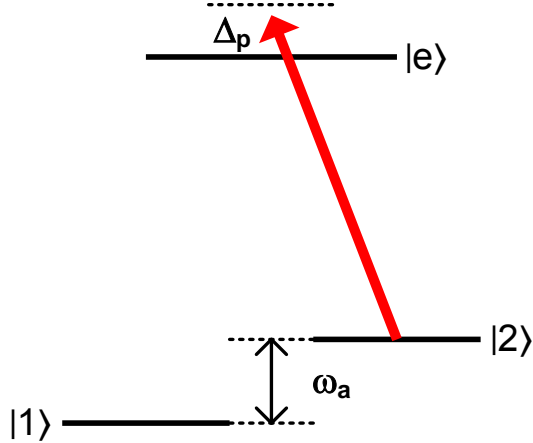


Figure 2.6: Simplified three-level atom model; two hyperfine ground states are  $|1\rangle = |F = 1, m_F = 0\rangle$  and  $|2\rangle = |F = 2, m_F = 0\rangle$  where  $\omega_a$  is the frequency difference between two hyperfine ground states. A cavity probe detuning is  $\Delta_p$  ( $\Delta_p > 0$ : blue-detuned from  $|e\rangle = |F' = 3\rangle$ ).

of spontaneously emitted photons. The spontaneously scattered photons into free space collapse the coherent superposition atomic state from  $N$  atoms to  $N - 1$  atoms and decrease the size of the collective spin vector, which lessens spin-squeezing and raises atomic projection noise. In addition, the spatially inhomogeneous atom-cavity coupling leads to inhomogeneous broadening that limits atomic coherence and decreases the spin-squeezing; this inhomogeneity also increases as the cavity photon increases.

In the spin-squeezing experiment, the initially prepared coherent spin state is coupled to the cavity photons by the interaction Hamiltonian  $\hat{\mathcal{H}}_{int}$ , and the detection process of transmitted cavity photons turns the coherent spin state into the conditional spin squeezed state by quantum measurement theory.

We studied the spin-squeezed state with a simplified three-level atom model (Fig. 2.6). We also assume that all atoms are equally coupled to the resonator, with a single-photon Rabi frequency  $g$ . For a single atom and setting  $\hbar = 1$ , the Hamiltonian of our system is as follows:

$$\begin{aligned}\hat{\mathcal{H}} = & \omega_c \hat{a}^\dagger \hat{a} + \omega_e |e\rangle\langle e| + \omega_1 |1\rangle\langle 1| + \omega_2 |2\rangle\langle 2| \\ & + g(e^{-i\omega_c t} \hat{a}^\dagger \hat{\sigma}_{2e} + h.c.) + g(e^{-i\omega_c t} \hat{a}^\dagger \hat{\sigma}_{1e} + h.c.) \\ & \Omega_{\mu w} (\hat{\sigma}_{12} e^{-i\omega_a t} + \hat{\sigma}_{21} e^{i\omega_a t}) + i\mathcal{E}(e^{-i\omega_d t} \hat{a}^\dagger - \hat{a} e^{i\omega_d t}),\end{aligned}\quad (2.1)$$

where  $\hat{\sigma}_{2e} = |2\rangle\langle e|$ ,  $\hat{\sigma}_{1e} = |1\rangle\langle e|$ ;  $\hat{a}^\dagger$  and  $\hat{a}$  are the creation and annihilation operators of cavity photons. In the first line, the first term is the cavity field ( $\omega_c$ ), and the second term is the free evolution of atomic excited state ( $\omega_e$  for  $|F' = 3\rangle$ ). The third and fourth terms are the free evolution of hyperfine ground state ( $\omega_1$  for  $|F = 1, m_F = 0\rangle$ ,  $\omega_2$  for  $|F = 2, m_F = 0\rangle$ ). The second line is the atom-cavity interaction terms. In the third line, the first term is the microwave driving field with  $\omega_a$  for Rabi oscillation, and the second term is the cavity driving field with  $\omega_d$ . Including cavity decay and atomic decay, we can describe our master equation as follows:

$$\dot{\hat{\rho}} = -i[\hat{\mathcal{H}}, \hat{\rho}] + 2\kappa\hat{\mathcal{D}}[\hat{a}]\hat{\rho} + 2\gamma_\perp\hat{\mathcal{D}}[\hat{\sigma}_{1e}]\hat{\rho} + 2\gamma_\perp\hat{\mathcal{D}}[\hat{\sigma}_{2e}]\hat{\rho}. \quad (2.2)$$

We simplify our system with transformation to a rotating frame and adiabatic elimination of the excited state (45). First, the transferred frame rotating at a frequency  $\omega_d$  with the state of  $|2\rangle\langle 2|$  as zero energy results in the following Hamiltonian:

$$\begin{aligned}\hat{\mathcal{H}}' = & -\Delta\hat{a}^\dagger \hat{a} - \Delta_e |e\rangle\langle e| - \omega_a |1\rangle\langle 1| + i\mathcal{E}(\hat{a}^\dagger - \hat{a}) \\ & + g(e^{i\Delta t} \hat{a}^\dagger \hat{\sigma}_{2e} + h.c.) + g(e^{i\Delta t} \hat{a}^\dagger \hat{\sigma}_{1e} + h.c.) \\ & \Omega_{\mu w} (\hat{\sigma}_{12} e^{-i\omega_a t} + \hat{\sigma}_{21} e^{i\omega_a t}),\end{aligned}\quad (2.3)$$

where  $\Delta = \omega_d - \omega_c$ ,  $\Delta_e = \omega_d - \omega_e$ , and  $\omega_a = \omega_2 - \omega_1 = 2\pi \cdot 6.835 \text{ GHz}$ . Second, in the case of a far-detuned weak cavity probe, we can adiabatically eliminate the excited state for the dynamics in the two ground states because we have a large detuning  $|\Delta_p| \gg \kappa, g, \gamma_\perp$  and a sufficiently low intracavity photon number. We are interested in effects of the light shift and not in populating the excited state.

$$\begin{aligned}\hat{\mathcal{H}}'' = & -\Delta\hat{a}^\dagger \hat{a} - \omega_a |1\rangle\langle 1| + i\mathcal{E}(\hat{a}^\dagger - \hat{a}) \\ & + \frac{g^2}{\Delta_p} \hat{a}^\dagger \hat{a} |2\rangle\langle 2| + \frac{g^2}{(\Delta_p - \omega_a)} \hat{a}^\dagger \hat{a} |1\rangle\langle 1| \\ & \Omega_{\mu w} (\hat{\sigma}_{12} e^{-i\omega_a t} + \hat{\sigma}_{21} e^{i\omega_a t}),\end{aligned}\quad (2.4)$$

where  $\Delta_p = \omega_c - \omega_e = \Delta_e - \Delta$ . With a transferred frame rotating at a microwave transition frequency  $\omega_a$ , we have the following Hamiltonian:

$$\hat{\mathcal{H}}''' = -\Delta\hat{a}^\dagger\hat{a} + i\mathcal{E}(\hat{a}^\dagger - \hat{a}) + \frac{g^2}{\Delta_p}\hat{a}^\dagger\hat{a}|2\rangle\langle 2| + \frac{g^2}{(\Delta_p - \omega_a)}\hat{a}^\dagger\hat{a}|1\rangle\langle 1| + \Omega_{\mu w}(\hat{\sigma}_{12} + \hat{\sigma}_{21}), \quad (2.5)$$

where  $\hat{\sigma}_z = |2\rangle\langle 2| - |1\rangle\langle 1|$ . The microwave term is only used for preparing an initial coherent spin state, which  $\frac{\pi}{2}$  pulse drives all atoms in a ground state  $\prod_{i=1}^N|1\rangle_i$  to be a coherent spin state. After the preparation of the coherent spin state, the Hamiltonian of spin-squeezing does not need the microwave term, and it can be simplified using  $\hat{\sigma}_z$  as follows:

$$\hat{\mathcal{H}}''' = -\Delta\hat{a}^\dagger\hat{a} + 0 \cdot \hat{\sigma}_z + i\mathcal{E}(\hat{a}^\dagger - \hat{a}) + g^2\hat{a}^\dagger\hat{a}\mathbb{I}\left(\frac{1}{\Delta_p} + \frac{1}{\Delta_p - \omega_a}\right) + g^2\hat{a}^\dagger\hat{a}\hat{\sigma}_z\left(\frac{1}{\Delta_p} - \frac{1}{\Delta_p - \omega_a}\right), \quad (2.6)$$

For  $N$  atoms,

$$\hat{\mathcal{H}}_N = -(\Delta - \delta_0)\hat{a}^\dagger\hat{a} + 0 \cdot \sum_{i=1}^N \hat{\sigma}_{z,i} + i\mathcal{E}(\hat{a}^\dagger - \hat{a}) + g^2\hat{a}^\dagger\hat{a}\sum_{i=1}^N \hat{\sigma}_{z,i}\left(\frac{1}{\Delta_p} - \frac{1}{\Delta_p - \omega_a}\right), \quad (2.7)$$

where  $\delta_0$  is  $\left(\frac{Ng^2}{\Delta_p} + \frac{Ng^2}{\Delta_p - \omega_a}\right)$ , and  $N$  is an atom number.

Our system has non-radiative inhomogeneous dephasing ( $\gamma_d$ ), which results from the different trapping frequencies of ground and excited states; we can determine  $\gamma_d$  from atomic coherence time. In a real system, inhomogeneous spatial coupling of optically-trapped atoms comes from the distribution of atomic clouds at a finite temperature, and the cavity probe-induced ac Stark shifts are inhomogeneous depending on the spatial atom-cavity coupling. The spatial inhomogeneity is not considered in the simulation. The master equation is then as follows:

$$\dot{\hat{\rho}} = -i[\hat{\mathcal{H}}_N, \hat{\rho}] + 2\kappa\hat{\mathcal{D}}[\hat{a}]\hat{\rho} + 2\gamma_d\sum_{i=1}^N (\hat{\sigma}_{z,i}\hat{\rho}\hat{\sigma}_{z,i} - \hat{\rho}), \quad (2.8)$$

where  $\gamma_d$  is an inhomogeneous (non-radiative) dephasing rate that we measured. The second line is an inhomogeneous dephasing term. The above master equation describes collective atomic dynamics, which can be obtained by  $\hat{\rho}(t) = \prod_{j=1}^N \hat{\rho}_j(t)$ , where  $\hat{\rho}_j(t)$  is the density operator for the  $j$ -th single atom.

For a specific case of  $\Delta_p = \frac{\omega_a}{2}$  ( $> 0$ ), the ac Stark shift term is  $\frac{1}{\Delta_p} - \frac{1}{\Delta_p - \omega_a} = \frac{4}{\omega_a} = \frac{2}{\Delta_p}$ . The Hamiltonian is as follows:

$$\hat{\mathcal{H}}_{N,\Delta_p=\frac{\omega_a}{2}} = (\delta_0 - \Delta) \hat{a}^\dagger \hat{a} + 0 \cdot \sum_{i=1}^N \hat{\sigma}_{z,i} + \frac{2g^2 \hat{a}^\dagger \hat{a}}{\Delta_p} \sum_{i=1}^N \hat{\sigma}_{z,i} + i \mathcal{E}(\hat{a}^\dagger - \hat{a}) \quad (2.9)$$

If the unconditional master equation, where we do not consider quantum measurement process, is able to contain the effective spontaneous emission term using Lindblad forms (Eq. 2.10), it would be ideal to simulate collective atom-cavity system. Only in the specific case of  $\Delta_p = \frac{\omega_a}{2}$ , the unconditional master equation (Eq. 2.10) can be constructed without losing symmetry.

$$\begin{aligned} \dot{\hat{\rho}} = & -i[\hat{\mathcal{H}}_N, \hat{\rho}] + 2\kappa \hat{\mathcal{D}}[\hat{a}]\hat{\rho} \\ & + \frac{2\gamma_\perp}{\Delta_p^2 + (\frac{\gamma_\perp}{2})^2} \sum_{i=1}^N \left\{ \alpha \hat{\mathcal{D}}[\hat{\sigma}_{22,i}\hat{a}] + (1-\alpha) \hat{\mathcal{D}}[\hat{\sigma}_{12,i}\hat{a}] \right\} \hat{\rho} \\ & + \frac{2\gamma_\perp}{(\Delta_p - \omega_a)^2 + (\frac{\gamma_\perp}{2})^2} \sum_{i=1}^N \left\{ \beta \hat{\mathcal{D}}[\hat{\sigma}_{11,i}\hat{a}] + (1-\beta) \hat{\mathcal{D}}[\hat{\sigma}_{21,i}\hat{a}] \right\} \hat{\rho} \\ & + 2\gamma_d \sum_{i=1}^N \hat{\mathcal{D}}[\hat{\sigma}_{z,i}]\hat{\rho}, \end{aligned} \quad (2.10)$$

where  $\Delta_p = \frac{\omega_a}{2}$  and  $\hat{\mathcal{D}}[\hat{\sigma}_z] = \hat{\sigma}_z \hat{\rho} \hat{\sigma}_z - \hat{\rho}$  with  $\mathbb{I} = \hat{\sigma}_z^\dagger \hat{\sigma}_z = \hat{\sigma}_z \hat{\sigma}_z^\dagger$  ( $\hat{\sigma}_z^\dagger = \hat{\sigma}_z$ ); the coefficients of  $\alpha$  and  $\beta$  are determined by Clebsch-Gordon coefficients. The spontaneous emission from the cavity photons is modeled effectively as in the second and the third line. The fourth line is the inhomogeneous dephasing term. The detailed derivation of adiabatic eliminated atomic state that can be described by two hyperfine ground states' operator is shown in (45); a far-detuned and weak probe is replaced with a cavity field, and the Lindblad form of the effective spontaneous emission is reconstructed with a part of coherent interaction term and spontaneous emission related terms. The non-radiative dephasing term can be represented

by the Lindblad form. Using the above master equation, we can simulate our collective atom-cavity system, including the effective spontaneous emission and the dephasing.

Considering the state of atom-cavity system conditioned on the photodetection process, the stochastic Schrodinger equation (SSE) for heterodyne detection is as follows (46):

$$\begin{aligned} d|\tilde{\Psi}_c(t)\rangle = & \left\{ 1 - \left( \frac{\kappa}{2} \hat{a}^\dagger \hat{a} + \frac{\gamma}{2} \hat{\sigma}^\dagger \hat{\sigma} + i\hat{\mathcal{H}} \right) dt \right\} |\tilde{\Psi}_c(t)\rangle \\ & + \left\{ \sqrt{\kappa} \hat{a} \langle \sqrt{\kappa} \hat{a}^\dagger \rangle_c dt + dW_1 \sqrt{\kappa} \hat{a} \right\} |\tilde{\Psi}_c(t)\rangle \\ & + \left\{ \sqrt{\gamma} \hat{\sigma} \langle \sqrt{\gamma} \hat{\sigma}^\dagger \rangle_c dt + dW_2 \sqrt{\gamma} \hat{\sigma} \right\} |\tilde{\Psi}_c(t)\rangle, \end{aligned} \quad (2.11)$$

where  $dW_t = \frac{dW_{t,1} + idW_{t,2}}{\sqrt{2}}$  ( $t = 1, 2$ );  $dW_{t,1}$  and  $dW_{t,2}$  are independent Wiener increments for  $t = 1, 2$ , and  $|\tilde{\Psi}(t)\rangle$  is the unnormalized wave function. The transmitted cavity photons are measured by heterodyne detection with a strong local oscillator, and the spontaneous emission is assumed to be collected in a way of heterodyne detection by many detectors that cover the entire solid angle  $4\pi$ . In our system, the retro-reflected PDH beat note between a cavity-mode sideband and a carrier light is demodulated at a modulation frequency, which is similar to the heterodyne detection model. However, the retro-reflected beat note between a non-cavity-mode sideband and a carrier light generates some background noise.

For the collective atom-cavity system with  $N$  atoms at the detuning of  $\Delta_p = \frac{\omega_a}{2}$ , the SSE becomes as follows:

$$\begin{aligned} d|\tilde{\Psi}_c(t)\rangle = & \left\{ 1 - \left( \frac{\kappa}{2} \hat{a}^\dagger \hat{a} + \sum_{i=1}^N \sum_{k=1}^5 \frac{\gamma_k}{2} \hat{\Sigma}_{k,i}^\dagger \hat{\Sigma}_{k,i} + i\hat{\mathcal{H}} \right) dt \right\} |\tilde{\Psi}_c(t)\rangle \\ & + \left\{ \sqrt{\kappa} \hat{a} \langle \sqrt{\kappa} \hat{a}^\dagger \rangle_c dt + dW_1(t) \sqrt{\kappa} \hat{a} \right\} |\tilde{\Psi}_c(t)\rangle \\ & + \sum_{i=1}^N \sum_{k=1}^5 \left\{ \sqrt{\gamma_k} \hat{\Sigma}_{k,i} \langle \sqrt{\gamma_k} \hat{\Sigma}_{k,i}^\dagger \rangle_c dt + dW_{2,k,i}(t) \sqrt{\gamma_k} \hat{\Sigma}_{k,i} \right\} |\tilde{\Psi}_c(t)\rangle, \end{aligned} \quad (2.12)$$

where  $dW_j(t) = \frac{dW_{j,1}(t) + idW_{j,2}(t)}{\sqrt{2}}$  (for all  $j$ );  $dW_{j,1}(t)$  and  $dW_{j,2}(t)$  are independent Wiener increments ( $dW(t) \cdot dW(t) = dt$ ,  $E[dW(t)] = 0$ ). The collapse operators are  $\sqrt{\gamma_1} \hat{\Sigma}_{1,i} = \sqrt{\frac{\gamma_1}{\Delta_p^2 + (\frac{\gamma_1}{2})^2}} \alpha \hat{\sigma}_{22,i} \hat{a}$ ,  $\sqrt{\gamma_2} \hat{\Sigma}_{2,i} = \sqrt{\frac{\gamma_1}{\Delta_p^2 + (\frac{\gamma_1}{2})^2}} (1 - \alpha) \hat{\sigma}_{12,i} \hat{a}$ ,  $\sqrt{\gamma_3} \hat{\Sigma}_{3,i} = \sqrt{\frac{\gamma_1}{\Delta_p^2 + (\frac{\gamma_1}{2})^2}} \beta \hat{\sigma}_{11,i} \hat{a}$ ,  $\sqrt{\gamma_4} \hat{\Sigma}_{4,i} = \sqrt{\frac{\gamma_1}{\Delta_p^2 + (\frac{\gamma_1}{2})^2}} (1 - \beta) \hat{\sigma}_{21,i} \hat{a}$ ,  $\sqrt{\gamma_5} \hat{\Sigma}_{5,i} = \sqrt{\gamma_d} \hat{\sigma}_{z,i}$  where  $\gamma_k$  is assumed to be same for  $N$  atoms

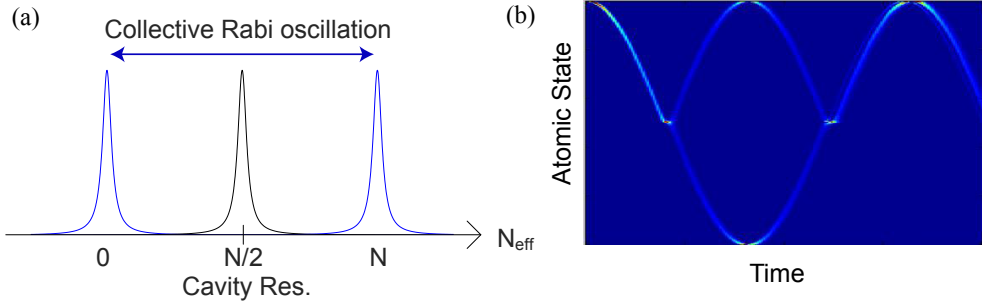


Figure 2.7: (a) Collective Rabi oscillation. (b) Macroscopic superposition state. The cavity becomes resonant at the mid-point of the full atom-induced-cavity shifts.

## 2.3 Macroscopic Self-Trapping

Utilizing a few kHz cavity linewidth and identically-coupled many atoms in our dual-wavelength (780nm – 1560nm) cavity, we expected to see a macroscopic superposition state during the collective Rabi oscillation when we set the cavity resonance at the mid-point of the full atom-induced cavity shifts. The atom-induced cavity shifts by  $N$  atoms are a couple hundred kHz. Therefore, the interaction regime of the collective atom-cavity interaction during Rabi oscillation is very sharp. In our simple simulation, we treated the collective atomic state as atom number states, but we simplified the cavity dynamics as the atom-number dependent ac Stark shift during Rabi-oscillation. Then, we could see the macroscopic superposition state as shown in Fig. 2.7. However, this simple model does not consider the quantum-mechanical atom-cavity interaction with cavity decay and quantum measurement theory. In reality, it is difficult to see the superposition state because the detection process of cavity photons entangled with atoms affects the atomic coherence, and the coherence of more atoms remains in a shorter time. For a larger number of atoms, the macroscopic superposition state becomes more fragile. Instead of the macroscopic superposition state, we observed macroscopic self-trapped state in the experiment (Fig. 2.8), which can be explained by the simulation of open quantum system (47; 48; 49; 50; 51; 52; 53). Chapter 6 presents self-trapping behavior in detail.

In a simulation, from the density matrix of collective atomic state, we could observe the atomic coherence of the superposition state for a very short time scale (Fig. 2.9). If a macroscopic superposition state occurs, such as  $\frac{1}{2} \left( | \frac{N}{2} - m \rangle + | \frac{N}{2} + m \rangle \right)$ , we have to see

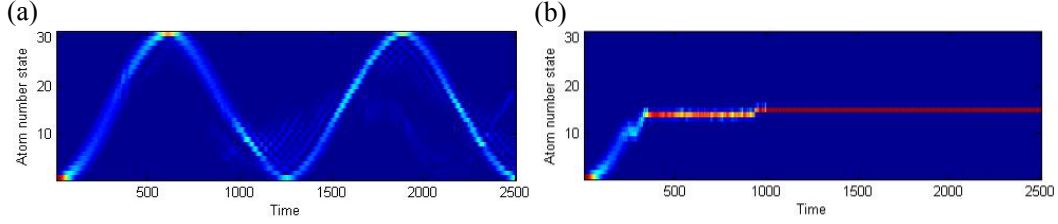


Figure 2.8: Rabi oscillation to self-trapping. (a) Rabi oscillation. (b) Self-trapping.



Figure 2.9: Coherence of a macroscopic superposition state; density matrices (3D and 2D plots) of macroscopic superposition state generated by collective atom-cavity interaction shows off-diagonal elements as an evidence for coherence.

abrupt cavity transmission drop because both  $|\frac{N}{2} - m\rangle$  and  $|\frac{N}{2} + m\rangle$  atomic states cannot make the cavity to be on-resonant, where  $N$  is a total atom number and  $m$  is a separated atom number from  $\frac{N}{2}$ ; only when the atomic states are close to  $|\frac{N}{2}\rangle$  state, we can see the cavity transmission. When we measure the macroscopic superposition state, the state would be stochastically projected to  $|\frac{N}{2} - m\rangle$  state or  $|\frac{N}{2} + m\rangle$  state, and the measurement output is expected to have a random fluctuation between the two states.

When all atoms are trapped in the cavity optical lattices, the in-phase cavity probe registers all the atoms homogeneously. Therefore, we are able to treat all the atoms equivalently. For the Hamiltonian of macroscopic self-trapping, we turn on the microwave Rabi field during the atom-cavity interaction; the dynamics of self-trapping requires the microwave field term. For  $N$  atoms, the Hamiltonian of self-trapping is

$$\begin{aligned} \hat{\mathcal{H}}_N = & (\delta_0 - \Delta) \hat{a}^\dagger \hat{a} + \mathbf{0} \cdot \hat{\mathbf{J}}_z \\ & + g^2 \hat{a}^\dagger \hat{a} \hat{J}_z \left( \frac{1}{\Delta_p} - \frac{1}{\Delta_p - \omega_a} \right) \\ & \Omega_{\mu w} (\hat{J}_- + \hat{J}_+) + i \mathcal{E} (\hat{a}^\dagger - \hat{a}), \end{aligned} \quad (2.13)$$

where  $\hat{J}_z = \sum_{i=1}^N \hat{\sigma}_{z,i}$ ,  $\hat{J}_- = \sum_{i=1}^N \hat{\sigma}_{12,i}$ ,  $\hat{J}_+ = \sum_{i=1}^N \hat{\sigma}_{21,i}$ .

The unconditional master equation is as follows:

$$\dot{\hat{\rho}} = -i[\hat{\mathcal{H}}_N, \hat{\rho}] + 2\kappa\hat{\mathcal{D}}[\hat{a}]\hat{\rho} + 2\gamma_\perp\hat{\mathcal{D}}[\hat{\sigma}_{1e}]\hat{\rho} + 2\gamma_\perp\hat{\mathcal{D}}[\hat{\sigma}_{2e}]\hat{\rho}. \quad (2.14)$$

The collective atomic state oscillates coherently at a microwave frequency, and the atom-cavity interaction occurs when the incident cavity probe becomes on-resonance at the mid-point of a full Rabi oscillation. The collective atom-cavity interaction is based on  $g^2\hat{a}^\dagger\hat{a}\hat{J}_z\left(\frac{1}{\Delta_p} - \frac{1}{\Delta_p - \omega_a}\right)$ . We can simulate the interaction in two ways. First, a collective atomic basis like the Dicke state simplifies the simulation process, and we need only a small number of matrices ( $\mathbb{I} = \mathbb{I}_{atom} \otimes \mathbb{I}_{photons}$ ,  $\mathbb{I}_{atoms}$  means a  $N_{at} \times N_{at}$  matrix for atoms). However, this approach cannot generally include spontaneous emission and dephasing terms because the symmetry of the collective atomic state is broken by those terms. For the macroscopic self-trapping effect, we can neglect spontaneous emission because of a few pW level incident cavity photons, but spontaneous emission needs to be included for the spin-squeezing because of a few nW level incident cavity photons. Optically-trapped atoms also experience some dephasing, but it is smaller than it is in the non-trapped atom case. Second, if we use an entangled  $N_{at}$  single atom basis ( $2^{N_{at}} \times 2^{N_{at}}$ ) for a generalized simulation, we can include an inhomogeneous dephasing term and an effective spontaneous emission term. The total density operator is  $\hat{\rho}(t) = \prod_{j=1}^N \hat{\rho}_j(t)$ , where  $\hat{\rho}_j(t)$  is the density operator for the  $j$ -th independent atom.

In the specific case of  $\Delta_p = \frac{\omega_a}{2}$ , the unconditional master equation of macroscopic self-trapping can have the effective spontaneous emission term using the Lindblad form without losing symmetry.

$$\begin{aligned} \dot{\hat{\rho}} = & -i[\hat{\mathcal{H}}_N, \hat{\rho}] + 2\kappa\hat{\mathcal{D}}[\hat{a}]\hat{\rho} \\ & + \frac{2\gamma_\perp}{\Delta_p^2 + (\frac{\gamma_\perp}{2})^2} \sum_{i=1}^N \left\{ \alpha\hat{\mathcal{D}}[\hat{\sigma}_{22,i}\hat{a}] + (1-\alpha)\hat{\mathcal{D}}[\hat{\sigma}_{12,i}\hat{a}] \right\} \hat{\rho} \\ & + \frac{2\gamma_\perp}{(\Delta_p - \omega_a)^2 + (\frac{\gamma_\perp}{2})^2} \sum_{i=1}^N \left\{ \beta\hat{\mathcal{D}}[\hat{\sigma}_{11,i}\hat{a}] + (1-\beta)\hat{\mathcal{D}}[\hat{\sigma}_{21,i}\hat{a}] \right\} \hat{\rho} \\ & + 2\gamma_d \sum_{i=1}^N \hat{\mathcal{D}}[\hat{\sigma}_{z,i}]\hat{\rho}, \end{aligned} \quad (2.15)$$

where  $\Delta_p = \frac{\omega_a}{2}$  and  $\hat{\mathcal{D}}[\hat{\sigma}_{z,i}] = \hat{\sigma}_{z,i}\hat{\rho}\hat{\sigma}_{z,i} - \hat{\rho}$ .

Considering the state of the collective atom-cavity system conditioned on the photodetection process (photon counting), the stochastic Schrodinger equation (46; 54) for the direct photodetection and  $N$  atoms at the detuning of  $\Delta_p = \frac{\omega_a}{2}$  is

$$\begin{aligned} d|\psi_c(t)\rangle = & \left\{ -i\hat{\mathcal{H}}dt - \kappa(\hat{a}^\dagger\hat{a} - \langle\hat{a}^\dagger\hat{a}\rangle_c)dt + \left( \frac{\hat{a}}{\sqrt{\langle\hat{a}^\dagger\hat{a}\rangle}} - 1 \right) dN_1(t) \right\} |\psi_c(t)\rangle \\ & - \sum_{i=1}^N \left\{ \sum_{k=1}^5 \gamma_k \left( \hat{\Sigma}_{k,i}^\dagger \hat{\Sigma}_{k,i} - \langle \hat{\Sigma}_{k,i}^\dagger \hat{\Sigma}_{k,i} \rangle_c \right) dt \right\} |\psi_c(t)\rangle, \\ & \sum_{i=1}^N \left\{ \sum_{k=1}^5 \left( \frac{\hat{\Sigma}_{k,i}}{\sqrt{\langle \hat{\Sigma}_{k,i}^\dagger \hat{\Sigma}_{k,i} \rangle}} - 1 \right) dN_{2,k,i}(t) \right\} |\psi_c(t)\rangle, \end{aligned} \quad (2.16)$$

where  $|\psi_c(t)\rangle$  is the normalized wave function, and  $dN_j(t)$  is the increment in the photo-count of the detector in the time interval  $(t, t+dt]$  with  $dN_j^2(t) = dN_j(t)$  and  $dN_j(t)dt = 0$ . The collapse operator  $\sqrt{\gamma_k} \hat{\Sigma}_k$  are the same as the spin-squeezing SSE.

## 2.4 Raman Lasing

We observed a continuous-wave Raman lasing using  $^{87}\text{Rb}$  cold atoms as a gain medium in a high finesse optical cavity (Fig. 2.10). This Raman lasing where single atoms can affect the cavity field has tunable gain property and unusual lasing threshold behavior in the system causing a jump in lasing power by a lasing-induced ac Stark shift. This section presents a quantum-mechanical model to describe the unusual lasing threshold behavior. A semi-classical model and experimental data will be presented in Chapter 7.

We use a three-level atom model for the Raman lasing, where two hyperfine ground states are  $|1\rangle = |F=1\rangle$  and  $|2\rangle = |F=2\rangle$ , and the optical excited state is  $|e\rangle = |F'=2\rangle$ . The two-photon transition of a Raman lasing occurs with a Raman pump and a lased cavity mode for the hyperfine transition of  $F'=2$ , where the single-photon detuning  $\Delta_{rmn}$  and two-photon detuning  $\delta$  determine the lasing properties (Fig. 2.11); the pump frequency variation ( $\omega_p \pm \Delta_p$ ) changes  $\delta$ .

The atypical threshold behavior of the Raman lasing in our atom-cavity system can be explained by the lasing-induced ac Stark shift (Fig. 2.12). For a blue-detuned lasing

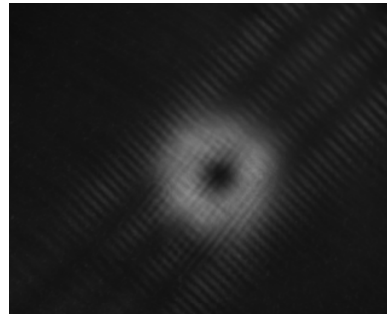


Figure 2.10: CCD image of a TEM<sub>00</sub> lasing mode and higher-order modes

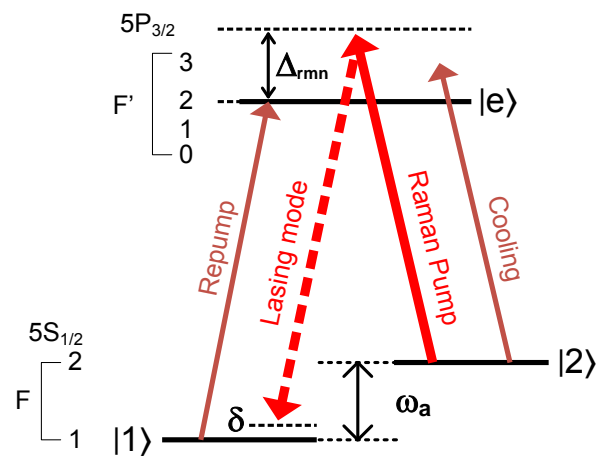


Figure 2.11: Three level atom model of Raman lasing with single-photon detuning  $\Delta_{rmn}$  and two-photon detuning  $\delta$ ; two hyperfine ground states are  $|1\rangle = |F = 1\rangle$  and  $|2\rangle = |F = 2\rangle$ ,  $|e\rangle = |F' = 2\rangle$ ,  $\Delta_{rmn} = \omega_p - \omega_{e2}$ , where  $\omega_p$  is a Raman pump frequency.  $\delta = \omega_a - (\omega_l - \omega_p)$ , where  $\omega_l$  is a lasing frequency. ( $\Delta_{rmn} = \Delta$  in Chapter 7).

mode ( $\Delta_{rmn} > 0$ ) and positive  $\delta$ , we can observe an abrupt jump in the lasing output. The initiated lasing mode shifts the  $F = 1$  state up, and the gain increases more. Therefore, the lasing output increases more, and the ac Stark shift increase further before it becomes an equilibrium (Fig. 2.12 (a)). However, for a blue-detuned lasing mode ( $\Delta_{rmn} > 0$ ) and negative  $\delta$ , the lasing mode also shifts  $F = 1$  state up, and the gain decreases. Therefore, this effect disappears (Fig. 2.12 (b)). In the simulations, we observed this unusual lasing threshold behavior and tunable gain properties, varying Raman pump intensity  $I_p$  (Fig. 2.13) and two-photon detuning  $\delta$  (Fig. 2.14).

The quantum-mechanical model of Raman lasing with three-level atoms are described as following: For a single atom ( $\hbar = 1$ ), the Hamiltonian of our system is

$$\hat{\mathcal{H}} = \omega_c \hat{a}^\dagger \hat{a} + \omega_e |e\rangle \langle e| + \omega_1 |1\rangle \langle 1| + \omega_2 |2\rangle \langle 2| + \Omega_p (e^{-i\omega_p t} \hat{\sigma}_{2e} + \hat{\sigma}_{e2} e^{i\omega_p t}) + ig (e^{-i\omega_l t} \hat{a}^\dagger \hat{\sigma}_{1e} - \hat{\sigma}_{e1} \hat{a} e^{i\omega_l t}), \quad (2.17)$$

where  $\omega_l$  is a lasing frequency into a cavity and  $\omega_c$  is a cavity resonant frequency for two photon Raman transition with a Raman pump frequency  $\omega_p$ . The Hamiltonian of Raman lasing does not have microwave field ( $\Omega_{\mu w} = 0$ ) and cavity driving field ( $\mathcal{E} = 0$ ). In the second line, the first term is the Raman pump field ( $\omega_p$ ), and the second term is a cavity lasing field ( $\omega_l$ ), which is generated from a two-photon process using MOT atoms as the gain medium. With a transferred frame rotating at the lasing frequency  $\omega_l$  and setting the state of  $|2\rangle \langle 2|$  as zero energy, we can have the following Hamiltonian:

$$\hat{\mathcal{H}}' = -\Delta_{lc} \hat{a}^\dagger \hat{a} - \Delta_{le} |e\rangle \langle e| - \omega_a |1\rangle \langle 1| + \frac{\Omega_p}{2} (e^{i\Delta_{lp} t} \hat{\sigma}_{2e} + \hat{\sigma}_{e2} e^{-i\Delta_{lp} t}) + ig (\hat{a}^\dagger \hat{\sigma}_{1e} - \hat{\sigma}_{e1} \hat{a}), \quad (2.18)$$

where  $\Delta_{lc} = \omega_l - \omega_c$ ,  $\Delta_{le} = \omega_l - \omega_{e1}$ ,  $\Delta_{lp} = \omega_l - \omega_p$ ,  $\Delta_{rmn} = \omega_p - \omega_{e2}$ ,  $\omega_a = \omega_2 - \omega_1 = 2\pi \cdot 6.835 \text{ GHz}$ , and  $\delta = \omega_{e1} + \Delta_{rmn} - \omega_l = \omega_a - \Delta_{lp}$ . We can adiabatically eliminate the excited state for the dynamics in the two ground states because we have a large detuning  $|\Delta_{rmn}| \gg \kappa, g, \gamma_\perp$ .

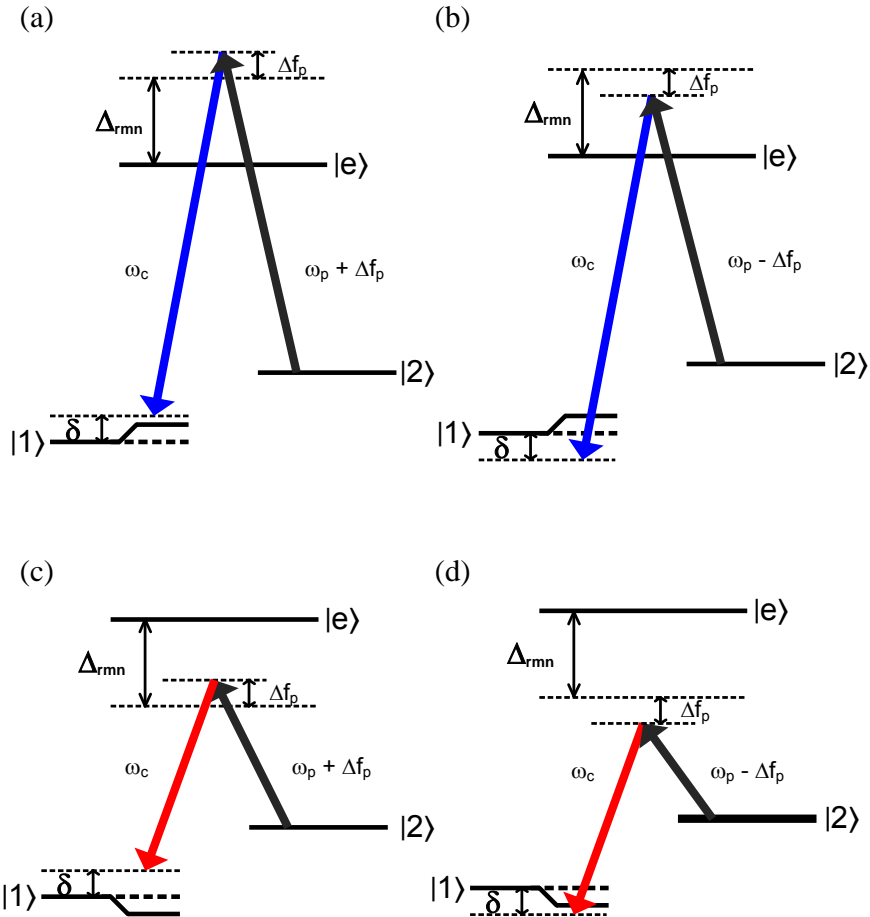


Figure 2.12: Lasing-induced ac Stark shift. (a) Blue-detuned lasing ( $\Delta_{rmn} > 0$ ) and the increased gain ( $\delta > 0$ ). (b) Blue-detuned lasing ( $\Delta_{rmn} > 0$ ) and the decreased gain ( $\delta < 0$ ). (c) Red-detuned lasing ( $\Delta_{rmn} < 0$ ) and the decreased gain ( $\delta > 0$ ). (d) Red-detuned lasing ( $\Delta_{rmn} < 0$ ) and the increased gain ( $\delta < 0$ ). When  $\omega_p$  varies as much as the relative pump frequency  $\Delta f_p$ , the lasing-induced ac Stark shift results in atypical lasing threshold behavior jumping in power which increases or decreases the gain according to  $\Delta_{rmn}$  and  $\delta$ .

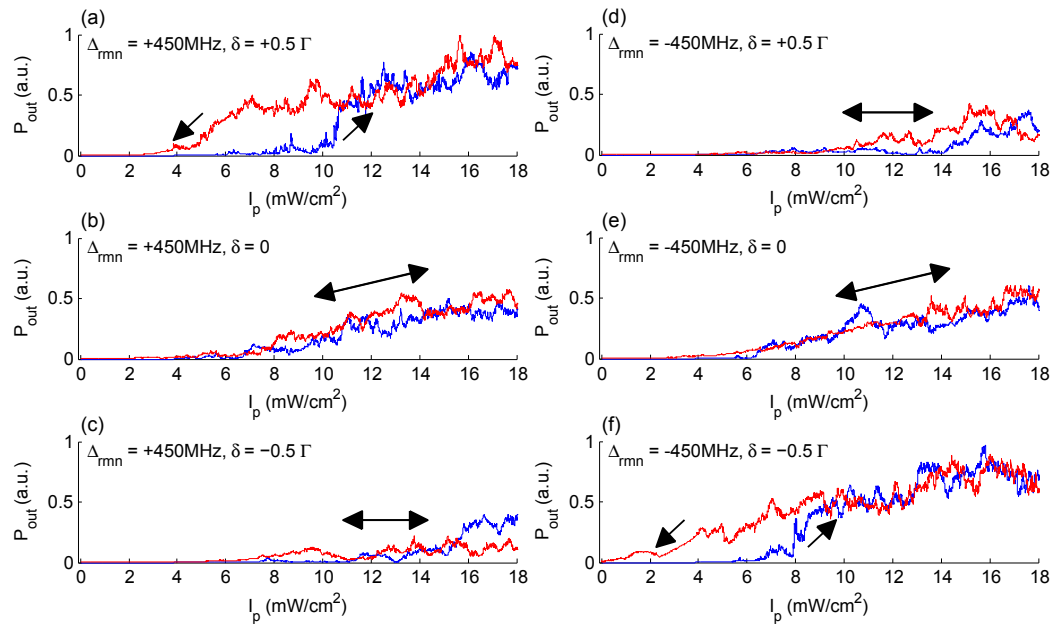


Figure 2.13: Simulation results of lasing output vs. pump intensity  $I_p$  (a)  $\Delta_{\text{rmn}} = +450\text{MHz}$ ,  $\delta = +0.5\Gamma$ . (b)  $\Delta_{\text{rmn}} = +450\text{MHz}$ ,  $\delta = 0$ . (c)  $\Delta_{\text{rmn}} = +450\text{MHz}$ ,  $\delta = -0.5\Gamma$ . (d)  $\Delta_{\text{rmn}} = -450\text{MHz}$ ,  $\delta = +0.5\Gamma$ . (e)  $\Delta_{\text{rmn}} = -450\text{MHz}$ ,  $\delta = 0$ . (f)  $\Delta_{\text{rmn}} = -450\text{MHz}$ ,  $\delta = -0.5\Gamma$ . (a), (b), (c) are blue-detuned Raman lasers, and (d), (e), (f) are red-detuned Raman lasers.

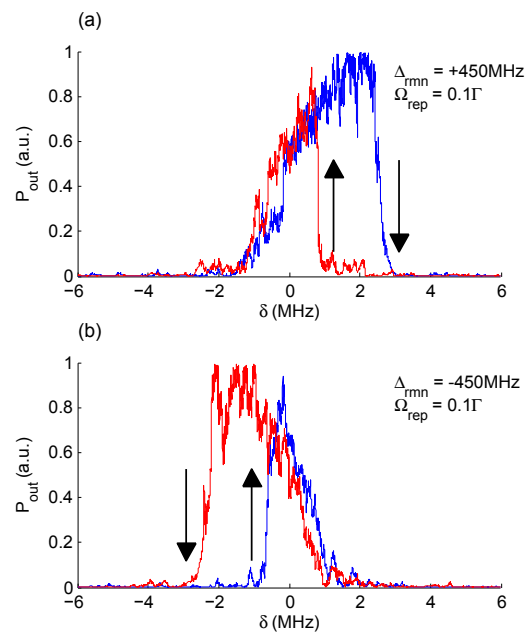


Figure 2.14: Simulation results of lasing output vs. two-photon detuning  $\delta$ . (a) Blue-detuned Raman lasing ( $\Delta_{\text{rmn}} = +450\text{MHz}$ ); for a positive  $\delta$ , there exists abrupt lasing output transition. (b) Red-detuned Raman lasing ( $\Delta_{\text{rmn}} = -450\text{MHz}$ ); for a negative  $\delta$ , there exists abrupt lasing output transition.

$$\begin{aligned}\hat{\mathcal{H}}'' &= -\Delta_{lc}\hat{a}^\dagger\hat{a} - \omega_a|1\rangle\langle 1| \\ &\quad + i\frac{g\Omega_p}{\Delta_{rmn}}(e^{i\Delta_{lp}t}|1\rangle\langle 2| - |2\rangle\langle 1|)e^{-i\Delta_{lp}t}) \\ &\quad + \frac{g^2}{\Delta_{rmn}}\hat{a}^\dagger\hat{a}|1\rangle\langle 1| + \frac{\Omega_p^2}{4\Delta_{rmn}}|2\rangle\langle 2|,\end{aligned}\tag{2.19}$$

In addition, with a transferred frame rotating at a microwave transition frequency  $\Delta_{lp} = -(\delta - \omega_a)$ , we obtain the following Hamiltonian:

$$\begin{aligned}\hat{\mathcal{H}}''' &= -\Delta_{lc}\hat{a}^\dagger\hat{a} - \delta|1\rangle\langle 1| \\ &\quad + i\frac{g\Omega_p}{\Delta_{rmn}}(|1\rangle\langle 2| - |2\rangle\langle 1|) \\ &\quad + \frac{g^2}{\Delta_{rmn}}\hat{a}^\dagger\hat{a}|1\rangle\langle 1| + \frac{\Omega_p^2}{4\Delta_{rmn}}|2\rangle\langle 2|,\end{aligned}\tag{2.20}$$

The detuning of Raman lasing,  $\Delta_{rmn}$ , can be varied while we change  $\delta$ , and we include this effect in  $\Delta_{rmn}$  for the simulation of Raman pump frequency sweep:  $\frac{1}{\Delta_{rmn}}$  becomes  $\frac{1}{\Delta_{rmn}-\delta} = \frac{1}{\Delta_{rmn}}\frac{1}{(1-\delta/\Delta_{rmn})} \simeq \frac{1}{\Delta_{rmn}} + \frac{\delta}{\Delta_{rmn}^2}$  for  $\delta \ll \Delta_{rmn}$ .

In the experiments, the continuous Raman lasing that needs repumping process (population inversion) is collective atomic behavior. When we consider many atoms and effective incoherent repumping process, the Hamiltonian becomes

$$\begin{aligned}\hat{\mathcal{H}}_N &= -\Delta_{lc}\hat{a}^\dagger\hat{a} - \sum_{i=1}^N \delta|1\rangle\langle 1|_i \\ &\quad + i\sum_{i=1}^N \frac{g\Omega_p}{\Delta_{rmn}}(|1\rangle\langle 2|_i - |2\rangle\langle 1|_i) \\ &\quad + \frac{g^2}{\Delta_{rmn}}\hat{a}^\dagger\hat{a}\sum_{i=1}^N|1\rangle\langle 1|_i + \frac{\Omega_p^2}{4\Delta_{rmn}}\sum_{i=1}^N|2\rangle\langle 2|_i \\ &\quad + 2\gamma_{rep}\sum_{i=1}^N\hat{\mathcal{D}}[|2\rangle\langle 1|_i]\hat{\rho},\end{aligned}\tag{2.21}$$

where the fourth line has the incoherent repumping process term from  $|1\rangle$  to  $|2\rangle$  with a repumping rate  $\gamma_{rep}$ .

For the case of  $\delta = 0$ , i.e.,  $\Delta_{lc} = 0$ , we can include the effective spontaneous emission term generally using the Lindblad form without losing symmetry as follows:

$$\begin{aligned}
\dot{\hat{\rho}} = & -i[\hat{\mathcal{H}}_N, \hat{\rho}] + 2\kappa\hat{\mathcal{D}}[\hat{a}]\hat{\rho} \\
& + 2\gamma_{rep}\sum_{i=1}^N\hat{\mathcal{D}}[\hat{\sigma}_{21,i}]\hat{\rho} \\
& + \frac{2\gamma_\perp}{[-\Delta_{rmn}-\delta]^2+(\frac{\gamma_\perp}{2})^2}\sum_{i=1}^N\left\{\alpha\hat{\mathcal{D}}[\hat{\sigma}_{22,i}\hat{a}] + (1-\alpha)\hat{\mathcal{D}}[\hat{\sigma}_{12,i}\hat{a}]\right\}\hat{\rho} \\
& + \frac{2\gamma_\perp}{[-\Delta_{rmn}+\Delta_{lc}]^2+(\frac{\gamma_\perp}{2})^2}\sum_{i=1}^N\left\{\beta\hat{\mathcal{D}}[\hat{\sigma}_{11,i}\hat{a}] + (1-\beta)\hat{\mathcal{D}}[\hat{\sigma}_{21,i}\hat{a}]\right\}\hat{\rho} \\
& 2\gamma_d\sum_{i=1}^N\hat{\mathcal{D}}[\hat{\sigma}_{z,i}]\hat{\rho},
\end{aligned} \tag{2.22}$$

where  $\delta = 0$  and  $\Delta_{lc} = 0$ . The third and fourth lines are the effective spontaneous emission of cavity photons, and the fifth line is the non-radiative dephasing term with a dephasing rate  $\gamma_d$ . The numerical simulation results in this section is based on this quantum-mechanical model, which can explain atypical lasing threshold behavior of our Raman, and a semi-classical theory also can describe the atypical lasing behavior analytically with experimental data (Chapter 7).

## 2.5 Conclusion

We explored several collective atom-cavity interactions using the open quantum system simulation (55) which includes cavity decay, spontaneous emission process, and quantum measurement theory. The Hamiltonians for spin-squeezing and macroscopic self-trapping are similar except for a microwave field term and the initial condition of cavity resonance point. The spin-squeezing process needs only a  $\frac{\pi}{2}$  pulse for the initial state preparation to generate coherent spin state before the cavity probe turns on. For the macroscopic self-trapping state, the cavity probe has to be resonant at the mid-point of the full atom-induced cavity shift during the collective Rabi oscillation, and the microwave field is kept on during the collective atom-cavity interactions.

The cavity photon detection process after the atom-cavity interaction affects the collective atomic state in the experiment of spin-squeezing and macroscopic self-trapping; in the real experiments, the intracavity photon number of spin-squeezing is higher than that of self-trapping (a few pW for  $\sim 92$  Hz Rabi oscillation). The cavity photon detection process and spontaneous emission process can be modeled by the theory of quantum measurement.

The photon detection process of spin-squeezing experiment can be modeled approximately as the heterodyne detection (54; 56); the beat note signal from a carrier light and a cavity mode is demodulated to measure the atom-induced cavity shift from the variation of the index of refraction, but non-cavity modes retro-reflected off from the cavity mirror surface adds background noise. The photon detection process of self-trapping experiment can be modeled as the direct photon counting process because we measure cavity-transmitted photons using an SPCM.

The photon detection process of Raman lasing, i.e. the quantum measurement process, can be neglected for the Raman lasing model because the effect of lasing dynamics dominate over that of quantum measurement. Compared to the spin-squeezing and the macroscopic self-trapping, the Raman lasing model does not have a microwave field and input cavity field, but it needs a Raman pump field and an incoherent repumping process for lasing. The Raman laser is two-photon process of the Raman pump and the cavity lasing field.

We have explored the Hamiltonians of our experiments, but there are several limitations to simulating this collective atom-cavity interaction. Using the entangled single atomic operators, the collective atom-cavity states, such as  $2^{N_{at}} \otimes n_{ph}$  can include spontaneous emission terms and non-radiative dephasing terms without losing symmetry, where  $N_{at}$  is an atom number, and  $n_{ph}$  is a photon number. However, this model requires enormous computing resources for  $N \gtrsim 10$ . The collective atom-cavity states, such as  $N_{at} \otimes n_{ph}$ , using the collective atomic operators cannot include spontaneous emission and non-radiative dephasing terms in a general way because of symmetry breaking. If we can neglect spontaneous emission,  $N_{at} \otimes n_{ph}$  model is useful to simulate thousands of atoms. The difference between two simulations is whether we use the entangled single atomic operators or the collective atomic operators.

# Chapter 3

## Cold Atoms in a Cavity

The development of the laser has contributed significantly to the study of atoms and molecules via laser spectroscopy and laser cooling and trapping. In a cavity chamber, we cool and trap atoms using a magneto-optical trap (MOT) (57; 58; 59; 60; 61), and the atoms are coupled to a cavity mode (62; 63). Using this atom-cavity system, we have studied the light and matter interaction. This chapter presents the apparatus and techniques used.

### 3.1 Lasing Cooling and Trapping

The laser cooling and trapping technique was developed in the early 1980s for high-resolution spectroscopy. This technique had a major impact on atomic physics research because precision spectroscopy of the cold atoms always requires optimal trapping to suppress the random motion of the atoms.

#### Scattering Force and Dipole Force

There are two types of optical forces between atoms and light: the scattering force and the dipole force. When a photon is scattered by an atom, the atom absorbs the photon and remits a photon spontaneously into free space. The atom experiences the scattering force and recoils because of the photon's momentum transfer. The scattering force  $\vec{F}_{scatt}$  of the

closely resonant light (64) is described with photon momentum  $\hbar\vec{k}$  and scattering rate  $R_{scatt}$  as follows:

$$\begin{aligned}\vec{F}_{scatt} &= \hbar\vec{k} \cdot R_{scatt} \\ &= \hbar\vec{k} \cdot \frac{\Gamma}{2} \frac{\Omega^2/2}{\delta^2 + \Omega^2/2 + \Gamma^2/4}\end{aligned}\quad (3.1)$$

where  $\delta$  is the light-atom detuning ( $\delta = \omega - \omega_0$ ),  $k$  is the wave number,  $\Omega$  is the Rabi frequency, and  $\Gamma$  is the spontaneous emission rate. As the atoms scatter more photons, the scattering force increases. Therefore, the scattering force is proportional to the scattering rate. This radiation pressure on the atoms decelerates the atoms. Optical molasses (65) and MOT atoms are generated using the scattering force.

The gradient of the photon's energy generates the dipole forces – a conservative force along the gradient direction. When the light field varies over slower length scales than the deBroglie wavelength ( $\lambda_{dBroglie} \ll \lambda_{light}$ ), the rate of the momentum change is equal to the force as follows:

$$\frac{d\langle\vec{p}\rangle}{dt} = -\langle\nabla U\rangle = \vec{F}, \quad (3.2)$$

where  $\vec{p}$  is the momentum of the atoms, and  $U$  is the potential energy. The optical dipole potential is  $U_{dipole} \simeq \frac{\hbar\Omega^2}{4\delta} = \frac{\hbar\Gamma^2}{8\delta} \frac{I}{I_{sat}}$  (64), where  $I_{sat}$  is the saturation intensity. Thus, the dipole force  $\vec{F}_{dipole}$  is described as follows:

$$\vec{F}_{dipole} = -\nabla U_{dipole} \quad (3.3)$$

$$= -\frac{\partial}{\partial z} \left( \frac{\hbar\Omega^2}{4\delta} \right) \quad (3.4)$$

$$= -\frac{\hbar\delta}{2} \frac{\Omega}{\delta^2 + \Omega^2/2 + \Gamma^2/4} \frac{\partial\Omega}{\partial z}, \quad (3.5)$$

where  $\Omega$  is Rabi frequency;  $|\delta| \gg \Gamma$  and  $|\delta| \gg \Omega$ . When the atoms in the ground-state experience an optical dipole potential,  $U_{dipole}$ , a light shift (the ac Stark shift) occurs. The variation of the light shift along the gradient direction produces the dipole force on the atoms. The dipole force generates a dipole trap if the light is far-detuned and intense. Positive detuning  $\delta$  ( $\omega > \omega_0$ ), blue-detuned light, means that the atoms experience a repelling

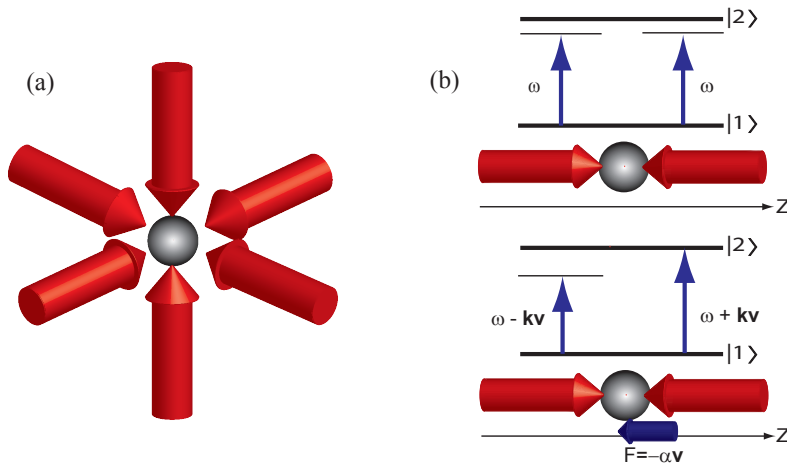


Figure 3.1: (a) Optical molasses (b) The mechanism of optical molasses; stationary atoms do not experience a force, moving atoms experience a force due to the Doppler effect.

force; whereas negative detuning  $\delta$  ( $\omega < \omega_0$ ), red-detuned light, means that the atoms experience an attracting force. The dipole force is conservative, and it is used for the dipole trap, the optical lattice, and the evanescent field reflector.

## Optical Molasses

The optical molasses (Fig. 3.1 (a)) technique confines atoms within a finite volume by the scattering force, which means that atoms are captured in a velocity class but are not trapped spatially. Two red-detuned beams from the  $x$ ,  $y$ ,  $z$  direction counterpropagate to the atoms, and the moving atoms encounter the scattering force from the photons' momentum due to the Doppler effect (Fig. 3.1 (b)).

The Doppler effect causes the atoms to experience an imbalanced force. Therefore, we can confine the atoms within the overlapping volume of the three beams. The scattering force is used to generate the optical molasses.

## Magneto-Optical Trap

The optical molasses technique only confines atoms within some volume. Adding a spatial magnetic-field gradient enables us to trap and cool atoms better. The result is a MOT.

Atoms such as alkali atoms experience a scattering force from the photon's momentum, and the magnetic degeneracy of the atoms splits under a magnetic field. The optimal photon scattering under the magnetic field controls the optical force on the atoms, which cools and traps the atoms in a vacuum.

Using a MOT, we cool and trap  $^{87}\text{Rb}$  atoms in our experiments. The principle of the MOT is as follows: Under a magnetic-field gradient, the degenerate magnetic energy levels of the atoms are split based on the atom's position. At the center of an anti-Helmholtz coil magnetic field, where the magnetic field is zero, atoms can be trapped because they are insensitive to the scattering force. As atoms move away from the center, the magnetic-field dependent energy levels are split further. The three x, y, z directional red-detuned counter-propagating ( $\sigma^+, \sigma^-$ ) cooling beams ( $F = 2 \rightarrow F' = 3$ , 780.246 nm) become on-resonance to the atomic energy levels split by a magnetic field when the atoms move toward the beams as a result of the Doppler effect (Fig. 3.2). The cooling beams exert a scattering force on the moving atoms, and the atoms lose their kinetic energy (66). Therefore, atoms can be confined in the overlapped volume of the 3D MOT cooling beams. The scattering process by the cooling beam pumps atoms from the  $F = 2$  to the  $F = 1$  state after spontaneous atomic decay. As the number of atoms in the  $F = 2$  state decreases, the cooling process becomes inefficient. The repumping beam ( $F = 1 \rightarrow F' = 2$ , 780.232 nm) can solve this problem by pumping the  $F = 1$  state atoms to the  $F = 2$  state.

We cool down the temperature of atoms further using a far-detuned MOT and optical molasses stage (polarization gradient cooling). A far-detuned and weak cooling beam enables us to have a far-detuned MOT which is colder than a MOT. After turning off the magnetic field and zeroing the residual magnetic field by bias fields, the far-detuned MOT atoms can be transformed to optical molasses atoms with a further-detuned and weaker cooling beam. The temperature of the atoms is measured using the time-of-flight (TOF) measurement; the measured temperature was about  $14.5\,\mu\text{K}$  after the far-detuned MOT process and optical molasses stage.

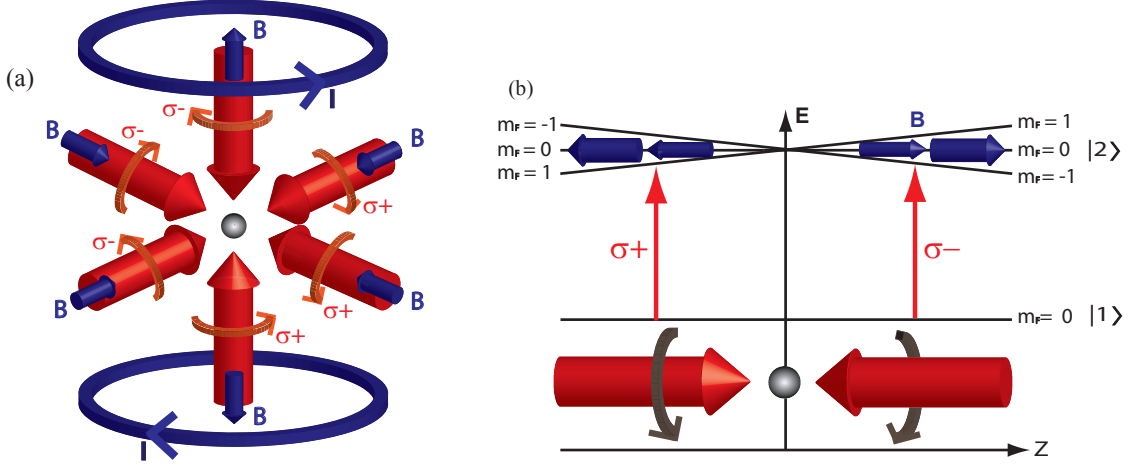


Figure 3.2: (a) MOT configuration;  $\sigma_k^+$  ( $\sigma_k^-$ ) light means that the light rotates clockwise (counter-clockwise) when it is viewed along the quantization axis  $+\hat{k}$  for  $\hat{k} = \hat{x}, \hat{y}, \hat{z}$ . (b) The mechanism of MOT; a red-detuned cooling beams become on-resonance to the atomic transition split by a magnetic field due to Doppler effect.

## 3.2 Cavity System

Our high-finesse cavity is combined with a vacuum chamber. Laser-cooled atoms are loaded into the central region of the cavity for studying the atom-cavity interaction. We developed two types of cavity chambers, a single-wavelength (single- $\lambda$ ) hemispherical cavity chamber with a PZT (Piezoelectric Transducer) and a dual-wavelength (dual- $\lambda$ ) confocal cavity without a PZT. Chapter 4 presents the single- $\lambda$  cavity experiments on collective normal mode splitting and spin-squeezing. Chapters 5, 6, 7 present the dual- $\lambda$  cavity experiments on identical atom-cavity coupling, macroscopic self-trapping, and Raman lasing.

### Optical Cavity Design

Optical cavities are widely used in various fields, but it is difficult to design a high-finesse cavity combined with many atoms in an ultra-high vacuum (UHV). For our experiment, we designed several cavities. Our single- $\lambda$  hemispherical cavity with a 205,000 finesse was designed to study the interaction between quantized light in the cavity and the cold atoms. A large cavity mode area ( $w_0 = 310\mu\text{m}$ ) at the cavity center allows the cavity mode to

Table 3.1: Cavity parameters

Parameters	Single- $\lambda$ cavity	Dual- $\lambda$ cavity	
Cavity Configuration	hemispherical	confocal	
Wavelength	780 nm cavity	780 nm cavity	1560 nm cavity
Cavity Finesse $\mathcal{F}$	205,000	175,000	117,000
Mirror Radius of Curvature $R$	10 cm	9.9 cm	
Cavity Length $L_{cav}$	9.96 cm	10.73 cm	
Free Spectral Range $\frac{\Delta\nu_{fsr}}{2\kappa}$	1.505 GHz	1.3964 GHz	
Cavity Mode Waist $w_0$	310 $\mu$ m	111 $\mu$ m	157 $\mu$ m
Maximum Coupling Strength $\frac{g_0}{2\pi}$	53 kHz	142 kHz	—
Cavity Half Linewidth $\frac{\kappa}{2\pi}$	3.7 kHz	3.99 kHz	5.98 kHz
Atomic Half Linewidth $\frac{\gamma}{2\pi}$	3.03 MHz		
Single Atom Cooperativity $\frac{g_0^2}{2\kappa\gamma}$	0.125	0.84	—
Chamber vacuum pressure $P$	$\sim 10^{-8}$ mbar	$10^{-10} \sim 10^{-9}$ mbar	

register many atoms, but the single- $\lambda$  cavity system has a spatially inhomogeneous atom-cavity coupling. To overcome the spatial inhomogeneity, we developed the dual- $\lambda$  confocal cavity for a 1560 nm cavity lattice and a 780 nm cavity probe. The dual- $\lambda$  confocal cavity has 175,000 cavity finesse for 780 nm and 117,000 cavity finesse for 1560 nm, which has a smaller mode area ( $w_0 = 110 \mu\text{m}$ ) at the cavity center; compared to the single- $\lambda$  cavity,  $g_0$  of a 780 nm cavity mode is  $\sim 2.7$  times larger, and  $\eta$  is  $\sim 6.7$  times larger (Table 3.1).

The single- $\lambda$  hemispherical cavity ( $L_{cav} = 9.96 \text{ cm}$ ) has a large mode volume, which can overlap with a large number of cold atoms. Using an ABCD matrix method (67), we calculated the beam waist of the cavity mode at the middle of the cavity as follows:

$$w_{hemi}^2(z) = \frac{\lambda |z^2 + (L_0 - \delta L)\delta L|}{\pi \sqrt{\delta L(L_0 - \delta L)}}, \quad (3.6)$$

where  $L_0$  is the mirror's radius of curvature  $R$ , and  $L_0 - \delta L$  is the cavity length  $L_{cav}$  (Fig. 3.3). The beam waist of the cavity mode at various places is as follows:

At the flat mirror surface:  $w_{flat,hemi}^2 = w_{hemi}^2(z=0) = \frac{\lambda}{\pi} \sqrt{(L_0 - \delta L)\delta L} = w_{0,hemi}^2$ .

At the curved mirror surface:  $w_{curv,hemi}^2 = w_{hemi}^2(z=L_0 - \delta L) = \frac{\lambda}{\pi} \frac{\sqrt{L_0 - \delta L}}{\sqrt{\delta L}} L_0$ .

At the middle of the cavity:  $w_{mid,hemi}^2 = w_{hemi}^2\left(z = \frac{L_0 - \delta L}{2}\right) = \frac{\lambda}{4\pi} \frac{\sqrt{L_0 - \delta L}}{\sqrt{\delta L}} (L_0 + 3\delta L)$ .

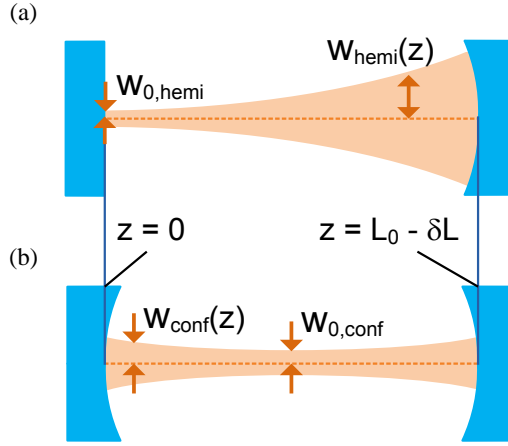


Figure 3.3: Cavity design. (a) Single- $\lambda$  hemispherical cavity. (b) Dual- $\lambda$  confocal cavity;  $L_{cav}$  is a cavity length, and  $L_0$  is the mirror's radius of curvature ( $L_{cav} = L_0 - \delta L$ ).

The dual- $\lambda$  confocal cavity ( $L_{cav} = 10.73\text{ cm}$ ) also has a large mode volume, but it is smaller than the single- $\lambda$  cavity has. The dual- $\lambda$  cavity has a 1560nm cavity lattice and a 780nm cavity probe. Using the ABCD matrix of the confocal cavity (67), the beam waist of the cavity mode is

$$w_{conf}^2(z) = \frac{\lambda}{\pi} \frac{|L_0^2 - (2z + \delta L)L_0 + 2z(z + \delta L)|}{\sqrt{L_0^2 - \delta L^2}}. \quad (3.7)$$

The beam waist of the cavity mode is as follows:

$$\text{At the curved mirror surface: } w_{curv,conf}^2 = w_{conf}^2(z=0) = \frac{\lambda}{\pi} \frac{\sqrt{L_0 - \delta L}}{\sqrt{L_0 + \delta L}} L_0.$$

$$\text{At the middle of the cavity: } w_{mid,conf}^2 = w_{conf}^2\left(z = \frac{L_0 - \delta L}{2}\right) = \frac{\lambda}{2\pi} \sqrt{L_0^2 - \delta L^2} = w_{0,conf}^2,$$

where  $w_{0,conf}$  is the beam waist at the middle of the confocal cavity.

Fig. 3.4 shows the beam waists of a single- $\lambda$  hemispherical cavity mode and a dual- $\lambda$  confocal cavity mode according to  $\delta L$ .

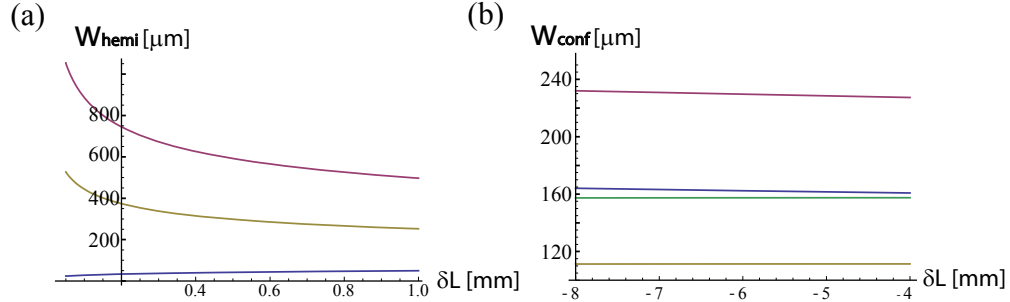


Figure 3.4: (a) Beam waist of a single- $\lambda$  hemispherical cavity mode vs.  $\delta L$  at 780nm: the red, yellow, and blue lines are  $w_{\text{curv,hemi}}$ ,  $w_{\text{mid,hemi}}$ , and  $w_{\text{flat,hemi}}$ . ( $L_{\text{cav}} = L_0 - \delta L \simeq 10\text{ cm}$ ,  $\delta L \simeq 350\text{ }\mu\text{m}$ ). (b) Beam waist of a dual- $\lambda$  confocal cavity mode vs.  $\delta L$  at 780nm and 1560nm; the red and blue lines are  $w_{\text{curv,conf},1560}$  and  $w_{\text{curv,conf},780}$ , and the green and yellow lines are  $w_{\text{mid,conf},1560}$ ,  $w_{\text{mid,conf},780}$ . ( $L_{\text{cav}} = L_0 - \delta L \simeq 10.7\text{ cm}$ ,  $\delta L = -7\text{ mm}$ ).

## Cavity Standing-wave

Because of the boundary condition, the cavity light always builds up a standing wave with nodes and anti-nodes. The 780 nm weak QND (quantum-non-demolition) probe light generates a standing wave in the cavity. The optical potential  $U_{\text{dipole}}$ , which the atoms experience due to the ac Stark shift (64), is described as follows:

$$U_{\text{dipole}} = \frac{\hbar\Omega^2}{4\Delta} = \hbar \frac{4n_{ph}g^2}{4\Delta} \quad (3.8)$$

$$= \hbar \frac{n_{ph}g_0^2}{\Delta} \sin^2(k_p z) e^{-\frac{2(x^2+y^2)}{w_0^2}}, \quad (3.9)$$

where  $\Omega^2 = 4n_{ph}g^2$  for the intracavity photon number  $n_{ph}$ . If we assume that the atoms are cold enough to be trapped and the optical lattice sites are harmonic potentials in the cavity axial and cavity transverse direction, we obtain

$$U_i = \frac{1}{2}k_i(r_i - r_{i,0})^2 \quad (r_{i=1,2,3} = x, y, z) \quad (3.10)$$

$$= \frac{1}{2}m\omega_i^2(r_i - r_{i,0})^2, \quad (3.11)$$

where the trapping frequency is  $\omega_i = \sqrt{\frac{k_i}{m}} = \sqrt{\frac{1}{m} \frac{\partial^2 U_i}{\partial r_i^2}}$ .

Using Eq. 3.9, we obtain the trapping frequencies in the optical lattice as follows:

$$\omega_x|_{y=0,z=\frac{\pi k_p}{2}} = \sqrt{\hbar \frac{4}{m_{Rb} w^2} \frac{n_{ph} g_0^2}{\Delta}} \quad (3.12)$$

$$\omega_y|_{x=0,z=\frac{\pi k_p}{2}} = \sqrt{\hbar \frac{4}{m_{Rb} w^2} \frac{n_{ph} g_0^2}{\Delta}} \quad (3.13)$$

$$\omega_z|_{x,y=0} = \sqrt{\hbar \frac{2k_p^2}{m_{Rb}} \frac{n_{ph} g_0^2}{\Delta}}. \quad (3.14)$$

In our experiments of a single- $\lambda$  cavity, there was no optical trap, and atoms falling through the hemispherical cavity ( $w_0 = 310\mu m$ ) had  $\sim 10$  milliseconds interaction time with a cavity mode. The weak QND probe beam was only used for reading out the atom-induced light shift. The lifetime of the trapped atoms in the 1560nm cavity lattice is longer as 1.1s, and the atomic coherence time is 57ms.

## Cavity Chamber

Our Zerodur cavity chamber is compact,  $\lesssim 650\text{cm}^3$ , and designed for a mobile-platform atom-based sensor (Fig. 3.5). The entire cavity chamber is constructed from Zerodur, which has very low helium permeability and a near-to-zero thermal expansion coefficient ( $\simeq 10^{-8}/\text{K}$ ) at room temperature. This chamber encompasses a current driven rubidium dispenser (Alvatec) and a region for a two-dimensional MOT (2D-MOT) for preparing a collimated beam of atoms that passes through a hole (1.5 mm in a diameter) into the main chamber to load a three-dimensional MOT. Extension tubes attached to the main chamber hold the cavity mirrors. The Zerodur glass contacts, except the mirror end-caps, are held together with a Sodium Silicate molecular bonding agent, and the glass-metal contacts for the ion-pump and the dispenser are sealed with Indalloy. The mirror end-caps, to which the mirror substrates are epoxied to, are attached to the extension tubes with a thin layer of high-temperature epoxy (crystallization at  $\sim 120^\circ\text{C}$ ), allowing a final fine-tuning of the mirror alignments while monitoring the cavity optical transmission spectrum as the epoxy

cures during the construction of the chamber. The epoxy contacts of the chamber can endure a baking temperature of  $120 - 130^\circ\text{C}$ , permitting us to reach vacuum pressures smaller than  $\sim 10^{-9}$  mbar, maintained by an ion-pump (5L/s). At the end of the 2D MOT chamber (Fig. 3.5 (a), (b)),  $^{87}\text{Rb}$  atoms are released from a dispenser source (Alvatec), and the laser-cooled 2D MOT atoms are transferred to the 3D MOT chamber. The 3D MOT atoms are loaded at the cavity center, and those atoms are further cooled down via far-detuned MOT and optical molasses stages.

The two mirrors, coated for high reflectivity at both 780 nm and 1560 nm (by Research Electro-Optics), are used to construct an optical cavity whose modes overlap with the MOT at the center of the chamber. The relevant cavity parameters together with atom-cavity coupling strengths are given in Table 3.1.

The single- $\lambda$  cavity chamber (Fig. 3.6 (a)) has a high-finesse hemispherical cavity with a PZT, and the gaps for the PZT electrodes were filled with low-temperature epoxy (Fig. 3.7 (a)). Low-temperature epoxy cure, filling the gap, melts at  $80^\circ\text{C}$ , and the cavity PZT can be damaged if the temperature exceeds  $120^\circ\text{C}$ . Because of the low-temperature baking ( $\sim 70^\circ\text{C}$ ), the hemispherical cavity chamber has only an  $\sim 10^{-8}$  mbar vacuum. The hemispherical cavity configuration with a PZT needs more freedom to align because the finesse of a hemispherical cavity is more sensitive to the mirror alignment than that of a confocal cavity, and the PZT electrode needs a feedthrough to a PZT driver.

The dual- $\lambda$  cavity chamber (Fig. 3.6 (b)) has a high-finesse confocal cavity without a PZT, and the contacts between the mirror end-cap and the cavity tubes were cured by high-temperature epoxy (Fig. 3.7 (b)). For the control of its length, we can still tune the cavity resonance frequency by more than one free spectral range (FSR)  $\Delta\nu_{\text{fsr}}$ , albeit quite slowly, through the thermal expansion of the mirror substrates controlled by the heat patches on the extension tubes. High-temperature epoxy (glass temperature of  $120^\circ\text{C}$ ) which does not contain a PZT seems to be a good solution for a chamber that needs UHV and therefore, needs high-temperature baking. Because of high-temperature baking (over

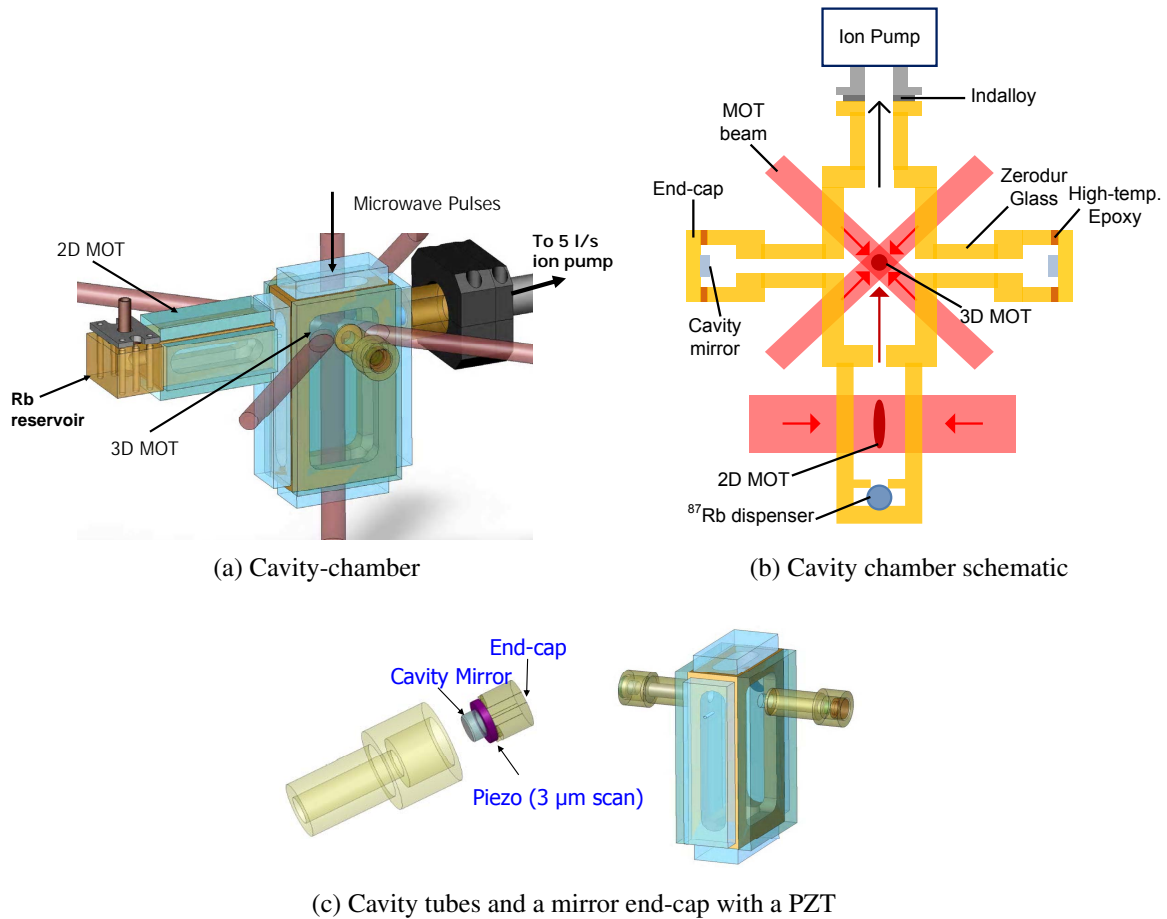


Figure 3.5: Cavity chambers (a) Zerodur cavity chamber consists of a 2D MOT chamber, 3D MOT chamber,  $^{87}\text{Rb}$  dispenser, cavity tubes and a cavity, and an ion pump. (b) Schematic of the cavity-chamber (Dual- $\lambda$  cavity-chamber); the near-confocal cavity has the 780 nm and the 1560 nm and cavity modes. (c) Mirrored-end-cap is a Zerodur end-cap with a cavity mirror and a PZT, and it is glued to the cavity tube.

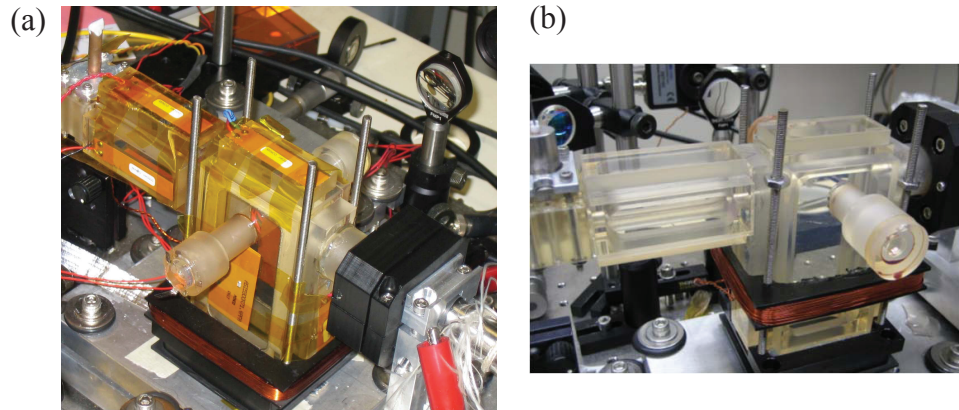


Figure 3.6: Pictures of cavity chambers (a) Single- $\lambda$  hemispherical cavity chamber with a PZT. (b) Dual- $\lambda$  confocal cavity chamber without a PZT.

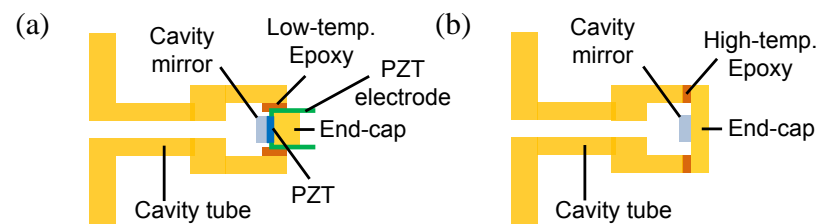


Figure 3.7: Schematics of cavity tubes and mirror-ends. (a) Single- $\lambda$  cavity with a PZT. (b) Dual- $\lambda$  cavity without a PZT.

$120^{\circ}\text{C}$ ), the confocal cavity chamber has an  $\sim 10^{-10}$  mbar-level vacuum. The mirror end-caps were glued with high-temperature epoxy at the end-contact of the cavity tubes; the confocal cavity can be aligned only with 2D of freedom, and it does not need a gap for PZT electrodes. High temperature epoxy cure needs more care because a thick and asymmetric epoxy layer results in unbalanced shrinking forces that can crack the Zerodur glass during the crystallization.

To align the cavity mirrors for a high finesse (Fig. 3.8), we used two precise gimbal mounts held to the 3D translation stages. For vibration isolation, we used vibration-isolated multi-stacks of platforms for our mirror mount system. For the cavity alignment, we precisely set the cavity length, i.e. the distance between the two cavity mirrors, using 3D translation stages. Then, we observe the interference fringe patterns. After precise alignment, we can see stronger fringe patterns, and we can also see the axial modes and the transverse modes of the cavity. While sweeping a laser frequency, we tune the alignment of cavity mirrors for a better light coupling to the cavity. Through the cavity transmission, the higher modes usually show up first and the lowest modes show up later. As we try to make the lower modes larger one by one, the lowest mode  $\text{TEM}_{00}$  becomes amplified much more than the other modes. Then, we suppress other cavity modes more and check the cavity finesse by the cavity ringdown measurement (Fig. 3.8).

For measuring the cavity finesse, we drove light pulses with a pulse time width of several tens of  $\mu\text{s}$ , which is close to the cavity lifetime. The AOM switch can cut the continuous laser beam within a few hundred nano seconds. We saw the cavity ring-down over the time scale, and measured the  $\frac{1}{e}$  time (Fig. 3.8 (a)). As we scanned our probe frequency, the probe became on-resonance with the cavity resonance frequency. We could see multiple peaks over several FSRs of frequency sweeping. Magnifying the spectrum, the transmission peaks generated by frequency scanning also showed a cavity ring-down with a proper transimpedance amplifier.

## Cavity Lock Scheme of a Single- $\lambda$ Cavity

This subsection presents the cavity lock scheme of the single- $\lambda$  cavity system discussed in Chapter 4. For single- $\lambda$  cavity experiments, we used two cavity-lock servos (Fig. 3.9 (a)).

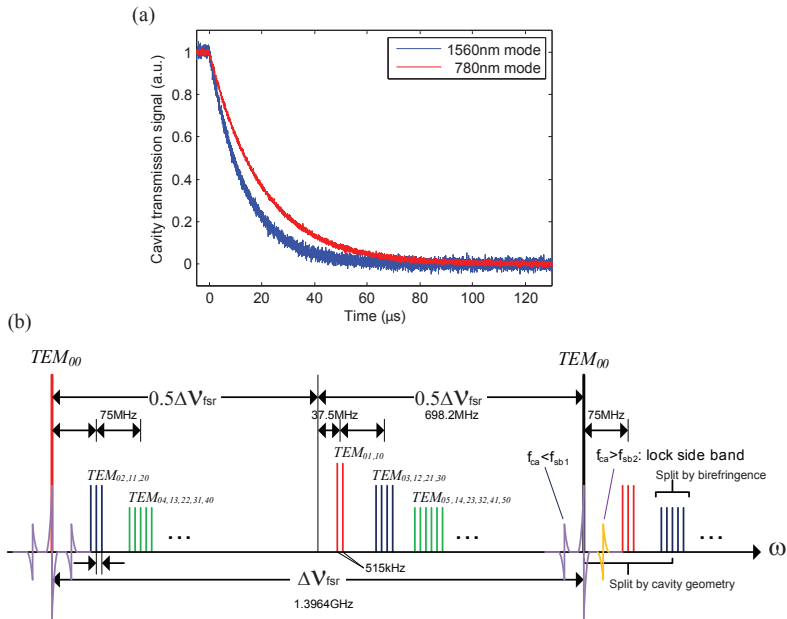


Figure 3.8: (a) Cavity ring-down measurements of 1560nm and 780nm cavity modes. At time  $t = 0$ , an incident cavity probe is switched off using an acousto-optic modulator. The measured lifetimes are  $\tau_{780} = 19.9 \mu\text{s}$  and  $\tau_{1560} = 13.3 \mu\text{s}$ . (b) Cavity transmission spectrum: For the dual- $\lambda$  confocal cavity ( $\delta L > 0$ ), the longitudinal mode spacing is  $\Delta\nu_{\text{fsr}} = 2\pi\frac{c}{2L} = 1.3964 \text{ GHz}$ . The transverse mode spacing is  $\Delta\nu_{\text{tms}} = \frac{1}{2}\Delta\nu_{\text{fsr}} + 37.5 \text{ MHz}$  (67), and this results in the spacing  $2\Delta\nu_{\text{tms}} - \Delta\nu_{\text{fsr}} = 75 \text{ MHz}$  between nearest transverse modes.

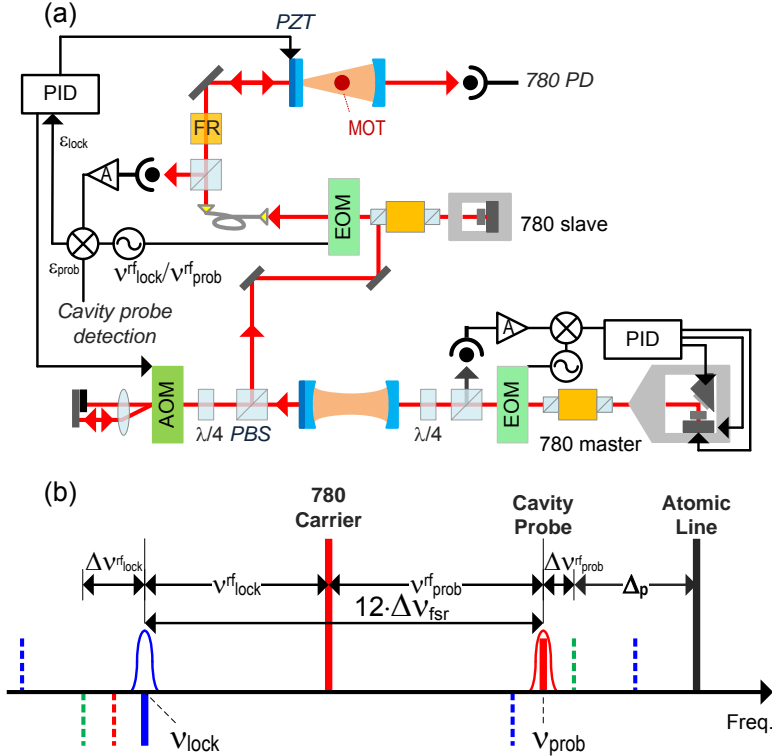


Figure 3.9: Single- $\lambda$  cavity lock scheme of one master 780 nm laser and a 780 nm reference cavity. This single- $\lambda$  cavity is used for observing collective normal mode splitting and measuring anti-spin-squeezing (Chapter 4). (a) Experimental setup with one master lasers of 780 nm. (b) Cavity modulation scheme of a 780 nm cavity lock sideband and a 780 nm cavity probe;  $\Delta v_{fsr} = 2\pi \cdot 1.505$  GHz is the cavity frequency spectral range;  $v_{prob}^{RF} = 2\pi \cdot 9.065$  GHz the cavity probe's modulation frequency;  $v_{lock}^{RF} = 2\pi \cdot 8.995$  GHz, the cavity lock's modulation frequency. There are two cavity modes of the locking beam and the QND probe beam with  $12 \cdot \Delta v_{fsr}$  ( $\sim 2\pi \cdot 18.06$  GHz) apart, and the carrier light is not resonant with the cavity. AOM, acousto-optic modulator; EOM, electro optic modulator;  $\lambda/2$ , a half wave-plate;  $\lambda/4$ , a quarter wave-plate; PID, cavity lock box; FR, Faraday rotator.

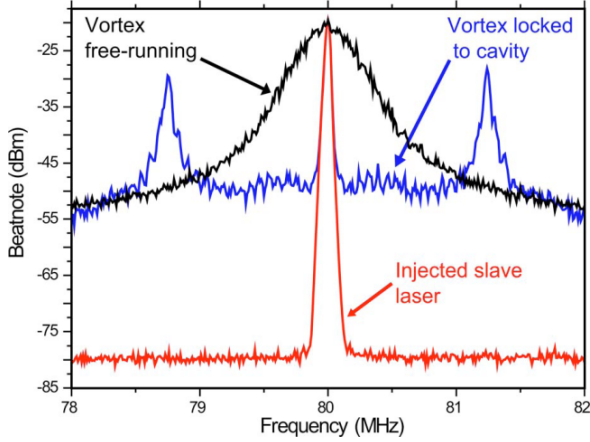


Figure 3.10: Self-heterodyne beat note of the low-noise carrier light after a reference cavity and an injection lock (6).

With the first cavity-lock servo (Fig. A.1), a reference cavity, and an injection lock, we prepare the low-noise QND probe carrier light; a 780nm master laser is locked to a high-finesse reference cavity (68). That feedback can bring us to have the linewidth of the cavity transmitted light down to  $\sim 7.4\text{ kHz}$  (FWHM) (6), and the fluctuation of the transmitted light is suppressed using an injection lock to a slave diode laser (Fig. 3.10). The second cavity-lock servo (Fig. A.2) locks our science cavity to the light through a cavity PZT, varying the cavity resonant frequency, and a double-pass AOM, modifying the frequency of the probe light carrier.

For this experiment, we prepared two cavities, both of which are high-finesse cavities made of Zerodur glass. The first cavity is a confocal reference cavity shown in Fig. 3.9 (a), which has a length of 10cm and a 160,000 finesse. Using this high-finesse reference cavity with no vacuum and with thermal stabilization, we narrowed the linewidth of the QND probe carrier, and we thereby obtained a low-noise QND probe carrier. The reference cavity is free running, and our NewFocus Vortex laser (a Littman-type external-cavity diode laser) is locked to the reference cavity using the Pound-Drever-Hall locking technique with a high-frequency feedback (68; 69; 70; 71; 72; 73; 74; 75). The 300kHz Vortex laser's linewidth is reduced to 7.8kHz following the reference cavity around the wavelength of  $\lambda = 780\text{ nm}$ . This cavity lock technique changes the frequency noise to the

amplitude noise. Following the cavity lock, the QND probe carrier light is injected into a slave laser. The amplitude noise is suppressed because the slave laser only follows the injection seed's frequency. The reference cavity locking scheme is as follows: The Vortex laser's modulation frequency is 30 MHz, and the reflected beat note is detected using a high-frequency photodiode (Hamamatsu G4176). The demodulated error signal is fed back to the laser after a cavity locking servo in three frequency paths (68). Following a high-pass filter, the high-frequency feedback is directly applied to the diode head and provides bandwidth greater than 1 MHz. An intermediate frequency feedback is applied through the laser current controller. Finally, the low-frequency feedback (400 Hz) is applied to the PZT on the external grating of the Vortex. Based on the laser spectrum from a self-heterodyne beat note, we observed significant linewidth reduction, as shown in Fig. 3.10.

The second cavity surrounding the atoms in a vacuum is a hemispherical science cavity with a 10 cm ( $\Delta v_{\text{fsr}} \sim 2\pi \cdot 1.505 \text{ GHz}$ ) cavity length and a 205,000 finesse. The linewidth  $\kappa$  is  $\simeq 3.7 \text{ kHz}$  (HWHM). The cavity input beam is linearly polarized, and we use a Faraday rotator to rotate linearly polarized light rather than a  $\lambda/4$  wave plate. The hemispherical configuration provides a large mode beam waist  $\sim 310 \mu\text{m}$ , and the large mode volume at the center of the cavity overlaps the magneto-optically trapped atoms. The double FM technique is used for a cavity lock with dispersive measurements on the second sideband.

A phase modulator with multiple frequencies modulates the QND probe beam, in which each RF sideband frequency is independently controllable. We set each frequency in such a way that the separation is an integer multiple of the FSR (frequency spectral range). Then, the locking beam and the QND beam couple to the cavity modes. The science cavity follows the locking beam, and the error signal (AC) from the beat note between carrier light and locking beam feeds back to the PZT of the cavity and the double pass acousto-optic modulator (AOM) before the injection lock into the slave laser of the QND beam. Using this technique, the far-detuned probe stabilized to the science cavity experiences the atoms' index of refraction, and the atom-induced cavity resonance shift provides the information of an atom number. Using the dispersive signal, we convert the frequency shift to the number of atoms. The transmitted cavity light from the reference confocal cavity is then used to injection lock a slave laser, which suppresses the amplitude noise. The slave light is next locked to the science cavity containing atoms, and the double FM technique is used to

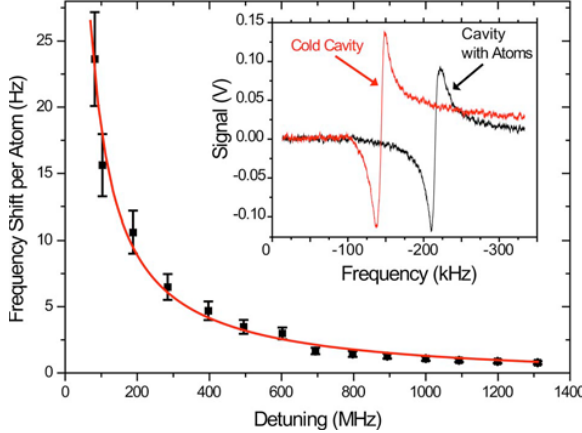


Figure 3.11: Atom-induced cavity shift (6).

provide a probe frequency. The minimum optical power in the locking sideband required for a stable cavity lock is a few nano watts. The second sideband at  $2\pi \cdot 9.1\text{GHz}$  (six FSRs) serves as the dispersive probe and is generated by an EOM (NewFocus model 4851). The beat note is detected in the reflection from the cavity with a photodiode (Hamamatsu G4176) followed by a broadband amplifier. For our parameters, photon-shot-noise-limited detection is obtained with 5mW of carrier intensity.

The photodiode signal is separated into two amplification chains. A 100MHz demodulated error signal is used for the cavity lock servo. High-frequency feedback (60kHz bandwidth) is applied to an AOM via a proportional and double-stage integrator loop. Low-frequency feedback (below 400Hz) is applied to the science cavity PZT. This cavity lock allows us to probe atoms stably with the cavity probe (the setup shown in Fig. 3.9 (a)).

Using the measurement of the dispersive light shift  $\delta v_{at}$  from the  $^{87}\text{Rb}$  atomic cloud with a typical size of  $\sim 300\mu\text{m}$ , we can read the atom number. The initial laser-cooled atoms in the cavity are presented in (5). In the far detuned limit, the light shift is

$$\delta v_{at} = \frac{N_{at}g^2}{\delta}, \quad (3.15)$$

where  $g$  is the atom-cavity coupling ( $g/\hbar = 2\pi \cdot 53\text{kHz}$ ), and  $\delta$  is the detuning from the atomic resonance. Fig. 3.11 shows the frequency shift per atom scaling inversely with  $\delta$ .

The inset in Fig. 3.11 shows the frequency shifted dispersive profile taken with 50,000 atoms loaded in the cavity mode with  $\delta \approx 1$  GHz and an optical power of 1 nW in the probe sideband. By averaging over a 400  $\mu$ s window away from the atom-cavity resonance, we observe a signal-to-noise ratio of 400 : 1. This allows us to have the resolution limit of  $< 10$  atoms, significantly below the shot-noise limit ( $\sim 220$  atoms). Combined with an inferred spontaneous emission rate of 104 events/s, this demonstrates that our FM technique can provide the sensitivity needed to detect sub-atom-shot-noise fluctuations in future quantum non-demolition measurements.

## Cavity Lock Scheme of a Dual- $\lambda$ Cavity

This subsection presents the cavity lock scheme of the dual- $\lambda$  cavity system of Chapter 5, Chapter 6, and Chapter 7.

A cavity lock scheme of two master 780 nm and 1560 nm lasers and a 780 nm reference cavity was firstly developed for studying dual- $\lambda$  cavity's properties (Fig. 3.12). This cavity lock scheme is updated later using one master 1560 nm laser and a 1560 nm reference cavity with a frequency-doubler (Fig. 3.13). In both cases, we stabilize a master laser to a high finesse reference cavity ( $\sim 5$  MHz lock bandwidth) and have a slave injection lock, in order to generate a low-noise probe carrier. The scheme of two master lasers is able to lock both cavity modes independently to the science cavity, whereas with the scheme of one master laser and a PPLN, the frequency-doubled cavity probe follows the master laser's cavity lock. Both schemes are similar, and both use external cavity diode lasers as master lasers. The scheme of two master lasers guarantees that both cavity modes stay tightly locked while the cavity-chamber's temperature drifts. The scheme of one master laser lengthens the coherence time of trapped atoms because a cavity lock sideband (780 nm) that results in residual light shifts is unnecessary.

The cavity lock scheme of one master laser is as follows: All the spectral lines that are used to drive the desired cavity modes are generated from one external-cavity diode laser operating at 1560 nm (New Focus Vortex,  $\sim 300$  kHz) that is effectively stabilized to a cavity mode. The schematic for the laser-cavity stabilization and the generation of the required spectral lines are shown in Fig. 3.13. The 1560 nm master laser is first actively

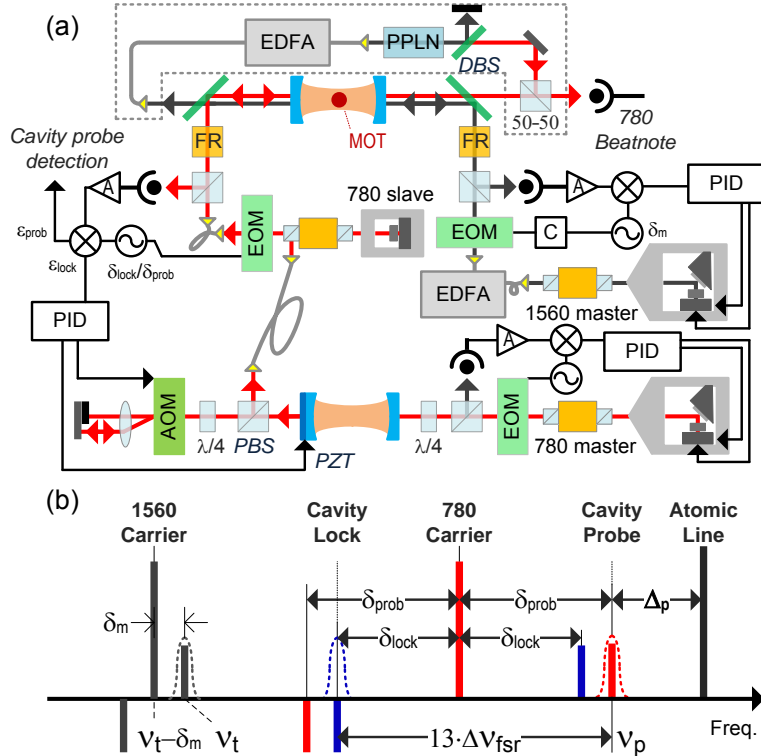


Figure 3.12: Dual- $\lambda$  cavity lock scheme of two master 780 nm and 1560 nm lasers and a 780 nm reference cavity. (a) Experimental setup with two master lasers of 780 nm and 1560 nm. (b) Cavity modulation scheme of a 1560 nm cavity optical lattice and a 780 nm cavity probe;  $\nu_t$  is the cavity lattice's frequency;  $\delta_{prob}$ , the cavity probe's modulation frequency;  $\delta_{lock}$ , the cavity lock's modulation frequency;  $\delta_m$ , the lattice's modulation frequency; DBS, dichroic beam splitter; AOM, acousto-optic modulator; EOM, electro optic modulator;  $\lambda/2$ , a half wave-plate;  $\lambda/4$ , a quarter wave-plate; 50-50, 50%-50% beam splitter; PID, cavity lock box; A (green), (variable-gain) amplifier; C, variable attenuator; FR, Faraday rotator; EDFA, erbium doped fiber amplifier.

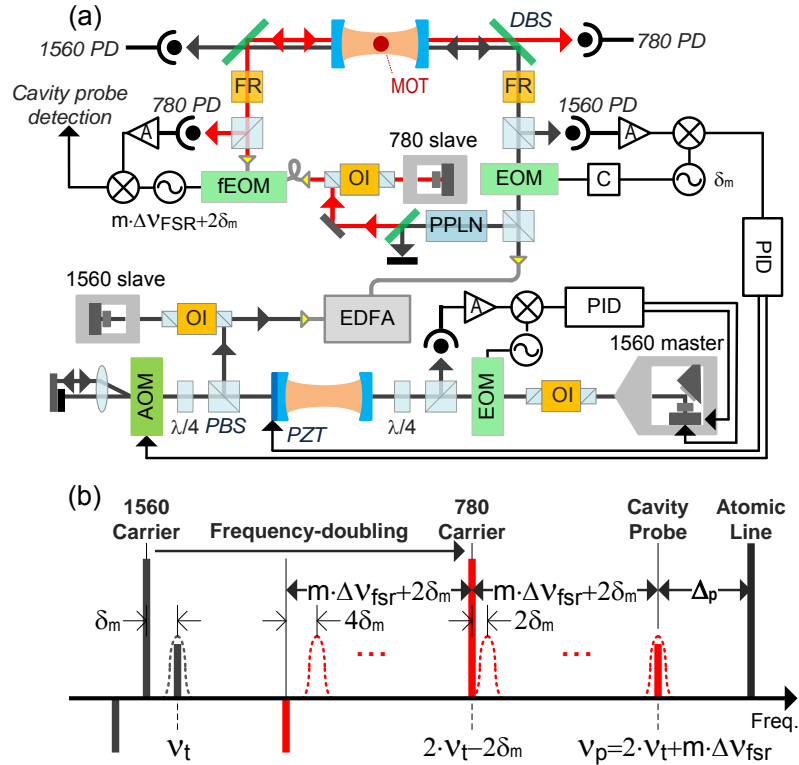


Figure 3.13: Dual- $\lambda$  cavity lock scheme of one master 1560nm laser and a 1560nm reference cavity with a frequency-doubler (PPLN). (a) Experimental setup with one 1560nm master laser and a frequency-doubler. (b) Cavity modulation scheme of a 1560nm cavity optical lattice and a frequency-doubled cavity probe (780nm);  $v_t$  is the cavity lattice's frequency;  $2v_t + m \cdot \Delta V_{\text{FSR}}$ , the cavity probe's frequency;  $\delta_m$ , the modulation frequency of the lattice beam; FOM, fiber-optic modulator; PPLN, periodically-poled lithium niobate. DBS, dichroic beam splitter; AOM, acousto-optic modulator; EOM, electro optic modulator;  $\lambda/2$ , a half wave-plate;  $\lambda/4$ , a quarter wave-plate; 50-50, 50%-50% beam splitter; PID, cavity lock box; A, (variable-gain) amplifier; C, variable attenuator; FR, Faraday rotator; EDFA, erbium doped fiber amplifier. The dotted box is the additional setup for beat note measurement.

frequency stabilized ( $\sim 5\text{ MHz}$  lock bandwidth) to an additional reference cavity, very similar in parameters to our main cavity, via the Pound-Drever-Hall method (69) (PDH) with a circuitry similar to the one described in reference (68). A 1560nm slave diode laser, whose output is later amplified by an erbium-doped fiber amplifier (EDFA) to  $\sim 250\text{ mW}$ , is injection locked to the light transmitted by the reference cavity for circumventing the remaining amplitude variations in the transmitted light. The low-noise 1560nm light emerging from the EDFA is split into two paths, one of which gets the frequency doubled to 780nm in a periodically-polled Lithium Niobate (PPLN) waveguide followed by injection into a 780nm slave diode laser. The other path is, firstly, phase-modulated with an electro-optical modulator (EOM) at  $\delta_m \sim 40\text{ MHz}$  and one of the generated sidebands is locked to the main cavity via the PDH method ( $\sim 100\text{ kHz}$  lock bandwidth), using the acousto-optic modulator (AOM) situated before the 1560nm slave diode laser and the reference cavity PZT as the fast and slow frequency feedback elements respectively. In effect, once locked, the 1560nm master laser follows a resonance frequency of the reference cavity, which in turn follows a resonance frequency of the main cavity as its length drifts. Likewise, the 780nm light automatically follows a cavity resonance that is an octave away. In this regime, the unnecessary of having to lock independently the 780nm light to the cavity prevents having permanent additional 780nm sidebands coupled to the cavity for locking purposes, avoiding undesired dephasing effects on the atoms due to inhomogeneous light shifts. The depth of cavity lattice depth can vary by as much as a factor of 100. We are able to turn on the cavity optical lattice optimally for adiabatic atom loading into the lattice.

The schematic of the generated optical frequencies is shown in Fig. 3.13 (b). The 1560nm sideband that is locked to the cavity serves as the 1D optical lattice inside of the cavity, and one of the sidebands generated by the broadband fiber electro-optic modulator (fEOM) (at  $\sim 6\text{ GHz}$ ) following the 780nm slave laser serves as the probe mode that couples near-resonantly to the atoms in our experiments. Both of these modes are  $\text{TEM}_{00}$  in the transverse profile. The cavity read-out, i.e., identification of the resonance frequency of the probe mode under the influence of the atoms, is accomplished with a heterodyne measurement in a manner identical to the generation of an error signal in the PDH method. In particular, the beat-note signal between the reflected 780nm carrier obtained on a photodiode is demodulated electronically to DC, and the resulting signal is

observed on an oscilloscope while the probe mode resonance. A microwave horn is located outside of the chamber to drive coherently the  $\sim 6.834\text{ GHz}$  hyperfine clock transition ( $|F = 1, m_f = 0\rangle \leftrightarrow |F = 2, m_f = 0\rangle$ ) that we are interested in of the  $^{87}\text{Rb}$  atoms.

### 3.3 Apparatus

This section presents the optical and electrical system for laser cooling and trapping technique, control electronics, and sensor hardware. The system is designed for a mobile platform atomic sensor.

#### Laser System for MOT

A compact laser system ( $10'' \times 10'' \times 2''$ , Fig. 3.14) and a small science cage ( $14'' \times 12.6'' \times 9''$ , Fig. 3.16) with DSP (Digital Signal Processor)-controlled electronics (Fig. 3.15) were designed for future portable applications. All outputs of the lasers from the compact laser system were coupled into optical fibers connected to the main science cage shown in Fig. 3.16.

The compact laser system combined with DSP-controlled circuits was designed for a mobile platform. The eagleyard DFB (Distributed Feedback Laser) diode lasers with 2MHz (FWHM) linewidth were used for repumping and cooling lasers. The output power was about 80mW at room temperature. We need the repump light for the  $^{87}\text{Rb}$  D2 transition from  $F = 1$  to  $F' = 2$ , and the wavelength is 780.232 nm. The wavelength of the cooling light for the transition from  $F = 2$  to  $F' = 3$  is 780.246 nm. Two compact optical isolators prevent optical feedback, and we use compact walk-off crystals as polarized beam splitters. The cooling light seed is amplified with a MOPA (master oscillator power amplifier). A small rubidium cell inside the system is used for the laser lock. We precisely tune the frequency of the laser in the range of several tens of MHz by an EOM and AOM.

#### Control Electronics

Control electronics (Fig. 3.15) are based on a host PC and DSP control board (Innovative SBC6711 and Servo16, TI TMS320C DSP series). The host PC program communicates

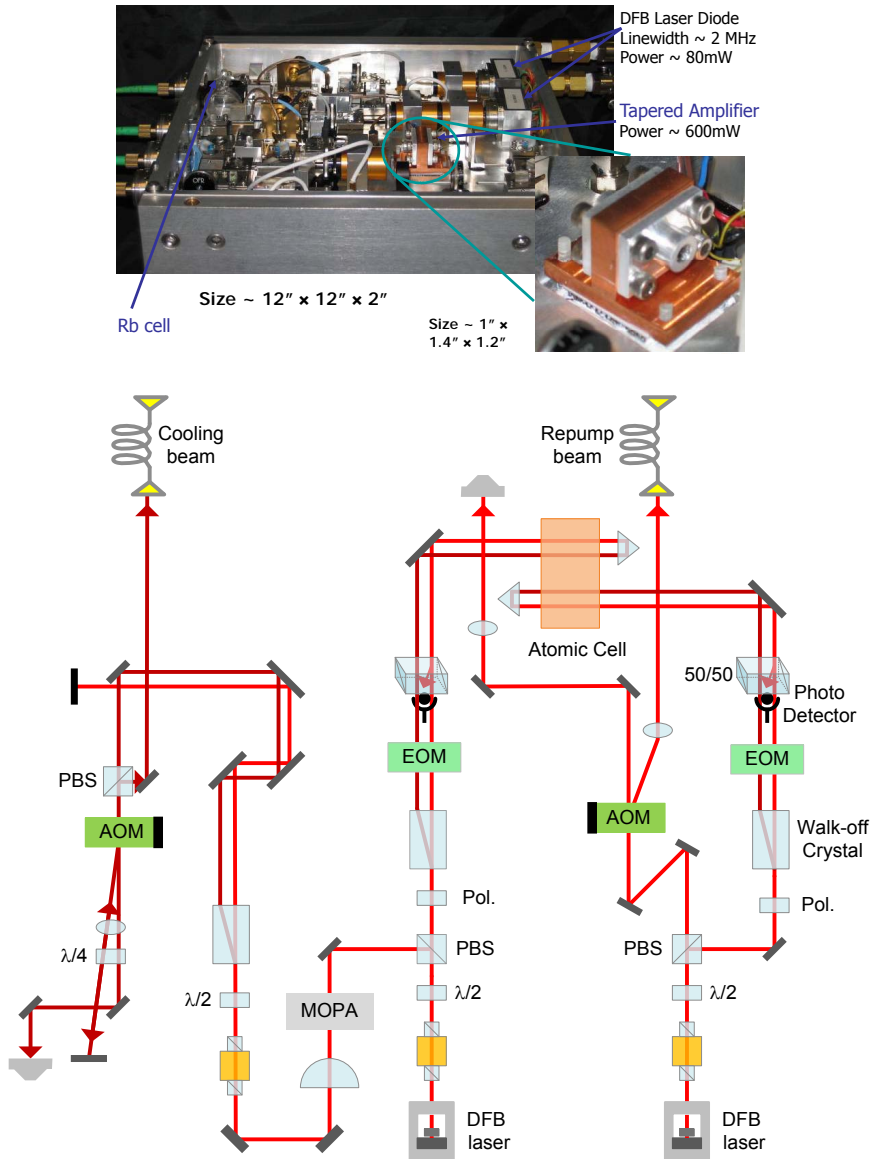


Figure 3.14: Compact laser system and its schematic for cooling and repumping beams; AOM is acousto-optic modulator; EOM, electro optic modulator;  $\lambda/2$ , a half wave-plate;  $\lambda/4$ , a quarter wave-plate; 50-50, 50%-50% beam splitter; PBS, polarized beam splitter.

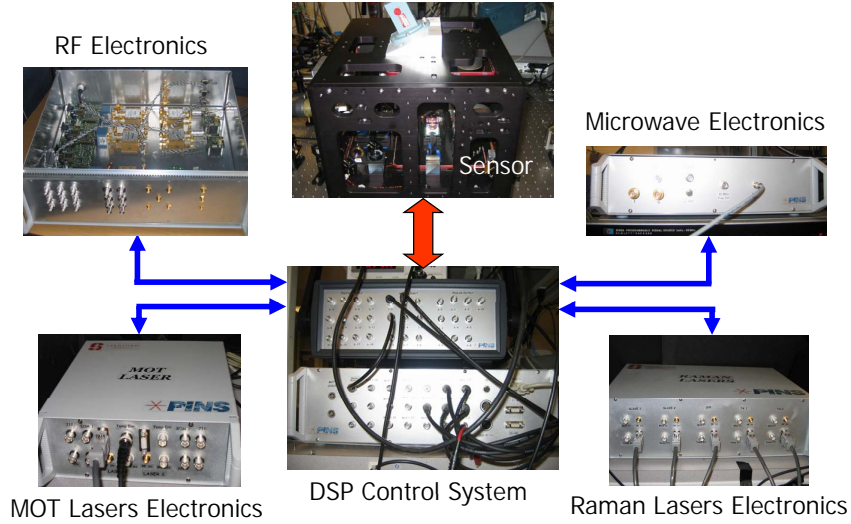


Figure 3.15: Control system

with the DSP control program in the DSP via the USB (Universal Serial Bus). Usually, the host PC sets in advance various values for the measurement process, and the DSP board sends analog, digital, and SPI (Serial-Port Interface) control signals to each electric circuit and acquires analog data input. Most of the circuit boards are controlled by SPI communication, but some are directly controlled by the DSP analog output or digital output signals. The DSP control board has 16 DAC (Digital-Analog Converter) outputs and 16 ADC (Analog-Digital Converter) inputs.

There are various DSP-controlled circuit boards, such as the laser diode current controllers, laser diode temperature controllers,  $^{87}\text{Rb}$  spectrum lock circuits, offset lock circuits, EOM drivers, current drivers for bias magnetic field and MOT magnetic fields, and programmable frequency synthesizers. We also have microwave control electronics for the microwave atomic clock transition and the multiple frequency modulation. High-power RF amplifiers, DDS (Direct Digital Synthesizer), and single sideband mixers were used for microwave pulse generation.

## Sensor Hardware

The small science cage ( $14'' \times 12.6'' \times 9''$ ) was developed for mobile platforms. In the cage, we set up the vacuum cavity chamber with various optics. An atomic interferometer can be used as a sensor for inertial navigation systems, and our atom-cavity technique can improve the performance of atomic inertial navigation sensors by suppressing the quantum measurement noise. In the X, Y plane of the chamber, two axes have already been used for the cavity axis and the rubidium ion-pumping axis. In addition, two  $45^\circ$ -off optical axes from the cavity axis and the ion-pumping axis are used for X, Y 3D MOT beam paths.

The cooling and repump beams (Fig. 3.16 (b)) are coupled to the science frame, and the size of the beams is optimized with lenses. The diameter of the 3D MOT beams is about half an inch, and their polarization is also optimized by a polarizer inside the tube. The cooling and repump beams are split by several wave plates in the cage for 2D MOT and 3D MOT optical paths. After going through the first  $\frac{\lambda}{4}$  wave plate and reflecting off the second  $\frac{\lambda}{4}$  wave plate mounted on a mirror, two counter-propagating beams of  $\sigma^+$  and  $\sigma^-$  polarizations capture atoms around the central region of the cavity.

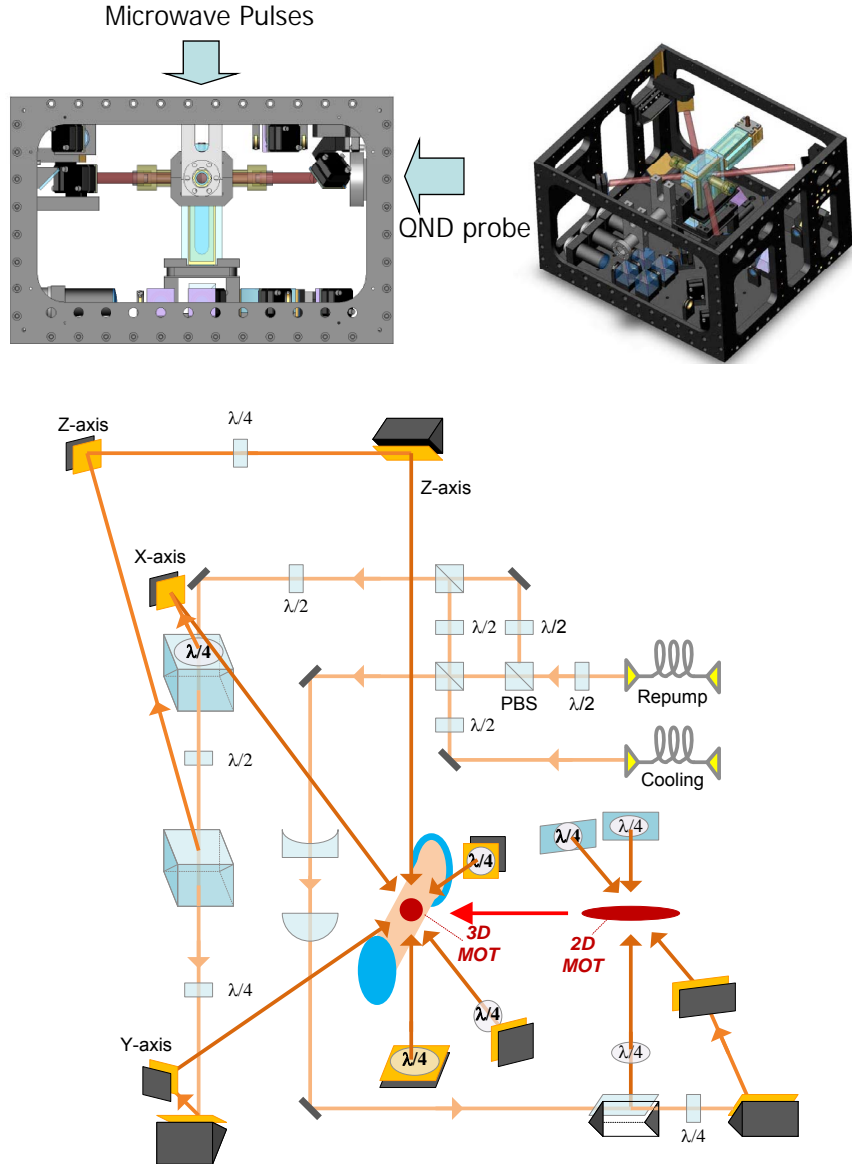


Figure 3.16: Sensor hardware; the science cage with a cavity chamber; AOM is acousto-optic modulator; EOM, electro optic modulator;  $\lambda/2$ , a half wave-plate;  $\lambda/4$ , a quarter wave-plate; 50-50, 50%-50% beam splitter; PBS, polarized beam splitter.

# Chapter 4

## Review and Motivation

In our cQED system, a cavity mode can be coupled with many atoms due to a large enough cavity mode volume. Many-atom-cavity dressed state in the collective strong coupling regime allowed us to measure the collective normal-mode splitting which confirms a large collective cooperativity (5) : The cQED system with a large collective cooperativity has the potential to generate the spin-squeezed state of atoms. After confirming the large collective cooperativity, we prepared the cavity-aided non-demolition probe for spin-squeezing, and we observed the anti-spin-squeezing resulting from the back-action measurement: The measurement of anti-spin-squeezing can be the evidence of spin-squeezing (4). Using the apparatus described in the previous chapter, the laser-cooled  $^{87}\text{Rb}$  atoms interact with the weak QND probe light in a high-finesse cavity. The cavity-aided continuous QND measurement senses the collective pseudospin of the atoms, which generates the conditional spin-squeezed state of the atoms by detecting the photons.

### 4.1 Collective Normal Mode Splitting

At the beginning of this cQED project, we ascertained that a high-finesse cavity with a large collective cooperativity is an essential tool to generate the spin-squeezed state of atoms. We designed a cavity chamber system with a high-finesse hemispherical single- $\lambda$  cavity; two cavity tubes with high reflective mirrors were attached to the chamber. The many-atom-cavity interaction between a large number of laser-cooled atoms and an off-resonant weak

(cavity) probe beam could realize the spin-squeezed state of atoms (17). The interaction strength is dependent on the optical depth of the atomic cloud. A higher cavity finesse and many atoms coupled to a cavity mode increase the optical depth because the cavity mode inside the high-finesse cavity can stay longer to interact more with many atoms. Incomplete overlapping between the atomic cloud and the cavity beam profile limits a number of atoms coupled to a cavity mode and results in an inhomogeneous spatial atom-cavity coupling. A properly large cavity mode volume (or tightly confined atoms to a cavity mode by a trapping potential) with an appropriately strong atom-cavity coupling is necessary to increase a number of atoms coupled to a cavity mode, decrease the spatial inhomogeneity, and achieve a large collective cooperativity, which is expected to produce spin-squeezed states. An initially prepared spin-squeezed state can enhance the phase sensitivity of the atomic sensors. The ratio  $\zeta$  of the interferometric sensitivity of the spin-squeezed states,  $\Delta\Phi_{SSS}$ , to that of the coherent spin states,  $\Delta\Phi_{CSS}$ , represents the degree of spin-squeezing (10; 18; 19) and is given by

$$\zeta = \frac{\Delta\Phi_{SSS}}{\Delta\Phi_{CSS}} = \left( \frac{\kappa\gamma}{Ng^2} \right)^{\frac{1}{4}} = \left( \frac{1}{2C} \right)^{\frac{1}{4}}, \quad (4.1)$$

where  $N$  is the atom number,  $g$  is the cavity coupling parameter,  $\gamma$  (HWHM) is the atomic decay rate, and  $\kappa$  (HWHM) is the cavity decay rate. As we see in Eq. 4.1, the spin-squeezing is improved by the collective cooperativity  $C$ . The collective cooperativity  $C$  of the atom-cavity system is

$$C = \frac{Ng^2}{2\kappa\gamma}, \quad (4.2)$$

where  $(g, \kappa, \gamma) = 2\pi \cdot (53, 3.7, 3030)$  kHz (HWHM); all the single- $\lambda$  cavity parameters are shown in Table 3.1.

Strong atom-cavity coupling ( $\frac{g^2}{2\kappa\gamma} \gg 1$ ) and a large number of atoms coupled to a cavity mode increases the collective cooperativity  $C$ , but stronger atom-cavity coupling requires a smaller cavity mode volume that overlaps with a smaller number of atoms. Therefore, the intermediate atom-cavity coupling ( $\frac{g^2}{2\kappa\gamma} \sim 1$ ) with a properly large cavity mode volume results in collective strong coupling ( $C \gg 1$ ) and can increase the degree of the spin-squeezing. The performance of a practical sub-shot-noise sensor is not only dependent

on  $\zeta$  but also on optimizing the overall sensitivity  $\Delta\Phi_{\text{SSS}} = \frac{\zeta}{\sqrt{N}}$ . To increase the overall sensitivity, we require a large mode volume such that the cavity probe interacts with a large number of the atoms. When the atomic cloud does not precisely overlap the cavity probe, the degree of spin-squeezing is limited by inhomogeneous coupling. There exists a difference between the effective atom number coupled to a cavity mode and the actual atom number obtained by a laser-cooling and -trapping. To study the cavity regime related to quantum metrology applications, we used the high-finesse hemispherical cavity with a large cavity mode volume and a large number of atoms,  $N \sim 2 \times 10^5$ . We demonstrated the normal-mode splitting of dressed states of the atomic ensemble and the cavity modes. As we tuned the probe light from the cavity resonance, we observed sub-natural atomic linewidth ( $\sim 1.74 \text{ MHz (HWHM)}$ ) normal mode splitting, from which we can infer the collective cooperativity  $C$ .

When  $C \gg 1$ , the cQED regime is known as the collective strong coupling regime. To study this regime, many atoms are coupled with a cavity mode by a cavity with a large enough mode volume or with a trapping potential. In this regime, many-atom-cavity dressed states result in collective normal mode splitting according to the atom number. The uncoupled system consists of all  $N$  atoms in the ground-state with one photon state or  $N - 1$  atoms in the ground-state (one excited state atom) with zero photon state. The coupled system exchanges energy, and emission of a photon is reversible. In the cavity transmission, there exists the atom-number dependent peak splitting.

In the many-atom-cavity dressed states, we assume that two-level atomic ensembles interact with a single-mode field in a photon number eigenstate. The hyperfine ground state of  $|F = 2\rangle$  is regarded as  $|g\rangle$ , and an optical excited state  $|F' = 3\rangle$  is regarded as  $|e\rangle$ . the ground-state  $|g\rangle$  is coupled via an optical transition of frequency  $\omega_c$  to the excited state  $|e\rangle$  with an atomic decay rate  $\gamma_\perp$ . Therefore, all atoms in the ground-state  $| -J \rangle$  and all excited state atoms  $| +J \rangle$  are as follows:

$$\begin{aligned} | -J \rangle &= \Pi_{i=1}^N |g\rangle_i = |g\rangle_1 |g\rangle_2 \cdots |g\rangle_N. \\ | +J \rangle &= \Pi_{i=1}^N |e\rangle_i = |e\rangle_1 |e\rangle_2 \cdots |e\rangle_N \end{aligned} \tag{4.3}$$

The  $| -J+1 \rangle$  state means  $N-1$  atoms in the ground-state and one atom in the excited state as follows:

$$\begin{aligned} | -J+1 \rangle &= \frac{1}{\sqrt{N}} |e\rangle_1 |g\rangle_2 |g\rangle_3 \dots |g\rangle_{N-1} |g\rangle_N \\ &+ \frac{1}{\sqrt{N}} |g\rangle_1 |e\rangle_2 |g\rangle_3 \dots |g\rangle_{N-1} |g\rangle_N \\ &+ \dots \\ &+ \frac{1}{\sqrt{N}} |g\rangle_1 |g\rangle_2 |g\rangle_3 \dots |g\rangle_{N-1} |e\rangle_N. \end{aligned} \quad (4.4)$$

Many two-level atoms and cavity photon states are described by the following Hamiltonian (76):

$$\hat{\mathcal{H}} = \frac{1}{2} \hbar \omega_{a0} \hat{J}_z + \hbar \omega_c \left( \hat{a}^\dagger \hat{a} + \frac{1}{2} \right) + \hbar g (\hat{a} \hat{J}_+ + \hat{a}^\dagger \hat{J}_-), \quad (4.5)$$

where  $\hat{J}_z = \sum_{i=1}^N \hat{\sigma}_{z,i}$ ,  $\hat{J}_+ = \sum_{i=1}^N \hat{\sigma}_{+,i}$ , and  $\hat{J}_- = \sum_{i=1}^N \hat{\sigma}_{-,i}$ . In the case of collective normal mode splitting, a cavity mode is closely resonant to the atomic optical transition instead of an off-resonant cavity probe. The initial state of the atoms and one photon is

$$|\Psi(t)\rangle = [C_{-J,1}(t)|-J\rangle|1\rangle + C_{-J+1,0}(t)|-J+1\rangle|0\rangle]. \quad (4.6)$$

Combining Eq. 4.5, 4.6, we obtain the following equations:

$$\begin{aligned} &i\hbar \dot{C}_{-J,1} |-J\rangle|1\rangle + i\hbar \dot{C}_{-J+1,0} |-J+1\rangle|0\rangle] \\ &= -\hbar g \sqrt{N} C_{-J+1,0} |-J\rangle|1\rangle - \hbar g \sqrt{N} C_{-J,1} |-J+1\rangle|0\rangle. \end{aligned} \quad (4.7)$$

The coupled equations for the coefficients  $C_{-J,1}$  and  $C_{-J+1,0}$  are

$$\frac{\partial C_{-J,1}}{\partial t} = ig \sqrt{N} C_{-J+1,0}, \quad (4.8)$$

$$\frac{\partial C_{-J+1,0}}{\partial t} = ig \sqrt{N} C_{-J,1}. \quad (4.9)$$

Therefore, the doublet in the spectrum is separated by  $\Delta = 2\sqrt{Ng^2} = 2\sqrt{2\kappa\gamma C}$ , and this can be more generalized as Eq. 4.10.

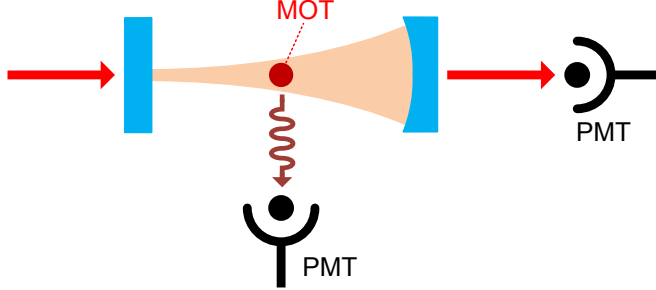


Figure 4.1: Schematic of an optical cavity with a MOT at the center of a hemispherical cavity mode (5); two PMTs are used for transmission and fluorescence detections.

The experimental apparatus is designed to demonstrate significant enhancement over the shot-noise limited sensitivity of a given atom number. Our goal is to achieve the best sensitivity toward the Heisenberg-limit. An untrapped atomic cloud expands depending on its temperature. Therefore, we need a comparable cavity mode volume to overlap the atomic cloud. We have large numbers of  $^{87}\text{Rb}$  magneto-optically trapped (MOT) atoms ( $\sim 2 \times 10^5$ ) at the center of the high-finesse hemispherical cavity mode as seen in Fig. 4.1. In our experiments, the atoms are located over nodes and anti-nodes of a standing wave cavity mode, and there is a spatially inhomogeneous atom-cavity coupling. Specifically, the longitudinal fast movement of the atoms in the cavity averages the inhomogeneous spatial coupling along the cavity axis, and we have  $g_{eff}^2 = \frac{g^2}{2}$  (77).

The theory for the vacuum-Rabi's splitting due to the atom-cavity coupling can be understood quantum mechanically in terms of the dressed states of an atom-cavity system. In the low excitation limit, the atom-cavity resonance is shifted from the bare atomic resonance  $\omega_0$ . In the limit of  $\kappa \ll \gamma, g$ , the doublet in the spectrum is separated by

$$\Delta = 2\sqrt{Ng^2 - \frac{\gamma^2}{4} + \frac{\delta^2}{4}}, \quad (4.10)$$

where the detuning  $\delta = \omega_0 - \omega_c$  is the detuning, where  $\omega_c$  is the bare cavity resonance. By comparing Eq. 4.1 and Eq. 4.10, we infer the effective  $\zeta$  of our system for large  $N$ , given  $\kappa$  and  $\gamma$ . This level-splitting is derived explicitly for a single excitation, which also applies to systems with a large photon number ( $n \gg 1$ ) under the condition of  $n \ll N$ . For a dressed bosonic system with a large number of excitations, only higher-order

transitions with energy separations identical to the vacuum splitting have nonzero matrix elements (76). Previous near-resonant level splitting experiments conducted in the small atom number regime ( $N < 600$ ) therefore required  $n \sim 1$  (22; 78; 79; 80). For higher amplitude excitation, the level splitting is reduced (78). Due to the large  $N$ , we are able to operate in much higher light intensity regimes. Recent work with large ensembles of atoms ( $\sim 10^6$ ) has observed the normal-mode splitting dispersively (81), which places different constraints on the photon number.

The normal-mode splitting is observed in the spectrum of the probe light transmitted through the cavity and the atomic fluorescence. A weak resonant probe beam is coupled into the cavity. We use two Hamamatsu R636-10 photo multiplier tubes (PMT) for the fluorescence images. One PMT is installed along the cavity axis to detect the transmitted probe light, and the other is aligned along the off-cavity axis to collect a fraction of the atomic fluorescence (Fig. 4.1). We load the MOT atoms before probing them with the cavity light. We varied the atomic loading time to control the atom number at the central region of the cavity. When the background vapor of the thermal atoms in the cavity region is reduced, we obtain rapid measurement cycle times for our measurements. A collimated atomic beam is generated in a two-dimensional (2D) MOT chamber and is loaded into a 3D MOT chamber at the center of a hemispherical cavity mode. During the experiment, the cavity lock is off, but it remains stable within the atom-cavity linewidth for tens of seconds. A NewFocus Vortex probe laser is scanned over 330MHz in 4ms from red to blue across the atomic resonance.

Fig. 4.2(a) shows the normal-mode splitting in a fluorescence spectrum detected from the atoms in the cavity mode during a single sweep of the probe beam frequency. We observe a sub-natural atomic linewidth, since we average the cavity and atomic linewidth in our large  $N$  regime. We measure the linewidth as

$$\text{linewidth (HWHM)} = 2\pi \cdot 1.74 \pm 0.04 \text{ MHz}, \quad (4.11)$$

with  $N \sim 1.3 \times 10^5$ . This is approximately  $\gamma$  (for  $\gamma \gg \kappa$ ) as we expected in the absence of any background broadening mechanisms.

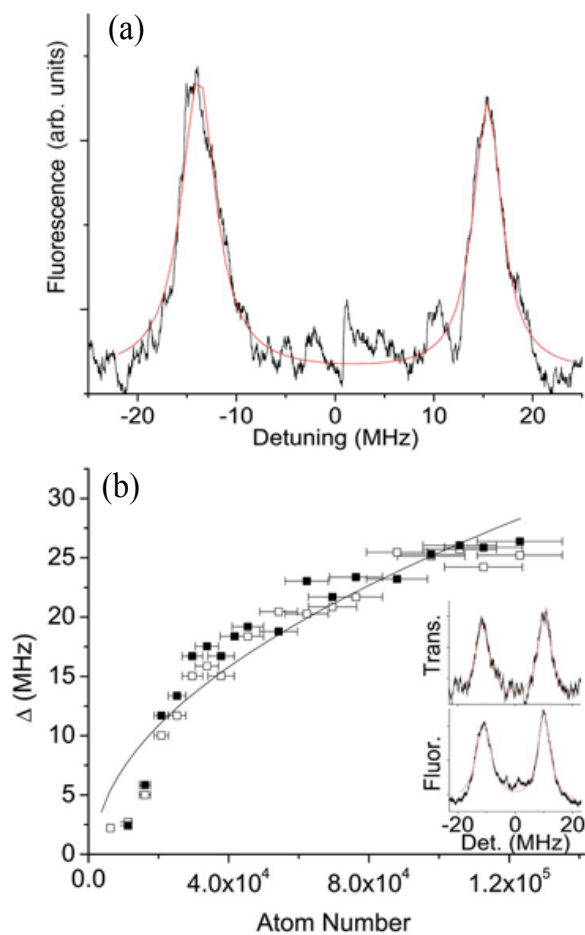


Figure 4.2: (a) Fluorescence spectrum vs. probe beam detuning. (b) Normal mode splitting vs. atom number (5).

We plot the normal-mode splitting observed both in fluorescence (empty squares) and transmission (filled squares) in Fig. 4.2(b). We average over eight frequency sweeps and measure  $\Delta$  for each  $N$  by fitting the data to a double Lorentzian to determine the peak separation. The number of atoms in the cavity mode is calibrated from the maximum observed level splitting using Eq. 4.10. The calibrated atom number is consistent with the fluorescence measurements of the MOT atom number. For shorter loading times,  $N$  is extrapolated from a  $1/e$  MOT loading decay time, which is  $\sim 250$  ms. The measured data follows a power law

$$\Delta = (2.11 \pm 0.34) \left( Ng^2 - \frac{\gamma^2}{4} \right)^{0.51 \pm 0.04}. \quad (4.12)$$

This agrees with Eq. 4.10. The horizontal error bars originate from a 15% shot-to-shot atom number fluctuation. The fit to the data is best for a large atom number ( $N \sim 1.7 \times 10^4$ ) in the low-intensity limit ( $n \ll N$ ). The intensity of the transmitted light related to the intracavity photon number drops suddenly from 450 pW to 23.5 pW for between  $1.1 \times 10^4$  and  $1.6 \times 10^4$  atoms. In this very low  $N$  regime, the atomic transition is partially saturated, which reduces the mode splitting (78; 82).

By optimizing our MOT loading sequence for the total atom number in the cavity, we maximize the observed mode splitting at  $\Delta = 2\pi \cdot 32.1$  MHz ( $N \sim 2 \times 10^5$ ) corresponding to  $C = 1.2 \times 10^4$  and  $1/\zeta \sim 12$ . This  $\zeta$  coupled with a large  $N$  offers the potential for achieving the absolute phase resolution ( $\Delta\Phi_{SSS}$ ). The sensitivity of the atomic sensors is improved compared to the best Cs fountain clocks that exist, which operate at the projection noise limit for up to  $10^7$  atoms (83). Since our system is not in the number density limiting regime, we expect to enhance the sensitivity of our sensor by increasing the atom number.

The normal-mode splitting is demonstrated when the cavity mode is closely resonant to the atomic transition. Therefore, as the detuning changes relative to the bare cavity transition, the degree of separation varies.

With a fixed atom number  $N \sim 1.3 \times 10^5$ , there is an excellent correlation between the expected splitting and the splitting measurement in the regime where the cavity is red-detuned ( $\delta > 0$ ) from the atomic resonance in Fig. 4.3.

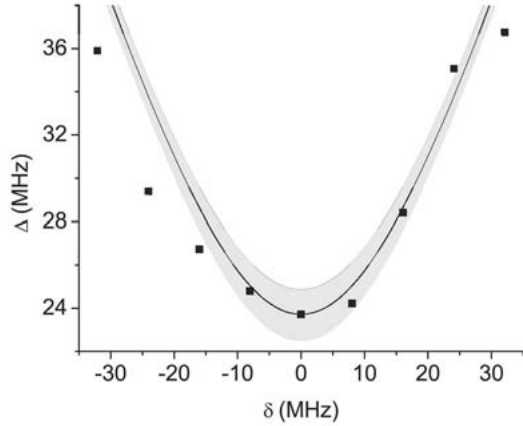


Figure 4.3: Normal mode splitting vs. detuning  $\delta$  ( $= \omega_0 - \omega_c$ ), where  $\omega_0$  is the bare atomic resonance, and  $\omega_c$  is the bare cavity resonance (5).

In Chapter 4.1, a large collective cooperativity ( $C = 1.2 \times 10^4$  with  $N \sim 2 \times 10^5$ ) is achieved in the high-finesse single- $\lambda$  cavity. The collective cooperativity is measured by the collective normal-mode splitting of the many-atom-cavity dressed state system via the atomic fluorescence or the transmission spectra. Based on the large collective cooperativity, we are able to realize an absolute phase sensitivity of atomic sensors that is better than that of the state-of-the-art atomic sensors operating near a quantum projection noise.

## 4.2 Anti-Spin-Squeezing

In our cQED system, the cavity-aided nondemolition measurement with a far-detuned and weak cavity probe (i.e., a probe that has a low spontaneous emission rate) has been used for generating collective pseudospin-squeezing of atomic clock states. The cavity probe's detuning is  $\sim 1.5$  GHz from the  $|F = 2\rangle$  to  $|F' = 3\rangle$  transition. In the optical Bloch sphere, a geometrical representation of two level quantum system, an excited state  $|2\rangle$  and a ground state  $|1\rangle$  are  $|F = 2, m_f = 0\rangle$  and  $|F = 1, m_f = 0\rangle$  respectively. As an initial state preparation, a  $\frac{\pi}{2}$  pulse turns all the atoms in the ground-state  $|1\rangle$  into the coherent spin state. The far-off-resonance cavity probe experiences the atom's index of refraction, and the atom-induced cavity shift provides information about the number of atoms coupled to the cavity

mode. Depending on the atomic state and the detuning, the cavity probe experiences different indices of refraction. The photodetection process of the cavity photons interacting with atoms creates conditional spin-squeezing. The detection of the probe's phase induces conditional QND measurement of the atoms, which projects the atomic states,  $\hat{J}_z$ , onto the value corresponding to the observed phase shift. The sub-shot noise limited atom measurement is available by means of the spin-squeezing process, but the fractional uncertainty of the probe phase is limited by the photon shot noise of the photodetector.

In the far-off-resonant regime, if we assume that all atoms have homogeneous coupling to the cavity mode, from Eq. 2.7, the Hamiltonian of spin-squeezing for  $N$  atoms is

$$\begin{aligned}\hat{\mathcal{H}}_N = & -(\Delta - \delta_0)\hat{a}^\dagger\hat{a} + 0 \cdot \hat{J}_z + i\mathcal{E}(\hat{a}^\dagger - \hat{a}) \\ & + g^2\hat{a}^\dagger\hat{a}\hat{J}_z\left(\frac{1}{\Delta_p} - \frac{1}{\Delta_p - \omega_a}\right),\end{aligned}\quad (4.13)$$

where  $\hat{J}_z = \sum_{i=1}^N \hat{\sigma}_{z,i} = \sum_{i=1}^N (|2\rangle\langle 2|_i - |1\rangle\langle 1|_i)$  is a collective atomic operator,  $\delta_0 = \left(\frac{Ng^2}{\Delta_p} + \frac{Ng^2}{\Delta_p - \omega_a}\right)$  is the offset of atom-induced cavity resonance shift,  $N = \sum_{i=1}^N (|2\rangle\langle 2|_i + |1\rangle\langle 1|_i) = N\mathbb{I}$  is the atom number operator,  $g$  is the atom-cavity coupling strength, and  $\Delta_p$  and  $\Delta_p - \omega_a$  are the probe beam's detuning from  $|2\rangle$  and  $|1\rangle$  respectively. The atom-cavity interaction Hamiltonian is  $\hat{\mathcal{H}}_{int} = g^2\hat{a}^\dagger\hat{a}\hat{J}_z\left(\frac{1}{\Delta_p} - \frac{1}{\Delta_p - \omega_a}\right) = n\Omega\hat{J}_z$ , where the photon number operator is  $n = \hat{a}^\dagger\hat{a}$ , and  $\Omega = g^2/\Delta_p - g^2/(\Delta_p - \omega_a)$ . The collective atom-cavity interaction between two coherent states leads to the phase shift in the probe field  $\Delta\phi = \hat{J}_z\Omega t$  for the interaction time  $t$ , while the collective atomic pseudospin vector precesses in the equatorial plane of the Bloch sphere at a rate proportional to the photon number.

The collective pseudospin vector is coupled to the coherent state of the intracavity light. The coherent state of the light,  $|\Psi_{ph}\rangle = \sum_{n=0}^{\infty} e^{-\frac{|\alpha|^2}{2}} \frac{\alpha^n}{\sqrt{n!}} |n\rangle$ , is the ensemble state of a Fock state with a Poisson distribution. The initial coherent spin state,  $|\Psi_{at}\rangle = \sum_{k=0}^{2J} \frac{1}{2^J} \binom{2J}{k}^{\frac{1}{2}} |J, J_z = J - k\rangle$ , coupled to the different eigenstates of the light has different rotation rates, which results in the fluctuation of the collective spin vector to the equatorial line of the Bloch sphere. The uncertainties of collective atomic operators can be analytically derived with the coherent spin state  $|\Psi_{at}\rangle$  and the coherent state of intracavity light  $|\Psi_{ph}\rangle$ . In a cavity, the collective atom-cavity interaction between atoms and a cavity probe induces the unitary evolution of the atom states and the photon states.

The time-dependent interaction Hamiltonian  $\hat{\mathcal{H}}_{int}(t)$  for a time interval yields the unitary evolution,  $\hat{U}_t \hat{\rho}_{sys} \hat{U}_t^\dagger$ , where  $\hat{U}_t \propto \exp\left[-\frac{i}{\hbar} \int_0^t dt' \hat{\mathcal{H}}_{int}(t')\right] = \exp\left[-i \frac{N_{at} g^2}{\Delta_p} \int_0^t dt' n_{ph}(t')\right]$ . We assume that a coherent state of cavity photons interacts with atoms during a time interval, and the photon states interacted with atoms can be taken away from the system by measurement process. A projective measurement on the photon state, whose statistics are specified by some set of partial projectors  $\Pi_i^{ph} \otimes \mathbb{I}^{at}$ , will lead to  $\text{Pr}(i) = \text{Tr}[(\Pi_i^{ph} \otimes \mathbb{I}^{at}) \{\hat{U}_t |\Psi_{at}\rangle \langle \Psi_{at}| \otimes |\Psi_{ph}\rangle \langle \Psi_{ph}| \hat{U}_t^\dagger\} (\Pi_i^{ph} \otimes \mathbb{I}^{at})]$ . The post-measurement state of the system is  $|\Psi_S\rangle_{post} = (\Pi_i^{ph} \otimes \mathbb{I}^{at}) \{\hat{U}_t |\Psi_{at}\rangle \langle \Psi_{at}| \otimes |\Psi_{ph}\rangle \langle \Psi_{ph}| \hat{U}_t^\dagger\} (\Pi_i^{ph} \otimes \mathbb{I}^{at}) / \sqrt{\text{Pr}(i)}$ . The post-measurement density matrix about the atoms is  $\hat{\rho}_{at|post,i} = (\Pi_i^{ph} \otimes \mathbb{I}^{at}) \{\hat{U}_t |\Psi_{at}\rangle \langle \Psi_{at}| \otimes |\Psi_{ph}\rangle \langle \Psi_{ph}| \hat{U}_t^\dagger\} (\Pi_i^{ph} \otimes \mathbb{I}^{at}) / \text{Pr}(i)$ , where  $\sum_i (\Pi_i^{ph} \otimes \mathbb{I}^{at}) = (\sum_i \Pi_i^{ph}) \otimes \mathbb{I}^{at} = \mathbb{I}_{ph} \otimes \mathbb{I}^{at} = \mathbb{I}^{ph \otimes at}$ . Thus,  $\Delta \hat{J}_k^2$  ( $k = x, y, z$ ) can be calculated as follows:  $\Delta \hat{J}_k^2 = \langle \hat{J}_k^2 \rangle - \langle \hat{J}_k \rangle^2 = \text{Tr}[\hat{\rho} \hat{J}_k^2] - (\text{Tr}[\hat{\rho} \hat{J}_k])^2$ .

Since the Hamiltonian entangles the collective atomic pseudospin  $\hat{J}_z$  with the probe field phase, the measurement of the probe's phase projects the atomic state onto a stochastically determined state of  $\hat{J}_z$  with the corresponding uncertainty. For  $n\Omega^2 t^2 \ll 1$ , the uncertainty is conditioned on the outcome of the phase measurement, and the uncertainty is  $\Delta \hat{J}_z^2 = \frac{N}{4} \frac{1}{1 + \frac{1}{2} N n \Omega^2 t^2}$ , rather than the standard quantum limit of  $\Delta \hat{J}_z^2 = \frac{N}{4}$ . For interaction times greater than the cavity photon lifetime,  $\tau_c = 1/\kappa$ , the above picture is modified by the leakage of photons from the cavity. Effectively, the interaction time can be broken down into intervals of length  $\tau_c$ , where the probe state is measured, and the resulting atomic state interacts with a new photon state. The squeezing will then be given by  $\Delta \hat{J}_z^2 = \frac{N}{4} \frac{1}{1 + \frac{1}{\sqrt{2}} N n \Omega^2 t \tau_c} \simeq \frac{N}{4} \frac{1}{1 + \frac{1}{\sqrt{2}} N \Omega^2 \tau_c \int ndt}$ , where  $n$  now denotes the time-averaged intracavity photon number. In the optical Bloch sphere, the corresponding uncertainty ellipse of the collective pseudospin vector rotates with the atomic state. The collective pseudospin vector remains polarized along  $x$ . The anti-spin-squeezing is then  $\Delta \hat{J}_y^2 = \frac{N}{4} \left(1 + \frac{1}{\sqrt{2}} N n \Omega^2 t \tau_c\right) \simeq \frac{N}{4} \left(1 + \frac{1}{\sqrt{2}} N \Omega^2 \tau_c \int ndt\right)$ . The conditional collective pseudospin-squeezing occurs only when we detect the atomic states via the QND probe light. The QND interaction process causes the unitary evolution of the atomic state. The conditional detection induces the conditional spin-squeezed state of the atoms. A more generalized model was treated in Chapter 2, and for a small number of atoms, we can simulate the conditional spin-squeezing conditioned on the heterodyne photodetection process.

Atomic spontaneous emission into free space reduces the correlation between the measured probe phase, and the collective pseudospin of the atoms used for the clock. If the spontaneous emission rate is known, the average phase shift due to the atoms that have scattered can be subtracted out. The stochastic fluctuation in the phase shift is not considered in our simplified calculation, but the fluctuation will add noise and reduce the degree of the conditional squeezing.

We used a single- $\lambda$  cavity chamber with  $(g, \kappa, \gamma) = 2\pi \cdot (53, 3.7, 3030)$  kHz (HWHM); all the cavity parameters are shown in Table 3.1. At the central region of the cavity, the released MOT atoms are further cooled by the optical molasses stage. The atoms prepared in a superposition of the clock states fall through the cavity and interact with a QND probe light. The probe beam senses the collective pseudospin state of the laser-cooled  $^{87}\text{Rb}$  atomic cloud in a magneto-optical trap (MOT).

The modulation scheme and cavity lock scheme of the single- $\lambda$  cavity are described in Chapter 3. The probe sideband beam is used to monitor the collective pseudospin of the atoms in the cavity via the phase shift. The variation in the atomic index of the refraction during the atom-photon interaction produces the phase shift on the probe beam. The phase shift is measured using a similar Pound-Drever-Hall scheme for the lock, with the error signal resulting in the phase shift. In the experiments described here, the probe is tuned at  $\sim 1.5$  GHz to the red of the  $5^2S_{\frac{1}{2}}, F = 2 \rightarrow 5^2P_{\frac{3}{2}}, F' = 3$  atomic transition with an input power of  $3 \sim 6$  nW, while the locking beam, is tuned further to the red at 18.06 GHz has an input power of 15 nW. The cavity-enhanced non-demolition measurement is designed for both spin-squeezing and atom number measurement. The slope of the dispersive signal is used to measure the atom number: A properly tuned probe frequency reads the atom number depending on the slope. The fluctuation between two states of  $|F = 1, m_f = 0\rangle$  and  $|F = 2, m_f = 0\rangle$  is used to quantify the standard deviation of the atoms.

The atomic cloud has a  $\frac{1}{e}$  radius of  $390\,\mu\text{m}$ . The atoms fall through the center of the cavity mode at  $2.9\,\text{cm/s}$ , while the atomic cloud expands at  $3.7\,\text{cm/s}$ . The cavity-enhanced measurement time for the atoms is hence limited to several ms. The thermal velocity of the atoms causes them to travel  $390\,\text{nm}$  between adjacent nodes of the cavity-standing wave in  $10\,\mu\text{s}$ . Measurements longer than  $10\,\mu\text{s}$  average over the longitudinal inhomogeneities in the ac Stark shift, but there exists a residual broadening due to the

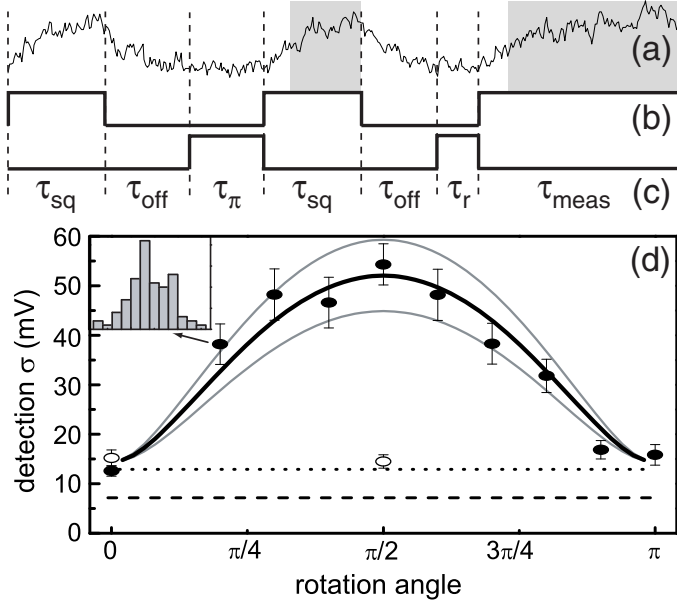


Figure 4.4: (a) Measured data. (b) Two spin-squeezing pulses and one final destructive probe pulse. (c) Microwave pulses of spin echo and final rotation. (d) Anti-spin squeezing vs. microwave rotation angle (4).

width of the thermal distribution. In the transverse direction, the ac Stark shift varies by a few percent in  $100 \mu\text{s}$  of the atomic motion, which also contributes to the inhomogeneous broadening. In addition, there exists a residual light shift from the locking beam, which results in additional inhomogeneous dephasing because the locking beam is always on during the measurement process. Experimentally, the interaction time  $t$  of squeezing pulses is also limited by the scattering rate at the detuning and power of a cavity probe because more scattering means more decoherence among coherent atoms.

Using the three-pulse sequence with a spin echo pulse illustrated in Fig. 4.4(a)-(c), the spin-squeezed state is generated and measured. To measure the atom number, there are two nondestructive ( $60 \mu\text{s} \times 2$ ) spin-squeezing pulses and one final destructive probe pulse ( $> 500 \mu\text{s}$ ). Between the two spin-squeezing pulses, the spin echo pulse is driven, which suppresses the inhomogeneous broadening effect. The probe light is turned on for a time  $\tau_{sq}$ . After that, it is turned off for a time  $\tau_{off}$ . After a possible final microwave rotation time  $\tau_r$ , the probe light measures the atomic state continuously for a time  $\tau_{meas}$ .

To quantify the conditional projection noise in our measurement, we calculate the difference between the cavity shift observed during the long measurement time and that observed during the second squeezing pulse. In practice, we tune the probe laser to be resonant with the cavity in the presence of the atoms, and simply average the Pound-Drever-Hall error signal that results from the heterodyne detection of the cavity shift at the probe frequency. The projection noise can then be extracted from the shot-to-shot fluctuations in the difference in the averages for the two periods.

Since the spot size of the cavity mode is comparable to the size of the atomic cloud, the atom-cavity coupling varies significantly in the transverse direction and is not averaged during the measurement process. For an atom cloud with a radius  $r_a$  and a cavity spot size  $r_c$ , the average atom-cavity coupling is less than the maximal on-axis value by a factor of  $(\frac{r_a}{r_c})^2 + 1$ . The variable related to the probe phase measurement is not  $\Omega \hat{J}_z = \Omega \sum_{i=1}^N \hat{\sigma}_{z,i}$  but  $\sum_{i=1}^N \Omega_i \hat{\sigma}_{z,i}$ , where  $\Omega_i$  is spatially-varying according to each atom's position. The projection noise of this variable is given by  $\Delta(\Omega \hat{J}_z) = \Omega \hat{J}_z \frac{\left\{(\frac{r_a}{r_c})^2 + 1\right\}^2}{2\left(\frac{r_a}{r_c}\right)^2 + 1}$ , which is the proper standard quantum limit to use for the evaluation of the spin-squeezing in our measurement. Because the dimension of the cavity waist limits an overlap volume between the atomic cloud and the probe beam, and the cavity coupling  $g_i(\vec{r})$  varies depending on the position of each atom, the effective atom number ( $N_{eff}$ ) and the actual atom number ( $N$ ) are different. At the atomic temperature of  $14.5 \mu\text{K}$ , the radius of the atomic cloud,  $r_a$ , is  $270 \mu\text{m}$  (after 3 ms), and the radius of the cavity mode,  $r_c$ , is  $310 \mu\text{m}$ .

In our experiment, the variance due to the atom shot noise is not exactly linearly proportional to the atom number. However, the atom shot noise data of the anti-spin-squeezing increases linearly with the atom number. This linear proportionality means that the spin-squeezing produced by our protocol cannot be measured for various reasons, such as the inhomogeneous cavity coupling, the inhomogeneous broadening, and technical noise.

The anti-spin-squeezing data, the variance of the in-plane component of the atomic pseudospin as a function of the atom number and probe intensity, is obtained by rotating the spin state after the two squeezing pulses (Fig. 4.5); the degree of anti-spin-squeezing

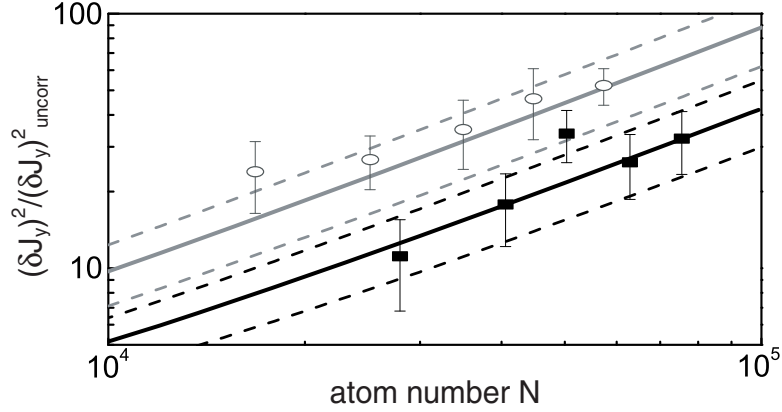


Figure 4.5: Anti-spin-squeezing of the variance of the in-plane atomic pseudospin (4); the black squares and white circles correspond to probe input powers of  $\approx 1.2 \text{ nW}$  and  $\approx 2.5 \text{ nW}$ , respectively.

$(\Delta \hat{J}_y)^2 / (\Delta \hat{J}_y)^2_{uncorr}$  is linearly proportional with the atom number and more coherently scattered photons, as we expected. To obtain the anti-spin-squeezing state, we rotate the uncertainty ellipse around its center using an additional  $\frac{\pi}{2}$  microwave pulse. The microwave pulse is driven between squeezing pulses and the final destructive measurement pulse. As we alter the duration of the final microwave pulse or the phase of the final microwave pulse with a fixed duration of  $\tau_{\frac{\pi}{2}}$ , we read out the orientation of the uncertainty ellipse from the measured atomic shift, a process that is similar to the Rabi oscillation with respect to the pulse duration of the microwave. After the two squeezing pulses generate the number-squeezed state, the  $\frac{\pi}{2}$  microwave pulse with the translated rotation axis rotates the number-squeezed state to the phase-squeezed state. The  $\frac{\pi}{2}$  rotation allows us to measure the anti-spin-squeezed state. The degree of atomic measurement noise is proportional to the degree of the rotation within a  $\frac{\pi}{2}$  rotation (see a Fig. 4.4(d)).

We can produce oscillation of an atomic population by scanning the collective pseudospin rotation axis in the equatorial plane of the Bloch sphere. After all sequences, the presence of the QND probe light (two squeezing pulses) reduces the final atomic contrast obtained in the oscillation to about 73% of the full contrast. The full atomic contrast is measured without the squeezing pulse immediately after the initial state superposition.

The inhomogeneous dephasing differs from the collective anti-spin-squeezing despite the fact that the dephasing is superficially similar to the anti-spin-squeezing in our experiment. We confirmed that the anti-spin-squeezing is different from the inhomogeneous light dephasing: A short squeezing pulse resulting in the same atomic contrast as two long squeezing pulses with an echo cannot generate anti-spin squeezing. The spin echo pulse compensates for the most inhomogeneous dephasing, but it cannot overcome the anti-spin-squeezing. The anti-spin-squeezing of the phase quadrature is produced via the QND interaction between the atoms and the QND probe light. If the QND interaction time is shorter, the degree of the spin-squeezing and of the anti-spin-squeezing become smaller. In our experiment, a single  $20\mu s$  squeezing probe pulse without a spin echo pulse produces the same amount of inhomogeneous dephasing as is produced by two sequential  $60\mu s$  squeezing probe pulses and a spin echo pulse. However, the  $20\mu s$  pulse produces much less anti-spin-squeezing rather than two  $60\mu s$  pulses and a spin echo pulse (see Fig. 4.4(d)).

The quantum non-demolition measurement of atoms in a high-finesse single- $\lambda$  cavity creates entanglement between the cavity probe field and the collective atomic pseudospin. The photodetection process of the cavity photons interacting with atoms generates the spin-squeezed state conditioned on the photodetection. Although we only observed a few dB of spin-squeezing due to reduced atomic coherence by spatially inhomogeneous atom-cavity coupling and residual light shifts from a cavity locking sideband, the 13dB anti-spin-squeezing promises that spin-squeezing can be generated in our system. We have analyzed the quadrature anti-spin-squeezing produced by the entanglement process to demonstrate that our protocol produces conditional spin-squeezing in the atomic ensemble.

# **Chapter 5**

## **Cavity QED System with Identically Coupled Atoms**

We demonstrated a many-atom-cavity system with a high-finesse dual-wavelength standing wave cavity in which all atoms are identically coupled to the desired cavity mode. Atoms are optically trapped in the one-dimensional lattice formed by the intense field of a 1560nm cavity mode, and register at the maxima of the 780nm cavity probe mode profile in the central region of the cavity. We investigated the characteristics of the system, such as atom registration, trap lifetimes, and atomic coherence times.

### **5.1 Introduction**

The field of cavity quantum electrodynamics (cQED) (20) studies the interaction between atoms and a cavity mode, in a regime where quantum properties of both participants are prominent. The confinement of light can increase the coherent atom-photon interaction strengths drastically such that an individual photon occupying a cavity mode that is near-resonant with an atomic transition can entirely change the mode structure of the cavity (84; 85). Initial experiments in the field have used laser cooled atoms freely falling through cavity modes, but various methods of trapping the atoms within the cavity modes for achieving longer and more controllable interactions were rapidly developed (86). For instance, cavity modes with frequencies that are far-off resonance from an atomic transition

are now used form state-insensitive optical dipole traps for the atoms within the cavity modes.

In addition to the experiments pursuing cQED with individual atoms, there has been growing interest in the last decade for studying the collective interaction of large ensembles of atoms with cavity fields. Specific interests include topics such as cavity-aided entanglement generation (spin-squeezing) for quantum enhanced metrology (87; 88), optomechanics with atoms for studying the coupling of collective motional degree of freedom to a cavity field (89), cavity-enhanced atomic quantum memories for quantum information processing (90), or ultra-narrow-linewidth lasers using narrow-transition ultra-cold atoms as the gain medium for metrological purposes (91). Central to many such conceivable systems is the issue of the variation in the coupling strength of the participating atoms to the cavity field, which degrades the coherence of the interactions, complicates the dynamics and the analysis of the basic physics, and sometimes completely disables the experiments.

Limiting our attention to Fabry-Perot type cavities, in which the modes are standing waves, identical coupling of the atoms to the relevant cavity mode (the probe mode) can be achieved by tightly trapping the atoms with a spatial period that is commensurate with the wavelength of the probe mode. Thus far, experimentally realized cavity-mode optical dipole traps have been incommensurate in a period with the relevant probe modes, resulting in non-identical atom-probe coupling and often requiring the definition of effective averaged coupling constants. We note that an alternative solution to the problem of identical coupling has recently been demonstrated where a trapped Bose-Einstein condensate (BEC) is made to interact with a cavity mode. In this case, identical atom-probe interaction is guaranteed irrespective of spatial variations in the atom-probe coupling as all the atoms occupy a single mode of the trap (92; 93). Nevertheless, from the perspective of precision measurement applications, one should keep in mind that BEC can be problematic due to uncontrollable energy shifts brought about by atomic collisions in the high density ensemble. In this paper, we present the realization and some performance characteristics of a many-atom cQED system in which atoms can be trapped at the anti-nodes of the probe mode with the aid of an optical dipole trap formed by a cavity mode half the frequency of the probe mode, allowing identical coupling strengths.

We investigated a dual-wavelength near-confocal cavity resonant at both 780nm and 1560nm. The former wavelength corresponds to the D<sub>2</sub> transition of atomic <sup>87</sup>Rb and is used for the probe mode, and the latter wavelength is used to form a far detuned one-dimensional (1D) optical lattice to trap the atoms. At the central region of the cavity, these commensurate probe and trapping wavelengths allow an in-phase registration of the atoms where they are localized at the maxima of the probe mode profile, as well as an out-of-phase registration in which case of a 1560nm trap comes with some disadvantage too as this value is close to the 5P – 4D transitions of <sup>87</sup>Rb (Fig. 5.1 (b)), causing strong redshifts on the 5P levels, significantly interfering with the operation of the magneto optical trap (MOT) and the optical molasses in the presence of a deep trap.

In a typical experiment, the atoms that are trapped in the MOT are first further cooled by switching to a far-detuned MOT (12 $\gamma$  red detuned) for  $\sim 25$  ms followed by a magnetic field-free polarization gradient cooling stage (54 $\gamma$  red detuned) for  $\sim 7$  ms, down to  $\sim 15 \mu\text{K}$ . These stages happen in the presence of a weak optical lattice, as a small amount of 1560nm light is necessary to keep the lasers locked to the cavity. Towards the end of polarization gradient cooling, we turn up the optical lattice power adiabatically by changing the 1560nm sideband power by a factor of as much as 100, and typically load  $10^4 \sim 10^5$  atoms distributed over about a couple thousand lattices sites, ready for experiments. With the onset of the full lattice ( $\sim 40\text{W}$  circulating optical power) we observe, what we interpret as, a differential drift in the effective cavity lengths for the 780nm and 1560nm light due to heating of the mirror coatings. For an identical drift in the two cavity lengths, the probe light should follow the cavity resonance (assuming exactly doubled frequency relationship). Nevertheless, this change in the cavity lengths comes to an equilibrium after a couple hundred milliseconds.

Our dual- $\lambda$  cavity has a 780nm cavity probe and a 1560nm cavity lattice which are able to localize atoms periodically in-phase with the cavity probe and allow us to register all the trapped atoms in each lattice site homogeneously at the central region of the cavity (Fig. 5.1(a)); all the cavity parameters, including  $(g_{780}, \kappa_{780}, \kappa_{1560}, \gamma) = 2\pi \cdot (142, 3.99, 5.98, 3030)$  kHz (HWHM) are shown in Table 3.1. The uniqueness of the equivalent atom registration in the cavity, assuming cold-enough atoms, allows us to extend

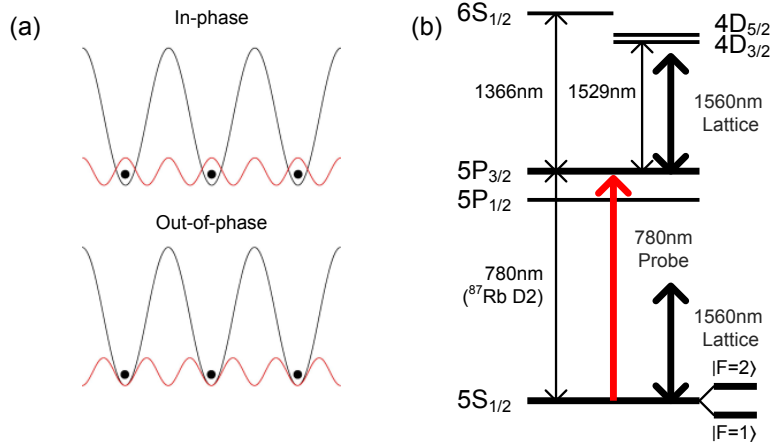


Figure 5.1: (a) In-phase and out-of-phase atom registration at the cavity center. Black curves: lattice potential due to the 1560 nm light, red-curves: 780 nm probe light intensity. (b) Energy level diagram of  $^{87}\text{Rb}$  atoms.

the cQED research to high degrees of spin-squeezed state generation and to macroscopic self-trapping of two hyperfine levels by collective atom-cavity interaction.

In this chapter, the dual- $\lambda$  cavity lock scheme of one master laser are used as described in Chapter 3 (Fig. 3.13). We stabilize a master 1560 nm laser to a high finesse reference cavity ( $\sim 5$  MHz bandwidth) and have a slave injection lock, in order to generate a low-noise light. The low noise 1560 nm light is amplified by an EDFA amplifier. The one path of the amplified light is locked to the science cavity via the PDH method ( $\sim 100$  kHz lock bandwidth) using the acousto-optic modulator (AOM) situated before the 1560 nm slave diode laser and the reference cavity PZT as the fast and slow frequency feedback elements respectively. The other path of the amplified light is frequency-doubled by a PPLN, and the frequency-doubled cavity probe (780 nm) follows the 1560 nm master laser's cavity lock. The scheme of one master laser lengthens the coherence time of trapped atoms because a cavity lock sideband that results in residual light shifts is unnecessary.

In addition, we measured the cavity FSR of two cavity mode (1560 nm and 780 nm). There was a slight difference between two cavity modes because of the different penetration depths. For simplicity, we assume for the rest of the discussion that the FSR of the cavities corresponding to the 780 nm and 1560 nm modes are identical. This assumption should not

change the discussion concerning the in-phase and out-of-phase registration as long as the two cavity mirrors are identical, so that the penetration depths are symmetric.

## 5.2 Identical Atom-Cavity Coupling

The  $\pi$ -polarized probe mode interacts dispersively with the atoms inside of the cavity by coupling the  $|F = 2\rangle$  ground states to the  $5P_{3/2}$  excited states with an effective frequency detuning of  $\Delta$  which we typically choose to be on the order of  $1\text{GHz} \gg \gamma$ . The resulting refractive index caused by the  $|F = 2\rangle$  atoms shifts the resonance frequency of the probe mode. The effects of absorption are minor. The amount of probe mode shifts incurred by an atom located at position  $\mathbf{r}_i$  can be given in terms of the position-dependent atom-cavity coupling constant  $g_i \equiv g(\mathbf{r}_i)$ , as  $\delta v_i = g_i^2 / \Delta$ . Note that the atoms in  $|F = 1\rangle$  states also give rise to shifts, but by an amount that is an order of magnitude smaller due to the larger detuning, so we will ignore their contribution from our discussion for simplicity. The shift incurred by an ensemble of atoms can be found simply by summing over all participating atoms  $\delta v = \sum_i \delta v_i$ . We utilize this cavity shift to show that we can trap the atoms entirely either at the nodes or anti-nodes of the probe mode, corresponding to out-of-phase and in-phase registration respectively.

For an exact frequency-doubling relationship between the lattice and the probe mode, one would expect to achieve the out-of-phase registration everywhere inside the cavity. However, shifting the frequency of the probe mode by a number  $m$  of FSRs splits the cavity into  $2m + 1$  alternating regions of out-of-phase and in-phase registrations. As we are coupling the frequency shifted sidebands into the cavity modes, we have the ability to hop the probe mode by a few FSRs, with the frequency relation between the probe and the lattice modes given by  $v_p = 2v_t + m \cdot \Delta v_{\text{fsr}}$  (Fig. 3.13 (b)). Around the cavity center (well within the Rayleigh range), the atom-cavity coupling constant's square and the lattice intensity distribution that is negatively proportional to the trapping potential are given by (assuming for simplicity that the lattice occupies an even cavity mode)

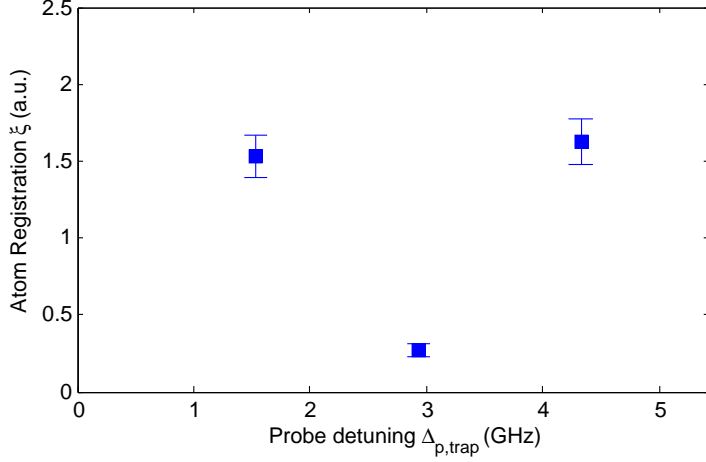


Figure 5.2: Atom registration  $\xi$  vs. cavity probe detuning  $\Delta_{p,trap}$  ( $^{87}\text{Rb}$  D2 transition from  $F = 2$  to  $F' = 3$ ). The two in-phase probes and one out-of-phase probe show different atom registrations  $\xi$ . The ratio between in-phase and out-of-phase registration  $\frac{\xi_{in ph}}{\xi_{out ph}}$  is 6.2 (0.2).

$$g^2(r) = g_0^2 \exp[-2(x^2 + y^2)/\omega_{o,p}^2] \sin^2\left(\frac{2\pi v_p}{c}z + \frac{m\pi}{2}\right), \quad (5.1)$$

$$I_t(r) = I_0 \exp[-2(x^2 + y^2)/\omega_{0,t}^2] \cos^2\left(\frac{2\pi v_t}{c}z\right), \quad (5.2)$$

where  $z$  is the coordinate along the cavity axis with  $z = 0$  corresponding to the cavity center,  $x$  and  $y$  are the coordinates transverse to the cavity axis,  $\omega_{o,p}$  and  $\omega_{0,t}$  are the probe and lattice mode waists respectively, and  $c$  is the speed of light. For probe modes with  $m$  odd and even respectively, one obtains in-phase and out-of-phase registrations around the cavity center as depicted in Fig. 5.2.

The spatially identical atom-cavity coupling is the unique property of the cavity. We measured atom-cavity couplings of trapped atoms and MOT atoms using a cavity probe. A measured cavity shift of trapped atoms  $\delta f_{trap}$  corresponds to  $N_{trap}$  optically trapped atoms with a  $\Delta_{p,trap}$  red-detuned probe, and a measured cavity shift of MOT atoms  $\delta f_{mot}$  corresponds to  $N_{mot}$  magneto-optically trapped (MOT) atoms (without a lattice trap) with a  $\Delta_{p,mot}$  red-detuned probe, where  $\Delta_{p,trap} = \Delta_{p,mot} + \delta_{ac,trap}$ . In a lattice trap, the probe detuning  $\Delta_{p,trap}$  has to include the lattice-dependent ac Stark

shift  $\delta_{ac,trap} (< 0)$  of  $5P_{3/2}$  to  $4D_{3/2,5/2}$  transitions (Fig. 5.1 (b)). Assuming a constant atomic loading rate to the lattice trap,  $\frac{\delta f_{trap}}{\delta f_{mot}}$  can normalize atom number variation. The measured data  $\frac{\delta f_{trap}}{\delta f_{mot}}$  is  $\frac{\sum_{i=1}^{N_{trap}} g(\mathbf{r}_i)^2 / \Delta_{p,trap}}{\sum_{j=1}^{N_{mot}} g(\mathbf{r}_j)^2 / \Delta_{p,mot}} = \frac{\Delta_{p,mot}}{\Delta_{p,trap}} \xi$ , where the atom registration ratio  $\xi = \sum_{i=1}^{N_{trap}} g(\mathbf{r}_i)^2 / \sum_{j=1}^{N_{mot}} g(\mathbf{r}_j)^2$ . As shown in Fig. 5.2, an in-phase cavity probe with a detuning  $\Delta_{p,0} (= 1.53 \text{ GHz})$  registers the trapped atoms in-phase for  $\Delta_{p,0} + 2 \cdot \Delta v_{\text{fsr}} (= 4.33 \text{ GHz})$  or out-of-phase for  $\Delta_{p,0} + 1 \cdot \Delta v_{\text{fsr}} (= 2.93 \text{ GHz})$  at the cavity center.

The ratio of in-phase to out-of-phase atom registrations,  $\frac{\xi_{in ph.}}{\xi_{out ph.}}$ , is 6.2 (0.2). At a given lattice depth, the ratio  $\frac{\xi_{in ph.}}{\xi_{out ph.}}$  between in-phase and out-of-phase atom registrations allows us to estimate the temperature of the trapped atoms because colder atoms are localized within the smaller volume in the same trap and have a better atom-cavity coupling than hotter atoms have. For a given optical depth, the size of atomic clouds can be approximated with the mean characteristic lengths of the  $n$ -th trap excited state based on the trapped atom temperature. Assuming that the density of trapped atoms in each lattice site is similar and atomic temperature of in-phase and out-of-phase cases are same,  $\frac{\xi_{in ph.}}{\xi_{out ph.}}$  can be estimated as  $\frac{\zeta_{in ph.}}{\zeta_{out ph.}}$  where  $\zeta = \iiint f_{\text{atom}}(x, y, z) f_{\text{probe}}(x, y, z) dV$ . The spatial distribution of the trapped atoms at each site is  $f_{\text{atom}}(x, y, z)$ , and the intensity profile of the cavity probe is  $f_{\text{probe}}(x, y, z)$ . Based on the measured  $\frac{\xi_{in ph.}}{\xi_{out ph.}}$  of 6.2 (0.2), we can say that  $15 \mu\text{K}$  MOT atoms become as hot as  $38(6) \mu\text{K}$  atoms because of compression after loading MOT atoms adiabatically into the lattice with  $870 \mu\text{K}$  trap depth.

### 5.3 Atomic Coherence Times

In the cavity system, we measured the lifetimes and coherence times of optically-trapped atoms. We also studied the differential ac Stark shift of two hyperfine ground states, which limits atomic coherence.

The lifetime of optically trapped atoms in the cavity optical lattice is 1.1 s (Fig. 5.3 (a)). When the  $^{87}\text{Rb}$  atoms are loaded into a trap with an adiabatic ramping of the lattice, we expect to have a slightly higher temperature of MOT atoms due to the smaller lattice site volume. This heating results in some loss of the trapped atoms. Another source of atomic loss can be parametric heating, which results from the cavity lattice fluctuation, but our

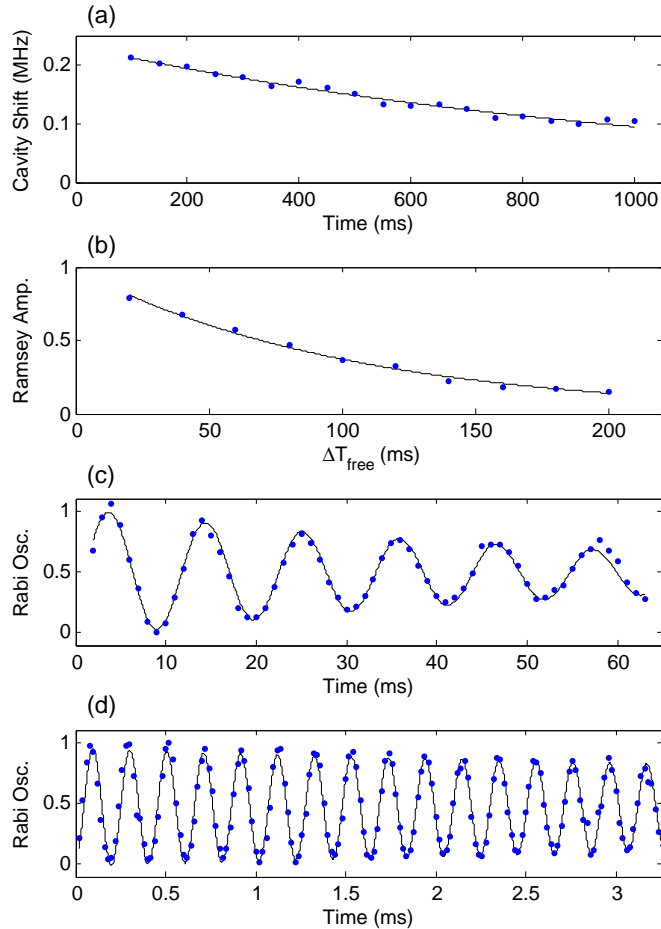


Figure 5.3: (a) The lifetime of the optically trapped atoms is 1.1 s. (b) The coherence time of Ramsey oscillation amplitude with  $\pi$  echo pulse is 0.21 s for  $2 \cdot \Delta T_{free}: \frac{\pi}{2} \rightarrow \Delta T_{free} \rightarrow \pi$  echo  $\rightarrow \Delta T_{free} (+\delta\phi_{\mu w}) \rightarrow \frac{\pi}{2}$ . (c) The coherence time of Rabi oscillation (93.2 Hz) is 57 ms. (d) The coherence time of Rabi oscillations (4.63 kHz) is 10.8 ms.

cavity with a few kHz linewidth minimizes high-frequency fluctuations because the cavity works as a low-pass filter. The scattering rate with the cavity optical lattice,  $870\,\mu\text{K}$ , is as small as  $0.58/\text{s}$ .

The coherence times of Rabi oscillation and Ramsey amplitude oscillation show our system's coherence as shown in Fig. 5.3 (b), (c), (d). The coherence time of the trapped atoms' two hyperfine ground states ( $|F = 1, m_f = 0\rangle$  and  $|F = 2, m_f = 0\rangle$ ) is much longer than that of the non-trapped atoms. The  $1/e$  coherence time of Rabi oscillation (93.2Hz) is 57ms, and the coherence time of Rabi oscillation (4.63 kHz) is 10.8 ms; a weak microwave field, having a slower Rabi oscillation and a smaller power-broadening, can address a more uniformly-distributed and narrower velocity class of atoms, which results in a smaller Rabi amplitude and a longer coherence time. The coherence time of the Ramsey oscillation amplitude with a  $\pi$  echo pulse informs us of our system's maximal coherence time. In a free evolution time  $\Delta T_{\text{free}}$  between two interferometric  $\pi/2$  microwave pulses, we drive a  $\pi$  echo pulse in order to rephase the collective atomic states. As the phase between two  $\pi/2$  microwave pulses varies, we can see the Ramsey oscillation amplitude. After each  $4\pi$  oscillation, the Ramsey oscillation amplitude fit to a sine wave is recorded. The  $1/e$  coherence time of the Ramsey fringe amplitude is 0.21 s with an echo pulse. This long coherence time is limited by the decoherence of the trapped atoms, which may be explained as follows: The atomic states of two hyperfine ground states experience a slightly different lattice potential, which makes their trapping frequencies different and spatially separates two atomic states for each atom. If the separation between two states is more than the deBroglie wavelength within a measurement cycle, decoherence occurs. The lattice-dependent ac Stark shift of our system (Fig. 5.4) is relatively small compared to a deep trap depth, but it is not negligible. We need an appropriately deep lattice for trapping atoms because of atomic temperature. If we could get atoms down to sub- $\mu\text{K}$  temperatures by evaporative cooling, a shallow lattice would be enough to trap atoms, and the lattice-dependent differential ac Stark shift of the lattice would become smaller. Then we would have a longer coherence time than we have now. In addition, the cavity probe carrier frequency-doubled from 1560nm low noise carrier could generate decoherence by a residual light shift because  $2\delta_m$  ( $\sim 80\,\text{MHz}$ ) (Fig. 3.13) is not a half of an FSR ( $\sim 700\,\text{MHz}$ ). If we can set the cavity probe carrier frequency

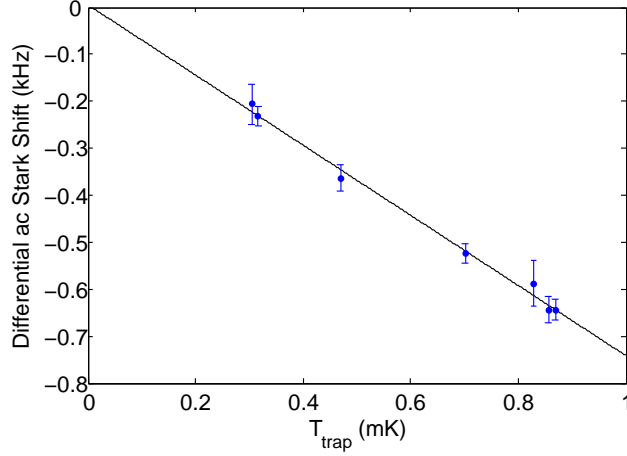


Figure 5.4: The trap-depth-dependent differential ac Stark shift of two hyperfine ground state vs. the estimated trap depth from the shift. The slope is  $-0.74 \text{Hz}/\mu\text{K}$ .  $T_{\text{trap}} = \frac{1}{k_B} U_{\text{dipole}}$ .

at the middle of two cavity resonance using a broadband fiber EOM, the residual light shift from the probe carrier can be distinguished, and the coherence time can be improved.

The differential ac Stark shift of two hyperfine ground states is measured depending on the lattice depth (Fig. 5.4). The overall ac Stark Shift by lattice depths corresponds to the level of  $5S_{1/2}$  to  $5P_{3/2}$ , but intense and far-detuned cavity optical lattices produce a slightly different ac Stark shift of the two states because of the 6.835GHz frequency difference between the two states. The microwave transition between the atomic clock state is shifted to the red by 644Hz, i.e., by a lattice of  $870 \mu\text{K}$ . Scanning the microwave transition frequency, the differential ac Stark shift of the two hyperfine ground states is measured according to the trap depth (Fig. 5.4).

## 5.4 Conclusion

Spatially identical atom-cavity coupling is realized by means of the dual-wavelength cavity. In the case of the in-phase atom registration, we are able to have trapped atoms identically coupled to a cavity probe as we have seen the constant ratio 6.2(0.2) of in-phase to out-of-phase atom registrations ( $\frac{\xi_{\text{in ph.}}}{\xi_{\text{out ph.}}}$ ) for three different detunings separated by an FSR. In the

cavity system, optically-trapped atoms have  $\sim 1.1$  s lifetime and  $\sim 0.21$  s coherence time. Since the trapped atoms with a finite temperature have atomic temperature distribution and spatial distribution in the lattice, each atom experiences a slightly different light shift at a given lattice depth. Sufficiently cold atoms with narrower atomic temperature distribution and more spatially localized distribution in the lattice can have a improved coherence time.

In the cavity system, there are some technical issues to be overcome for precision measurements. The thermal cavity length drift can be minimized by a feedback loop stabilizing the temperature of the cavity-chamber. The vibration noise also limits the quality of the cavity lock, and an additional vibrational noise reduction scheme would be useful.

The unique properties of our cavity system enable us to study high degrees of spin-squeezing and macroscopic self-trapping behavior due to collective atom-cavity interaction. Using our system, the cavity-aided atomic magnetometry (94) and cavity optomechanics (89) can be implemented and be improved because their performance is limited by spatially inhomogeneous atom-cavity coupling. Cavity-aided atomic thermometry for sufficiently cold atoms is also possible because the temperature of the trapped atoms in the lattice can be estimated based on the atom-cavity coupling ratio between in-phase and out-of-phase registrations.

# Chapter 6

## Macroscopic Self-trapping

As the spin-squeezed state improves measurement precision toward Heisenberg limit, so the macroscopic superposition state, known as Schrodinger Cat state, can yield higher-frequency sensitivity toward the Heisenberg limit (95). In our identically-coupled many-atom-cavity system (Chapter 5), presetting the cavity resonance at the mid-point of hundreds kHz atom-induced cavity shifts by a microwave pulse, it was expected to see the macroscopic superposition state utilizing a few kHz (cavity linewidth) atom-cavity interaction region at the mid-point of the full shifts. However, we observed not the superposition state but the self-trapped state.

Like a Josephon system (96; 97; 98), the collective oscillation of many atoms between two hyperfine levels by a microwave field can be interrupted by the collective atom-cavity interaction energy, i.e. the probe-induced ac Stark shift, that results in the energy offsets of the microwave transition. When the interruption occurs at the mid-point region of the full cavity shifts, the detection process of cavity transmitted photons, interacting with the collective atomic state, also affects the interrupted state to be localized.

### 6.1 Introduction

At the central region of a dual- $\lambda$  cavity, where MOT atoms are optically trapped, the anti-node of the 780nm cavity probe gets in-phase with that of 1560nm cavity lattice

(Chapter 5); the intensity maximum of 1560 nm cavity lattice and that of 780 nm cavity probe becomes well-overlapped at the region (Fig. 6.1 (b)), which allows us to have the in-phase atom registration and spatially homogeneous atom-cavity coupling. This unique property of our dual- $\lambda$  cavity enables us to regard these regularly spaced atoms in the lattice as one macroscopic ensemble of atoms that interact with a cavity mode. The trapped  $^{87}\text{Rb}$  atoms are  $\sim 10^4$  in the cavity lattice, and a frequency-doubled cavity probe (780 nm) registers the trapped atoms (Fig. 6.1); all the cavity parameters, including  $(g_{780}, \kappa_{780}, \kappa_{1560}, \gamma) = 2\pi \cdot (142, 3.99, 5.98, 3030)$  kHz (HWHM) are shown in Table 3.1, and the cavity lock scheme of one master laser are described in Chapter 3 (Fig. 3.13). The optically trapped atoms have 1.1 s lifetime and 57 ms Rabi coherence time. We measure the atom number by the atom-induced cavity shifts. The atoms are dispersively measured by demodulating the beat note signal between the cavity probe and the carrier light. In addition, the cavity photons are measured with an SPCM (single photon counting module) (Fig. 6.1 (b)).

## 6.2 Simulation

We simplify our atomic system to a three-level model (Fig. 6.1 (a)). The hyperfine ground states of  $|F = 2, m = 0\rangle$  and  $|F = 1, m = 0\rangle$  are regarded as  $|2\rangle$  and  $|1\rangle$ , respectively. We consider an ensemble of  $N$  identical three-level atoms whose ground states  $|2\rangle, |1\rangle$  are split by an energy  $\omega_a$  ( $= 6.835$  GHz) and are coupled via an optical transition of frequency  $\omega_c$  to an excited state  $|e\rangle$  with an atomic decay rate  $\gamma_\perp$ . In the optical Bloch sphere of an atomic clock state, a microwave drives Rabi oscillation between all ground states  $\prod_{i=1}^N |1\rangle_i$  ( $= |1\rangle_1 |1\rangle_2 \cdots |1\rangle_N$ ) and all excited states  $\prod_{i=1}^N |2\rangle_i$  ( $= |2\rangle_1 |2\rangle_2 \cdots |2\rangle_N$ ) (Fig. 6.1 (c)). Cavity modes with a linewidth  $\kappa$  and a frequency  $\omega_c$  are coupled to  $|2\rangle$  to  $|e\rangle$  with  $\Delta_p$  and to  $|1\rangle$  to  $|e\rangle$  with  $\Delta_p - \omega_a$  ( $\Delta_p < 0$  for a red-detuned probe). Atom-induced cavity shifts result from the atom's index of refraction, and we measure the collective atomic state depending on the atomic population difference. For simplicity, we assume that all atoms are equally coupled to the resonator, with a single-photon Rabi frequency  $g$ . We set the state of  $|2\rangle \langle 2|$  as zero energy.

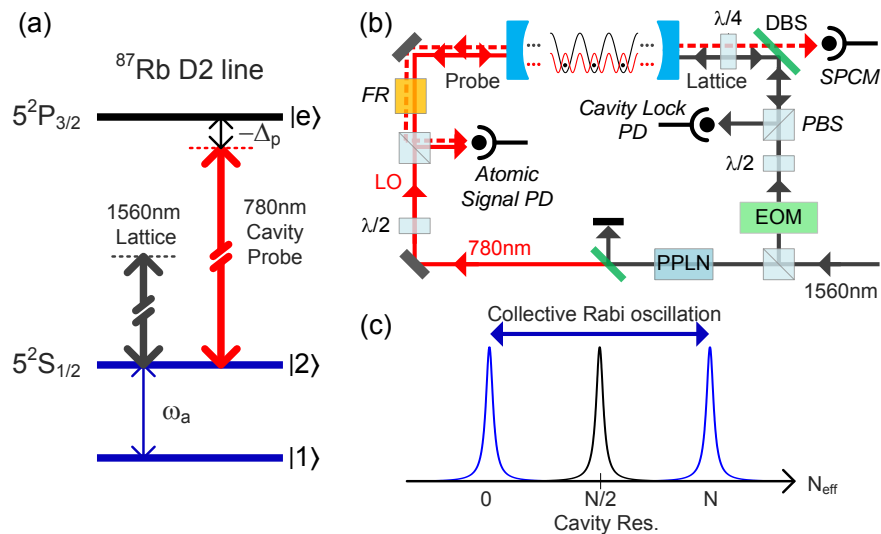


Figure 6.1: (a) Atomic energy level diagram, (b) Dual- $\lambda$  cavity with a cavity lattice and a cavity probe, (c) Collective Rabi oscillation; effective atom number which is  $N_{eff}$  ( $\simeq \frac{\delta v_{cav}}{g^2/|\Delta_p|}$ );  $\delta v_{cav}$  is the atom-induced cavity shift;  $\Delta_p = \omega_c - \omega_e$ , probe detuning;  $\omega_a (= 2\pi \cdot 6.85 \text{ GHz})$ , the ground-state hyperfine splitting. The  $\pi$  microwave pulse transfers the collective atomic states from all ground states ( $\prod_{i=1}^N |1\rangle_i$ ,  $N_{eff} = 0$ ) to all excited states ( $\prod_{i=1}^N |2\rangle_i$ ,  $N_{eff} = N$ ). The cavity becomes resonant about  $N_{eff} \simeq \frac{N}{2}$ .

As we present the theory in Chapter 2, for collective  $N$  atoms, the total Hamiltonian of macroscopic self-trapping is

$$\begin{aligned}\hat{\mathcal{H}}_{tot} = & (\delta_0 - \Delta) \hat{a}^\dagger \hat{a} + 0 \cdot \hat{J}_z \\ & + g^2 \hat{a}^\dagger \hat{a} \hat{J}_z \left( \frac{1}{\Delta_p} - \frac{1}{\Delta_p - \omega_a} \right) \\ & + \Omega_{\mu w} (\hat{J}_- + \hat{J}_+) + i \mathcal{E} (\hat{a}^\dagger - \hat{a}),\end{aligned}\quad (6.1)$$

where  $\delta_0 = \left( \frac{Ng^2}{\Delta_p} + \frac{Ng^2}{\Delta_p - \omega_a} \right)$ ,  $\hat{J}_z = \sum_{i=1}^N \hat{\sigma}_{z,i}$ ,  $\hat{J}_+ = \sum_{i=1}^N \hat{\sigma}_{21,i}$ , and  $\hat{J}_- = \hat{J}_+^\dagger$ ;  $N$  is an atom number in the trap. In our experimental regime of a few pW level cavity probe with  $|\Delta_p| \simeq 1.5 \text{ GHz}$ , we can ignore spontaneous emission from the cavity photons, but we include non-radiative inhomogeneous dephasing term that results from a state dependent trapping frequency.

$$\begin{aligned}\dot{\hat{\rho}} = & -i[\hat{\mathcal{H}}_{tot}, \hat{\rho}] + 2\kappa \hat{\mathcal{D}}[\hat{a}] \hat{\rho} \\ & + 2\gamma_d (\hat{\sigma}_z \hat{\rho} \hat{\sigma}_z - \hat{\rho}),\end{aligned}\quad (6.2)$$

where  $\hat{\sigma}_z = \hat{\sigma}_{22} - \hat{\sigma}_{11}$ ;  $\gamma_d$  is an inhomogeneous (non-radiative) dephasing rate that we measured. The actual physical system is collective atomic dynamics, such as  $\hat{\rho}(t) = \prod_{j=1}^N \hat{\rho}_j(t)$ , where  $\hat{\rho}_j(t)$  is the density operator for the  $j$ -th independent atom.

The interaction Hamiltonian  $\hat{\mathcal{H}}_{int}$  is  $g^2 \hat{a}^\dagger \hat{a} \hat{J}_z \left( \frac{1}{\Delta_p} - \frac{1}{\Delta_p - \omega_a} \right)$ . The atom-cavity interaction contributes to both the atom-induced cavity shift and the probe-induced ac Stark shift. By combining all the terms related to the cavity field, this atom-cavity interaction,  $\{(\delta_0 - \Delta) + g^2 \hat{J}_z \left( \frac{1}{\Delta_p} - \frac{1}{\Delta_p - \omega_a} \right)\} \hat{a}^\dagger \hat{a}$ , leads to the atom-induced cavity shift. The terms of the atoms,  $\{0 + g^2 \hat{a}^\dagger \hat{a} \left( \frac{1}{\Delta_p} - \frac{1}{\Delta_p - \omega_a} \right)\} \hat{J}_z$ , mean that the probe-induced ac Stark shift varies the detuning of the microwave atomic transition and has the potential to control the collective Rabi oscillation of  $\Omega_{\mu w} (\hat{\sigma}_{21} + \hat{\sigma}_{12})$ .

With an appropriate cavity probe, a feedback mechanism interrupts the collective Rabi oscillation (Fig. 6.6, 6.7) as follows: With an initial cavity resonance condition at the mid-point region of the full atom-induced cavity shifts, if the collective atomic state approaches the mid-point region from all ground state atoms by the microwave Rabi oscillation, the increased intracavity photons, shifting the atomic microwave transition and causing an off-resonant microwave field by ac Stark shift, slow down the approach of collective atomic

state to the mid-point. If the collective atomic state recedes from the mid-point region to all ground-state atoms, the decreased intracavity photons, causing a closely resonant microwave field by reduced ac Stark shift, make the collective atomic state to approach the mid-point. If the intracavity photon is not enough to interrupt the oscillation, the collective atomic state moves over the mid-point region, the Rabi oscillation continues. Therefore, the feedback mechanism with an appropriate cavity probe can freeze collective atomic state as the self-trapped state around the mid-point region with the aid of the measurement-induced state localization; the measurement process of cavity-transmitted photons interacting with atoms in a nondestructive way affects the atomic states because the atoms and the photons are weakly entangled. The detection process of cavity-transmitted photons by an SPCM, i.e. photon-counting process, can be modeled by quantum trajectory, and the measurement-induced state localization during the interruption can be simulated by Quantum Monte Carlo (Chapter 2).

This numerical simulation expects the atom-cavity system evolves from the normal Rabi oscillation to the self-trapped state as the atom-cavity interaction, i.e. the cavity probe's intensity, increases (Fig. 6.2). Between the normal Rabi oscillation and the self-trapped state (Fig. 6.2 (b)), Rabi oscillation with some macroscopic superposition states occurs with low cavity transmission, but the measurement process collapses the coherence of the superposition state. After this transition regime, there are self-trapped states with high cavity transmission ((Fig. 6.2 (c), (d)) and faster Rabi oscillation with low cavity transmission (Fig. 6.2 (e)), in sequence.

When we focus on the transition region (Fig. 6.3) where macroscopic superposition states, such as  $\frac{1}{2}(|\frac{N}{2} + m\rangle + |\frac{N}{2} - m\rangle)$ , occur in a short time at time  $\simeq 650, 950, 1150$ , where  $m$  is an atom number which represents the degree of state separation ( $0 < m \leq \frac{N}{2}$ ). When the atom-induced cavity shift of  $2m \cdot \frac{g^2}{\Delta_p}$  is large enough than the cavity linewidth, we can see an abrupt cavity transmission drop. For a large enough  $m$ , the superposition state of  $|\frac{N}{2} + m\rangle$  and  $|\frac{N}{2} - m\rangle$  results in the atom-induced cavity shifts of  $(\frac{N}{2} + m)\frac{g^2}{\Delta_p}$  and  $(\frac{N}{2} - m)\frac{g^2}{\Delta_p}$ , respectively. Both shifts make the cavity to be out of resonance because we preset the cavity resonance at the mid-point of the full cavity shifts. Because of its fragility and a short coherence time, the quantum measurement process makes the superposition state to be collapsed into one of the both state. As shown in Fig. 6.3, we can clearly observe the

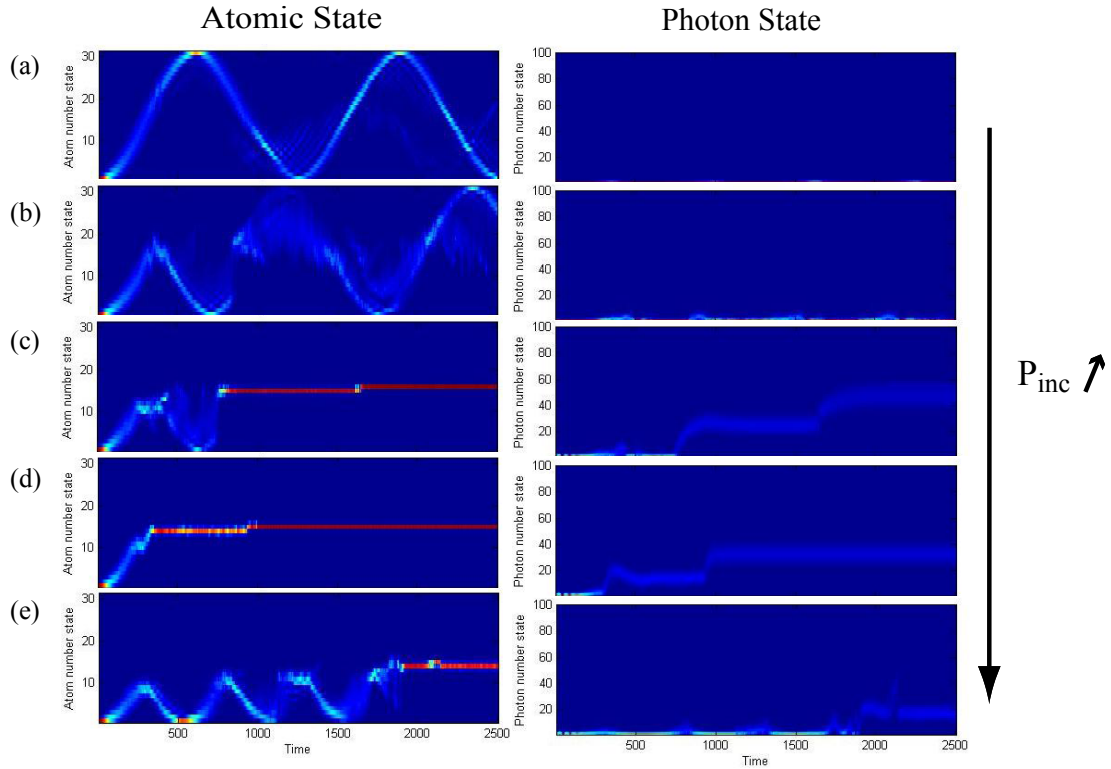


Figure 6.2: Simulation results of an atom-cavity system according to the increased incident cavity photons. (a) Normal Rabi oscillation with low cavity transmission. (b) Rabi oscillation with some macroscopic superposition state. (c), (d) Self-trapped state having constant cavity transmission. (e) Faster Rabi oscillation with low cavity transmission; the Rabi frequency is  $\Omega_{\mu w} = 1\text{ kHz}$ , the time step is  $dt = 800\text{ ns} = 2\text{ ms}/2500$ , and the cavity photon life-time is  $20\text{ }\mu\text{s}$ . Because we cannot simulate many atoms as  $\sim 10^4$ , the atomic state basis and photon state basis represent more atomic states and more photons state for studying the collective atom-cavity interaction behavior qualitatively; spontaneous emission and inhomogeneous dephasing can be neglected for the far-detuned and weak cavity probe.

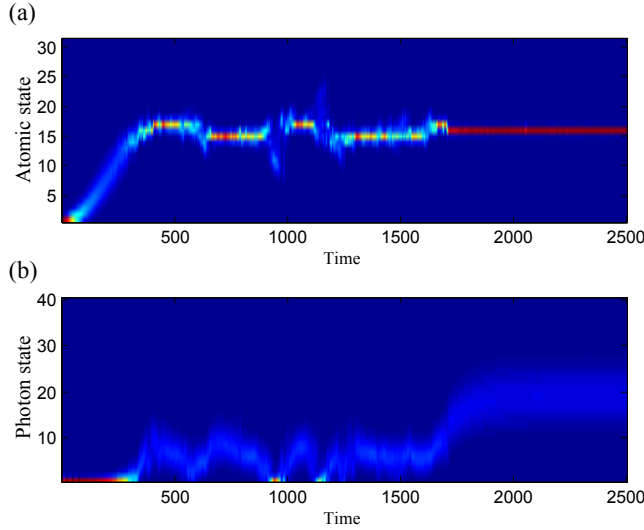


Figure 6.3: The self-trapping by the collective atom-cavity interaction. (a) Atomic states. (b) Photon states; at time  $\simeq 650$ , time  $\simeq 950$ , and time  $\simeq 1150$ , macroscopic superposition states occur, and the cavity transmission suddenly drops because the cavity is only resonant at the mid-point region of the full shifts; each component of superposition states does not satisfy the cavity resonant condition.

created superposition states to be projected one of the states around time  $\simeq 950$  and 1150. Around time  $\simeq 950$ , we also checked the evolution of the density matrix of atomic state and the q-function of photon state (Fig. 6.4), which shows the off-diagonal elements, i.e. the coherence between two atomic states; this can be the evidence for the macroscopic superposition states (Fig. 6.4 (c)). In the simulation, the time scale of the coherence is  $\sim 10 \mu s$  less than the cavity lifetime  $20 \mu s$ . Therefore, in real experiments, it is difficult to measure this effect because the transmission drop is not longer than the cavity lifetime; the measurement process of cavity transmitted photons, interacting with atoms, affects the created macroscopic superposition state to live shortly. If we do not measure the state or measure the state nondestructively, the macroscopic superposition state can live longer.

The macroscopic superposition state can be generated in two different ways (Fig. 6.5). First, the self-trapping protocol with a feedback mechanism, sensing the cavity transmission more than a threshold and then turning off a microwave field, can hold a macroscopic superposition state (Fig. 6.5 (a)); the incident cavity probe and the microwave field are kept on like the self-trapping protocol. Second, similar to the spin-squeezing protocol, after the

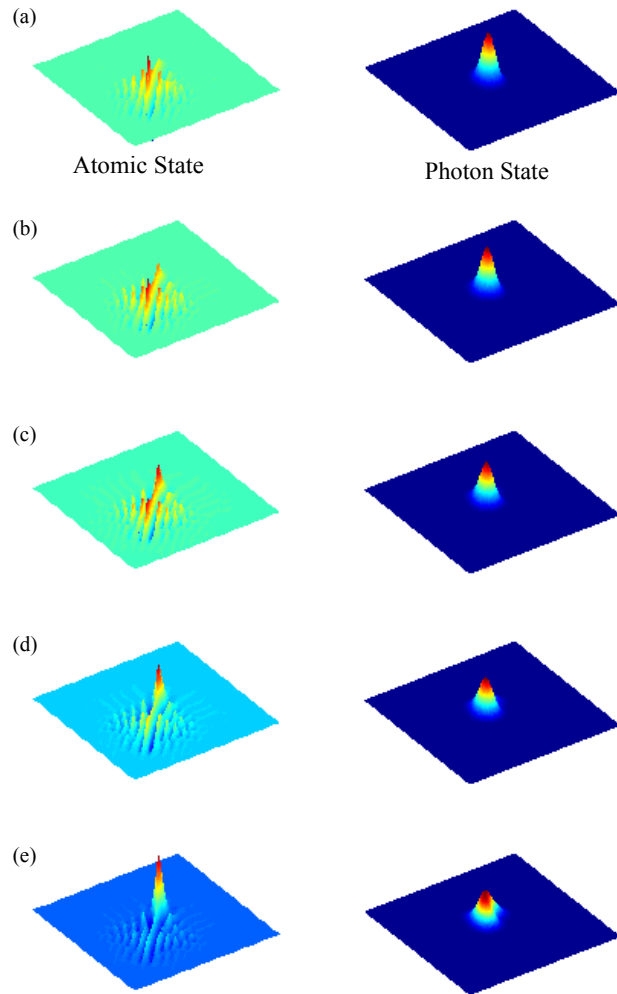


Figure 6.4: Evolution of the collective atomic state (density matrix) and cavity photon state (q-function): From a simulation (Fig. 6.3), we captured five shots when (a) time = 950, (b) time = 960, (c) time = 964, (d) time = 967, and (e) time = 970. We can see the coherence of macroscopic superposition states of atoms; off-diagonal elements of the density matrix remain.

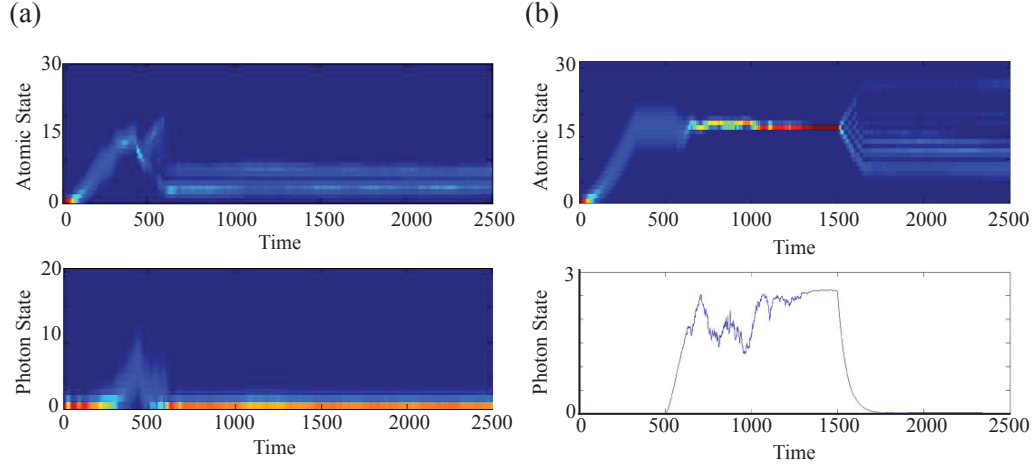


Figure 6.5: Macroscopic superposition state generation. (a) Self-trapping protocol with a feedback mechanism. (b) Spin-squeezing-like protocol with an interfering microwave.

initial state preparation of the coherent spin state with a  $\frac{\pi}{2}$  pulse (no cavity probe), the collective atomic state like the spin-squeezed state close to an atom number state is generated by a proper cavity probe. Then, with no cavity probe, we turn on a microwave field, making the state to be a interfered superposition state (Fig. 6.5 (b)).

### 6.3 Readout after or during the interaction

In the experiment, firstly, we measured the atomic states after the atom-cavity interaction, and secondly, we also measured the atomic states and cavity photons during the atom-cavity interaction. Because of the initial cavity resonance at the mid-point region of the full atom-induced cavity shifts, the Rabi interruption occurs around the mid-point region by the probe-induced ac Stark shift (Fig. 6.1 (c)); the atom-cavity system exhibits abrupt threshold behavior from the Rabi oscillation to the self-trapped state as a function of the incident cavity photons for a Rabi frequency.

We measured the collective atomic state after the interruption (Fig. 6.6). The probe-induced ac Stark shift as a feedback mechanism controls the coherent Rabi oscillation. Around the mid-point region of the full shifts, the interrupted Rabi oscillation occurs for enough incident cavity photons.

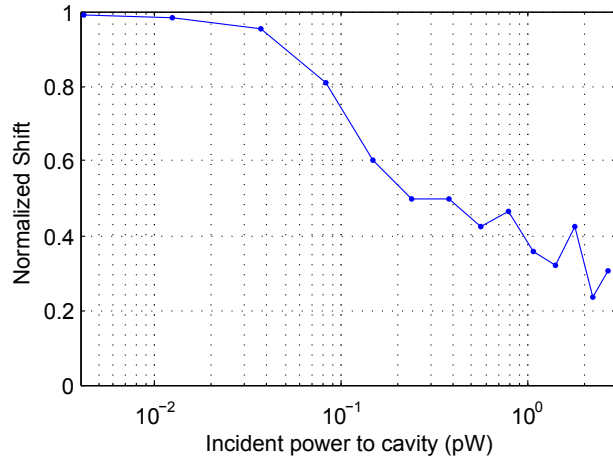


Figure 6.6: Normalized atom-induced cavity shifts vs. the incident cavity power. All ground state atoms transfer to all excited state atoms by a  $\pi$  pulse with very low intracavity photons. With an appropriate intracavity photons, collective atomic state transferring from all ground states to all excited states is interrupted around the mid-point region of the full shifts. The transition threshold is shown with a 92.1 Hz Rabi frequency.

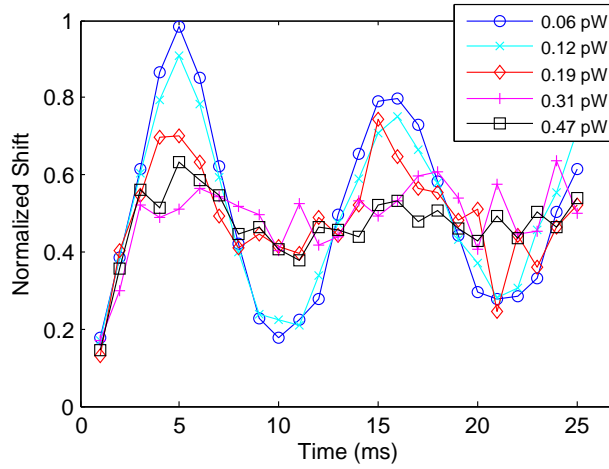


Figure 6.7: Readout after the atom-cavity interaction; QND interrupted Rabi oscillation with a microwave of 92.1 Hz Rabi-frequency ( $\tau_\pi = 5.4\text{ ms}$ ). We are able to interrupt the Rabi oscillation with  $0.2 \sim 0.3\text{ pW}$  light. A  $0.25\text{ pW}$  light corresponds to  $1 \times 10^6\text{ photons/s}$ , and with the cavity build-up to time of  $20\mu\text{s}$ , this corresponds to  $\sim 20$  photons.

We realized  $\sim 20$  photon level controllability of the collective Rabi oscillation. As shown in Fig. 6.7, the collective atomic state coherently evolve by a microwave field. All these measurements are taken using the 780 nm light retro-reflected optical path like PDH cavity lock. Using this setup, it is difficult to measure collective atomic state and cavity photons at the same time because the retro-reflected beat note signal between a carrier and a cavity side-band needs an appropriately high light level of the carrier and the probe at a high modulation frequency (9 GHz). After the non-destructive collective atom-cavity interaction at the level of several tens of photons, we measured the collective atomic states destructively at the end of incremental microwave pulses. Then we can see the transition threshold and the macroscopic self-trapped state. The photon-detector (Hamamatsu G4179), which measures the atom number at the retro-reflected optical path, needs an appropriately higher photon level for the photon shot-noise limited measurements (Fig. 6.1(b)). During the atom-cavity interaction, the spontaneous emission is low with a weak ( $\sim 0.25$  pW) and far-detuned ( $\sim 1.5$  GHz) cavity probe. At a threshold optical power, the spontaneously-emitted photons during the interaction time  $\tau_{int} \lesssim 0.1\tau_\pi$  is  $R_{scatt} \cdot \tau_{int} \lesssim 0.005$ , where  $R_{scatt} = \Gamma \frac{\Omega^2}{\Delta^2}$ . In the regime of this low-level cavity photon, we can say that this self-trapping behavior may not come from a probe-induced dephasing. Experimentally, if we observe the oscillation behavior of  $\hat{J}_x$  and  $\hat{J}_y$  components with the self-trapping behavior of  $\hat{J}_z$  component, the oscillation behavior will be a strong evidence to prove the coherence of the self-trapped state: In the optical Bloch sphere, the collective atomic state  $\hat{J}$  can be represented by  $\hat{J}_x$ ,  $\hat{J}_y$ , and  $\hat{J}_z$ , and we usually measure  $\hat{J}_z$  component (Fig. 6.7).  $\hat{J}_x$  and  $\hat{J}_y$  components can be measured like  $\hat{J}_z$  because  $\hat{J}_x$  can be projected to  $\hat{z}$ -axis after driving a  $\frac{\pi}{2}$   $\mu w$  pulse, and  $\hat{J}_y$  can be projected to  $\hat{z}$ -axis after driving a phase-shifted  $\frac{\pi}{2}$   $\mu w$  pulse.

Furthermore, we measured the cavity transmission during the collective atom-cavity interaction with an SPCM. The collective atomic state seems to persist in the mid-point region of the full cavity shifts ( $N_{eff} = \frac{N}{2}$ ) based on the high cavity transmission data because all-excited state or all-ground state results in no cavity transmission. This behavior is similar to what we expected (compare Fig. 6.8 with Fig. 6.2). The SPCM enables us to measure the transmitted cavity photons and estimate the collective atomic state. The atom-induced cavity shift can be measured by the transmitted photons, but we need a clean local oscillator. As shown in Fig. 6.8, the collective atom cavity interaction happens as

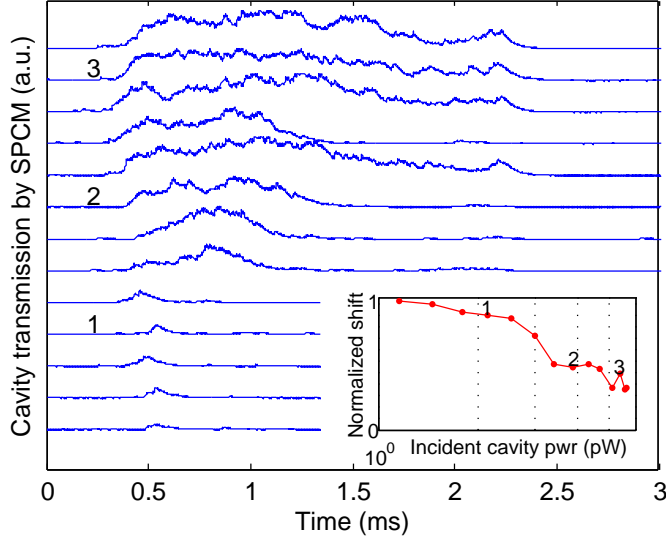


Figure 6.8: Readout during the atom-cavity interaction as we increase the incident cavity photons. The transmitted cavity photons during the atom-cavity interaction is continuously measured with an SPCM, and the transition threshold (in-set) is measured after the atom-cavity interaction with a photodiode at the retro-reflected path. For this measurement, we used a microwave of 183.5 Hz Rabi frequency ( $\tau_\pi = 2.7\text{ ms}$ ). For a higher Rabi frequency  $\Omega_{\mu\nu}$  results in a shorter interaction time  $\tau_{int}$ , and we need more threshold photons.

we increase the incident cavity photons: At the data 1 (Fig. 6.8), we observed a very low cavity transmission with a low incident cavity photons. When the number of the photons is not enough to interrupt the microwave transition of atomic clock states, a normal Rabi oscillation continues. At the data 2 (Fig. 6.8), the cavity transmission starts to be high around the transition threshold where the self-trapped state begins. At the date 3 (Fig. 6.8), the self-trapped state continues by the feedback mechanism of the ac Stark shift and the non-destructive measurement-induced state localization.

## 6.4 Conclusion

We demonstrated the self-trapped state of hyperfine two ground states by collective atom-cavity interaction. Collective Rabi oscillation between two hyperfine ground states can be interrupted by the probe-induced ac Stark shift, and the collective Rabi oscillation is frozen

as the self-trapped state with the aid of both the feedback mechanism of the ac Stark shift and the measurement-induced state localization.

# **Chapter 7**

## **Raman Laser**

We demonstrated a Raman laser using cold  $^{87}\text{Rb}$  atoms as the gain medium in a high finesse optical cavity. We observed robust continuous wave lasing in the atypical regime where single atoms can considerably affect the cavity field. Consequently, we discovered atypical lasing threshold behavior in the system causing jumps in lasing power, and propose a quantum-mechanical model (Chapter 2) and a semi-classical model in this chapter to explain the effect. We also measured the intermode laser linewidth, and observed values as low as 80Hz. The tunable gain properties of this laser suggest multiple directions for future research.

### **7.1 Introduction**

The improvement of laser performance influences ultrahigh-precision spectroscopy, metrology, and many quantum optics experiments. Particularly, these applications stand to benefit substantially from the potential advance of gain media that can be engineered for gain bandwidth, index of refraction, and dispersion properties. For example, recent developments have indicated that anomalous dispersion in a lasing medium can result in increased sensitivity of lasing frequency to the laser cavity length (99). Such a system could be employed as a next-generation (active) interferometer design for gravity wave detection. Another example concerns the state-of-the-art ring laser gyroscopes (RLG)

(100) that use differential frequency shifts in two counter-propagating ring cavity laser modes for rotation sensing (101).

With the Raman gain in an atomic system, we can precisely control the gain medium property, varying the pumping mechanism. Recent experiments in heated atomic vapors, pumped by light at two optical frequencies, for instance, demonstrate dispersion tunability from the normal to the anomalous regimes (99), opening up the possibility of integration of this property into lasing systems. The use of an atomic Raman gain medium for a laser was first demonstrated using a heated vapor cell (102), and it has since been realized with cold atoms (103; 104). These experiments show narrow gain bandwidth properties, but are limited in laser linewidth by operating with low-finesse resonant cavities. Proposals for other types of cold atom lasers are also generating considerable interest for their potential ultra-narrow linewidths (91).

In our experiment, a 2D two-dimensional MOT loads atoms into the three-dimensional MOT (3D-MOT) at the central region of the cavity. The atoms undergo a two-photon Raman transition driven by a frequency tunable pump laser which excites the atoms from the  $F = 2$  hyperfine ground state to an intermediate virtual state. An allowed cavity resonance from this intermediate state down to the  $F = 1$  hyperfine ground state allows completion of the two-photon process. The atoms are driven back to  $F = 2$  by the repump beam associated with the 3D-MOT, allowing continuous laser output. The relevant atomic energy levels and laser frequencies are shown in Fig. 7.1(a). We can excite different spatial modes of the cavity, as shown in Fig. 7.1(b), by changing the frequency of the Raman pump to select the cavity mode whose frequency satisfies the overall two-photon resonance condition.

All the details of the dual- $\lambda$  cavity chamber and cavity parameters, including  $(g_{780}, \kappa_{780}, \kappa_{1560}, \gamma) = 2\pi \cdot (142, 3.99, 5.98, 3030)$  kHz (HWHM) are shown in Table 3.1 and Chapter 3. The cavity's longitudinal mode spacing is given by the free spectral range  $\Delta\nu_{fsr}$ , and the transverse mode spacing  $\Delta\nu_{tms} = \frac{1}{2}\Delta\nu_{fsr} + 37.5$  MHz. This results in a spacing of  $2\Delta\nu_{tms} - \Delta\nu_{fsr} = 75$  MHz between nearest transverse modes, a separation much greater than the gain bandwidth of 5 MHz.

A schematic of the experimental setup is shown in Fig. 7.1(c). The input laser light at 1560 nm is split by a polarizing beam splitter, with one path used to stabilize the frequency of the light to the cavity using a Pound-Drever-Hall (PDH) method (69). The majority

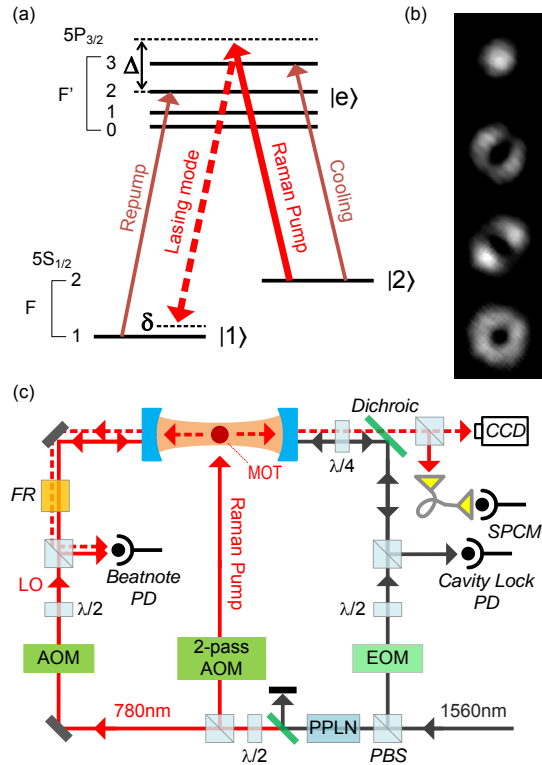


Figure 7.1: (a) Energy level diagram of  $^{87}\text{Rb}$  including relevant laser frequencies for the Raman process, as well as the cooling and repump light frequencies associated with the magneto-optical trap. (b) Sample CCD images showing relevant spatial modes of the laser. Top to bottom: TEM<sub>00</sub>, TEM<sub>01</sub>, TEM<sub>10</sub>, TEM<sub>01</sub> + TEM<sub>10</sub>, respectively. (c) Schematic of the experiment. LO is local oscillator; AOM, acousto-optical modulator; EOM, electro-optical modulator; FR, Faraday Rotator; PBS, Polarizing Beam Splitter; DBS, dichroic beam splitter;  $\frac{\lambda}{2}$ , half-wave plate;  $\frac{\lambda}{4}$ , quarter-wave plate.

of the light goes in the other path, where it is frequency doubled in a periodically poled lithium niobate (PPLN) waveguide crystal to generate the 780 nm light used for the Raman pump laser and the local oscillator beam. This way of generating the 780 nm light ensures that the Raman transition is essentially insensitive to cavity length drifts. A double-passed acousto-optical modulator allows for tuning of the pump beam frequency, enabling fast switching between spatial modes or simultaneous lasing of multiple modes. We note that the linewidth of the Raman pump does not need to be narrow, as we observe lasing equally well with a MHz linewidth pump.

Light emitted from one cavity mirror is split by a polarizing beam splitter. One beam is incident on a CCD camera to image the spatial mode intensity profile, while the other is incident on a single-mode fiber connected to a Perkin-Elmer ARQH-13 avalanche photodiode single photon counting module (SPCM). Short pulses from the SPCM, corresponding to a photon detection, are integrated, and a time trace is measured on an oscilloscope. Light emitted from the other cavity mirror is combined with a local oscillator beam and incident on a fast photodiode. The resulting beat note gives us the laser's optical frequency relative to the known local oscillator frequency.

The lasing threshold of TEM<sub>00</sub> cavity modes and the instantaneous beat note frequency of a donut mode were measured by a Perkin-Elmer ARQH-13 avalanche photodiode single photon counting module (SPCM) running in Geiger mode. In addition, the heterodyne beat note between TEM<sub>00</sub> lasing mode and a reference beam measured by a photo-detector packaged with a transimpedance amplifier (Finisar HFD6380-418) proved that this lasing comes from the Raman two-photon process. We also studied interesting threshold jumping effect explained with our theoretical prediction related to the lasing-induced ac Stark effect.

## 7.2 Lasing Threshold

We measured the threshold of Raman lasing as we loaded MOT atoms into the center of a cavity chamber with a constant pump intensity; in the measurement cycle of  $\sim 10$  sec, we turn the MOT magnetic field off and on. There is an atom-number dependent lasing threshold. The effective atom number  $N_{eff}$  in the cavity mode is related to atomic clouds which are geometrically overlapped with the cavity mode, where  $N_{eff} = \delta v_{cav}/(g^2/\Delta_p)$ ;

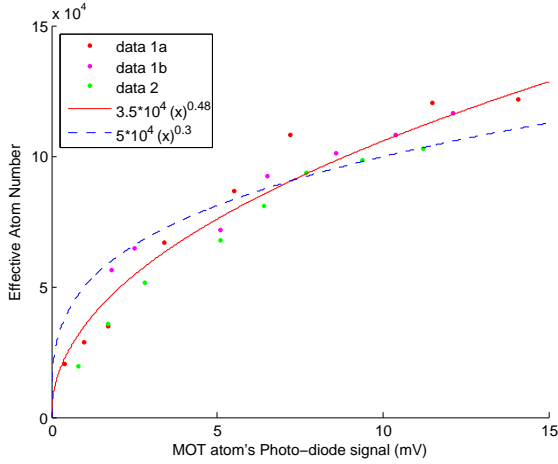


Figure 7.2: Effective atom number  $N_{eff}$  vs. cavity shift.

$\delta v_{cav}$ , the atom-induced cavity shift;  $\Delta_p$ , the cavity probe detuning. Loading MOT atoms, we measured atomic fluorescence using a photodiode, and we calibrated  $N_{eff}$  (Fig. 7.2).

The atypical threshold behavior of the Raman lasing can be described by the lasing-induced ac Stark shift (Fig. 2.12). In the case of a blue-detuned lasing mode ( $\Delta > 0$ ) and positive  $\delta$ , an abrupt jump in the lasing output occurs. The initiated lasing mode shifts the  $F = 1$  state up, and the gain increases more. As a result, the lasing output increases more, and the ac Stark shift increase further before it becomes an equilibrium (Fig. 2.12 (a)). However, in the case of a blue-detuned lasing mode ( $\Delta > 0$ ) and negative  $\delta$ , the gain decreases when the lasing mode shifts  $F = 1$  state up. Therefore, this effect disappears (Fig. 2.12 (b)). We observed the lasing threshold behavior by varying the gain medium ( $N_{eff}$ ) and the pump intensity ( $I_{pump}$ ) in the lasing mode (Fig. 7.3). The lasing intensity profile (Fig. 7.4) also shows unusual threshold behaviors and asymmetric shapes. Specific to the current setup, the flexibility in the pumping mechanism and the relatively narrow gain bandwidth leads to further interesting nonlinear phenomena in lasing behavior. For certain parameters, as the gain is increased, the onset of lasing takes place with an abrupt jump in lasing power, defying the traditional threshold behavior.

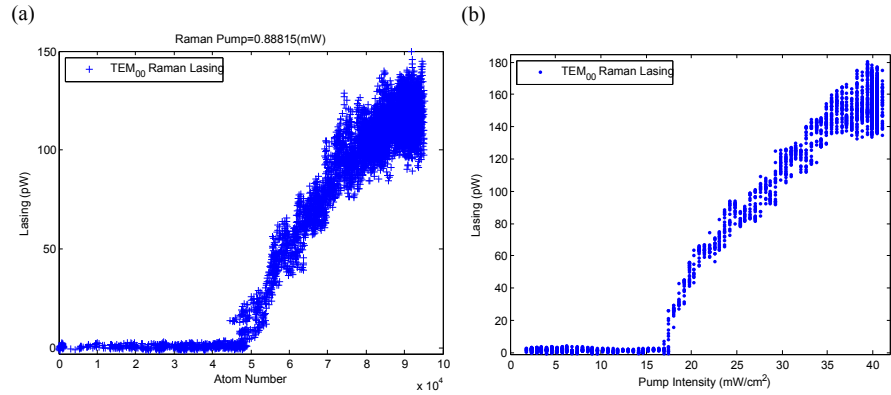


Figure 7.3: Lasing output power as a function of (a)  $N_{eff}$  and (b)  $I_{pump}$ .

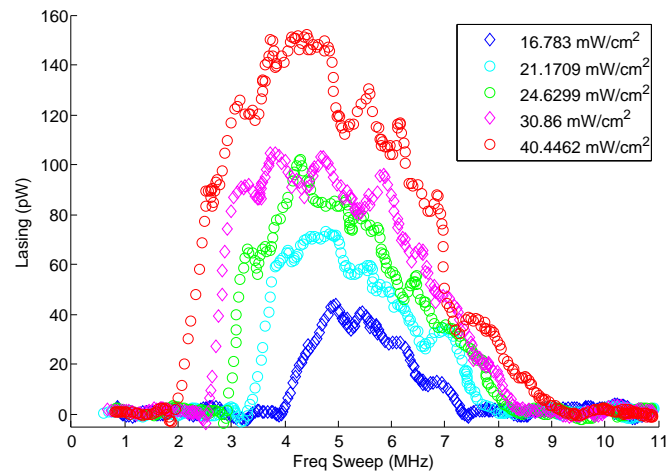


Figure 7.4: Lasing intensity profile vs. pump intensity; as sweeping Raman pump frequency  $\Delta f_p$ , we observed lasing output power  $P_{out}$  at several Raman pump intensity  $I_{pump}$ .

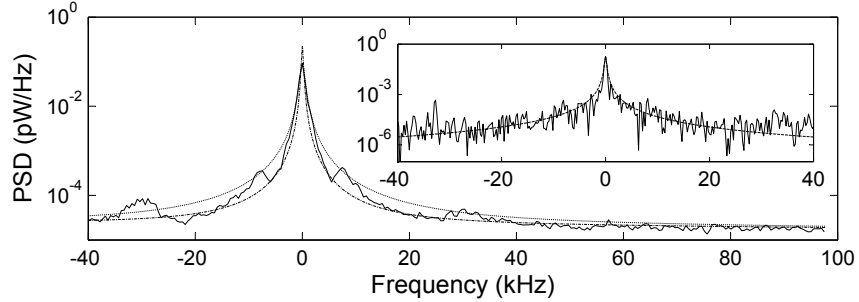


Figure 7.5: Measured beat note power spectral density between the  $\text{TEM}_{01}$  and  $\text{TEM}_{10}$  modes at  $25 \text{ mW/cm}^2$  pump intensity, showing an average of 100 spectra (2 ms windows) that are centered before averaging. Dotted lines: Lorentzian fit with HWHM of 448 Hz, dash-dotted lines: Lorentzian fit to the tails with HWHM of 172 Hz. Inset: A single realization of the spectrum for a particularly stable 4 ms window; dashed line: Lorentzian fit with HWHM of 160 Hz.

### 7.3 Lasing Linewidth and Frequency Shift

We extract the laser's intermode linewidth, which is insensitive to cavity length fluctuations, from the beat note between two lasing modes. Specially, by tuning the pump frequency we make the  $\text{TEM}_{01}$  and  $\text{TEM}_{10}$  modes lase simultaneously (Fig. 7.1 (b)), and partially couple these modes into a single mode fiber leading to the SPCM. These two modes are non-degenerate (due to geometrical imperfections in the cavity mirrors) by approximately 515 kHz, a value well within the gain bandwidth. A frequency spectrum extracted from a particularly stable 4 ms window of the recorded time-domain signal is shown in the inset of Fig. 7.5. A Lorentzian fit indicates a HWHM of 160 Hz, corresponding to an instantaneous intermode linewidth of 80 Hz for the convolution of two identical Lorentzian lineshapes. Similarly, a minimum average instantaneous linewidth of 224 Hz is obtained by averaging centered spectra derived from consecutive 2 ms windows (Fig. 7.5). Note that the purpose of the centering procedure is to eliminate broadening due to central lasing frequency drift. The fact that a good Lorentzian fit to the peak overshoots the tails is an indication of excess low-frequency noise on the instantaneous frequency. It is known that the quantum limited linewidth could, in principle, be inferred from the Lorentzian tails of a lineshape at high frequencies (105). In our case, although small side lobes and a high baseline partly obscure the tails of the distribution, a Lorentzian fit to these tails still represents an upper bound on

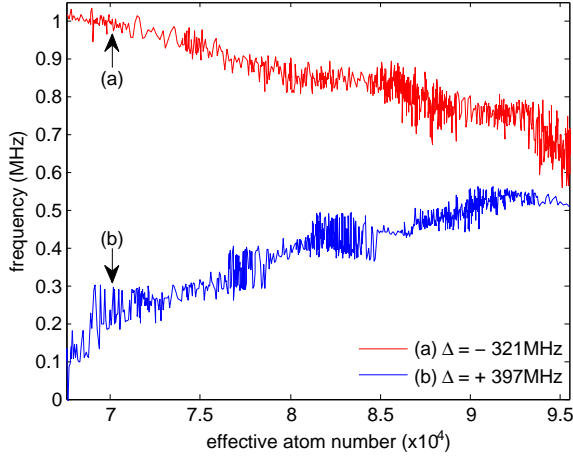


Figure 7.6: The center frequency shift of  $\text{TEM}_{00}$  mode as a function of  $N_{\text{eff}}$  for (a) red-detuned Raman pump ( $\Delta = -321\text{MHz}$ ) and (b) blue detuned Raman pump ( $\Delta = +397\text{MHz}$ ), where  $\Delta = \omega_p - \omega_{e2} = \Delta_{rmn}$  (Chapter 2). The opposite slopes are due to the positive and negative susceptibilities associated with the red and blue detuned configurations respectively. Relative positioning of the two curves is arbitrary.

the quantum limited linewidth of the laser. This procedure yields 86 Hz, and is insensitive to the window size used. Comparison with theory is subtle, but as a reference the Schawlow-Townes linewidth limit (without taking into account amplitude-phase noise coupling, or incomplete population inversion) is 0.25 Hz.

The atomic medium as gain medium results in lasing frequency variation. The shift of lasing frequency depends on the detuning of lasing mode. Depending on the detuning (blue-detuned or red-detuned), lasing mode experiences different index of refractions. In our Raman lasing setup, we tried to cancel the refractive index, and we expect the lasing frequency drift becomes a much smaller and narrower linewidth laser might be achieved. However, for the currently investigated configurations, the susceptibility is non-zero, causing an atom number dependent shift of the lasing mode. The absolute lasing frequency is measured in a heterodyne configuration by beating the light with the local oscillator beam incident on a high-frequency photodiode.

A complete understanding of the lineshape and noise sources are beyond the scope of this study. However, we would like to point out the following observations. Due to their motion inside of the MOT, the atoms in the lasing modes are expected to get completely

replenished within 1 ms, thus, the difference in the atom numbers seen by the TEM<sub>01</sub> and TEM<sub>10</sub> modes could in principle fluctuate significantly in the course of the spectral measurements. As a reference, the shot noise level is  $\pm 150$  atoms. Utilizing the measured generic atom number dependence of the absolute lasing frequency (Fig. 7.6), it can be inferred that only about  $\pm 20$  atoms (well below the shot noise level) of a fluctuation could account for the observed 224 Hz linewidth. Similarly, about  $\pm 90$  atoms of a fluctuation could account for the observed longer term ( $5 \sim 100$  ms) frequency fluctuations of  $\sim 900$  Hz in standard deviation.

## 7.4 Semi-classical Model

Fig. 7.7(a) shows lasing power as a function of Raman pump intensity for slightly differing pump frequencies with positive single-photon detuning  $\Delta$ . The pump frequency variation essentially changes the two-photon detuning  $\delta$  shown in Fig. 7.1(a). The jumping behavior in lasing power is observed for positive  $\delta$ . As the pump intensity is cycled up and down, the onset and extinction of lasing take place at different pump intensities. When  $\delta$  is negative, this behavior disappears. A simple mechanism based on the ac Stark shift experienced by the  $F = 1$  state seems to qualitatively capture this effect. For positive  $\Delta$ , the onset of any lasing will shift the  $F = 1$  state up, in turn decreasing  $\delta$  if it was positive initially, hence increasing the gain and further increasing the lasing, and the Stark shift until equilibrium is reached. For negative  $\delta$  the Stark shift will decrease the gain, resisting the increase in lasing.

The proposed mechanism can be modeled with a three level system (levels  $|1\rangle$ ,  $|2\rangle$ ,  $|e\rangle$  in Fig. 2.12), disregarding the details pertaining to the repump and cooling beams, and taking their effects into account phenomenologically by adding a population transfer rate  $\Gamma_{12}$  from  $|1\rangle$  to  $|2\rangle$  and additional decoherence rates. The gain associated with an ensemble of atoms can be calculated by solving for the steady-state values of the density matrix elements in a standard fashion (100). The quantity of interest is the density matrix element  $\rho_{e1}$  giving the atomic polarization at the lasing transition frequency  $\omega_l$  which can be expressed as a sum of one-photon and two-photon terms:

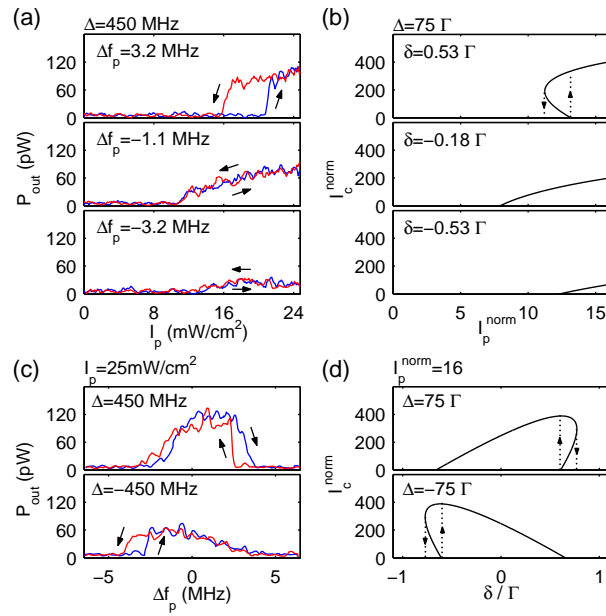


Figure 7.7: (a) Cavity output power as a function of pump intensity for die rent values of the relative pump frequency  $\Delta f_p$ .  $\Delta f_p = 0$  is chosen to correspond to the experimentally inferred  $\delta = 0$  condition. (b) The corresponding calculated steady-state intracavity intensity. The arrows indicate the expected jumps in the lasing intensity depending on the sweep direction. (c) Cavity output power as a function of  $\Delta f_p$  for opposite single photon detuning. (d) Calculated steady-state intracavity intensity. Parameters for the calculated curves are  $A = 0.135$ ,  $\gamma_1 = 0.625\Gamma$ ,  $\Gamma_{12} = 0.1\Gamma$ . We have a red-detuned Raman lasing ( $\Delta < 0$ ) and a blue-detuned Raman Lasing ( $\Delta > 0$ ).

$$\begin{aligned}
\rho_{e1}^{(1ph)} &= \frac{1}{2(\Delta+i\gamma_{e1})}(\rho_{ee} - \rho_{11}) \\
\rho_{e1}^{(2ph)} &= \frac{|\Omega_p|^2}{4\Delta^2} \frac{1}{2(-\delta' + i\gamma_{21})}(\rho_{22} - \rho_{11}) \\
\rho_{e1} &= [\rho_{e1}^{(1ph)} + \rho_{e1}^{(2ph)}] \Omega_c e^{i\omega_l t}
\end{aligned} \tag{7.1}$$

Here  $\rho_{ee} - \rho_{11}$  and  $\rho_{22} - \rho_{11}$  are population differences,  $\gamma_{e1}$  and  $\gamma_{21}$  are coherence decay rates,  $\Omega_p$  and  $\Omega_c$  are the Rabi frequencies associated with the pump and cavity lasing transitions,  $\delta' = \delta - (\delta_{ac1} - \delta_{ac2})$  is the effective two-photon detuning with  $\delta_{ac1} = \frac{|\Omega_c|^2}{4\Delta}$ ,  $\delta_{ac2} = \frac{|\Omega_p|^2}{4\Delta}$  being the ac Stark shifts for  $\rho_{22} - \rho_{11} = \frac{1}{1+s}$  where  $s = \frac{\gamma_{21}}{\Gamma_{12}} \frac{|\Omega|^2}{\delta'^2 + \gamma_{21}^2}$ . The two-photon Rabi frequency is described as  $\Omega = -\frac{\Omega_p^* \Omega_c}{2\Delta}$ . In solving the density matrix equations, we utilize simplifying assumptions based on  $\Delta \gg \gamma_{ij}, \Gamma_{ij}, \delta$ . The imaginary part of the expression in square brackets is proportional to the gain/loss, the real part to index of refraction (107).

At this stage, a self-consistent solution to the lasing intensity can be found by equating the single-pass gain to the mirror transmission. For the relevant parameter space,  $\rho_{31}^{(2ph)}$  brings gain while  $\rho_{e1}^{(1ph)}$  brings absorption but can be ignored. The resulting equation has the form  $AI_p^{norm} = \left(1 + \frac{\delta'^2}{\gamma_{21}^2}\right)(1+s)$  with  $\delta'$  and  $s$  expressed in terms of the normalized pump and intracavity intensity parameters of  $I_p^{norm} = \frac{2|\Omega_p|^2}{\Gamma^2}$  and  $I_c^{norm} = \frac{2|\Omega_c|^2}{\Gamma^2}$ , respectively. Here,  $A$  is a constant depending on various system parameters (including  $\Delta$ ), and  $\Gamma = \Gamma_{31} + \Gamma_{32}$ . The results, for parameters chosen to represent the experiment, are shown in Fig. 7.7(b)&(d), indicating a bi-stable behavior for certain parameters, closely mimicking the experimental results. Shown in Fig. 7.7(c) are experimental results of the lasing profile as a function of pump frequency, conforming to the theoretical model. Additional measurements analogous to the ones in Fig. 7.7(a), but with  $\Delta = -450$  MHz indicate that, in this case, the roles of positive and negative are swapped, as expected.

Sharp transitions in physical observables in general serve as good sensors. An example is the superconducting transition edge sensor (106). Although blurred by data averaging, the transitions in Fig. 7.7(a) are very sharp in reality. Once understood better and engineered for stability, the edges may be used for measuring any disturbance that would cause atomic level shifts.

## 7.5 Conclusion

In summary, we have demonstrated a high finesse cavity Raman laser using cold  $^{87}\text{Rb}$  atoms as the gain medium. We observed continuous wave lasing in the atypical regime where single atoms can considerably affect the cavity field. Consequently, we discovered atypical lasing threshold behavior in the system causing jumps in lasing power, which results from a lasing-induced ac Stark shift for a single-photon detuning and a two-photon detuning. We also propose quantum mechanical and semi-classical models to explain the effect. We also measured the intermode laser linewidth as 80Hz.

Switching to a traveling wave configuration, in which two counter-propagating beams with the same spatial mode profile address the same atomic sample, RLGs with unprecedented bias and scale factor stability might be achieved. Furthermore, the gain medium properties can be engineered, providing additional enhancements. Although we have concentrated on continuous wave operation, pulsed mode can prove to be interesting. In the absence of the repump beam, with the turn-on of the pump beam, there will be a one-time superradiant emission into the cavity mode, creating a non-classical state of the radiation field. Further increases in output power have the potential to decrease the Schawlow-Townes limit to the sub-mHz regime. Lasers with subHz linewidths, tunable dispersion, and sufficient output powers to seed slave lasers may be well within reach.

# Chapter 8

## Conclusion

We built a high-finesse single-wavelength cavity system for achieving pseudospin squeezing and studying collective atom-cavity interactions. Using this cavity, we observed the collective normal mode splitting, providing evidence for a large collective cooperativity that can result in better spin squeezing. In the cQED system, we observed more than ten dB anti-spin-squeezing, but a spatially inhomogeneous atom-cavity coupling and inhomogeneous light shifts limit to have the same amount of spin-squeezing. We developed a dual-wavelength high-finesse cavity to have identical atom-cavity coupling. The dual-wavelength cavity system overcame the inhomogeneities and had longer atomic coherence, and it should result in a high degree of spin-squeezing.

In the dual-wavelength cavity, atoms optically trapped in the 1560 nm cavity lattices are in-phase with the 780 nm cavity probe at the cavity center. Using in-phase atom registration, spatially identical atom-cavity coupling has been realized, and the lifetime and coherence time of optically trapped atoms has been lengthened than in the single-wavelength cavity. In addition, in-phase atom registration enables us to regard all the trapped atoms as one macroscopic ensemble for studying macroscopic oscillation and self-trapping behavior.

Macroscopic self-trapping of two hyperfine levels due to the collective atom-cavity interaction has been observed at the mid-point region of the full atom-cavity shifts. The coherent evolution of the macroscopic ensemble of atoms can be interrupted by the probe-induced ac Stark shift of atomic clock states when the incident cavity photons becomes

resonant, and the cavity photon number is higher than the threshold. Using the same protocol of this experiment, we expect to achieve a macroscopic superposition state which has the potential to improve the precision of atom interferometers, but the state was not observed. In our simulation, the macroscopic superposition state can be generated, which has a short lifetime due to the measurement process of the cavity transmitted photons.

A free-running Raman laser has been demonstrated in our cavity system using  $^{87}\text{Rb}$  atoms as the gain medium. The laser has atypical lasing threshold behavior and has a tunable gain. The lasing threshold behavior results from a lasing-induced ac Stark shift, which can change the gain by varying the Raman lasing detuning and Raman pump frequency. Raman lasing with a narrow linewidth cavity shows the potential to achieve a narrow linewidth free-running laser. We observed the intermode-linewidth as low as 80 Hz. A robust narrow linewidth Raman laser can be applied for precision measurements. We can achieve anomalous dispersion by using two Raman pumps with two different frequencies, which could result in higher precision in ring laser gyroscopes due to better sensitivity to the variation of the cavity length.

## **Appendix A**

### **Cavity-lock servo circuits**

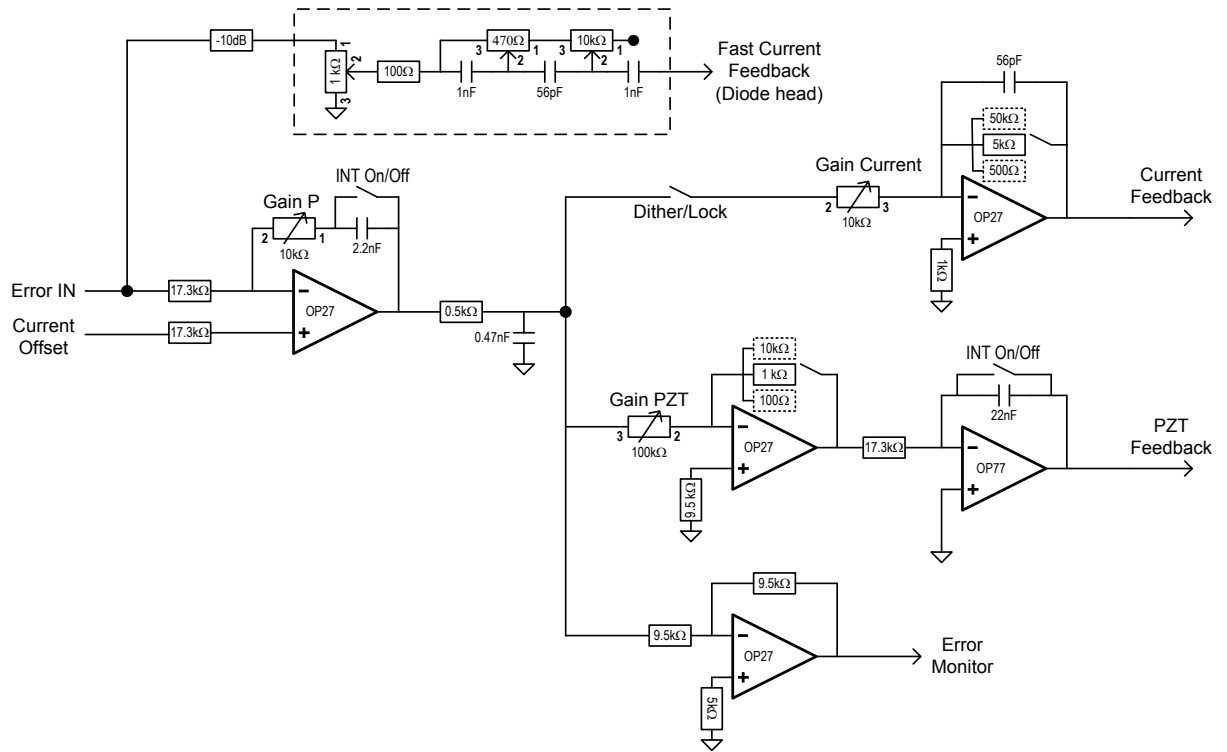


Figure A.1: Cavity-lock servo 1: With this cavity-lock servo, we can stabilize a master ECDL laser to a high-finesse reference cavity, and the linewidth of the master laser becomes narrower as much as the reference cavity's linewidth (Fig. 3.9, 3.12, 3.13).

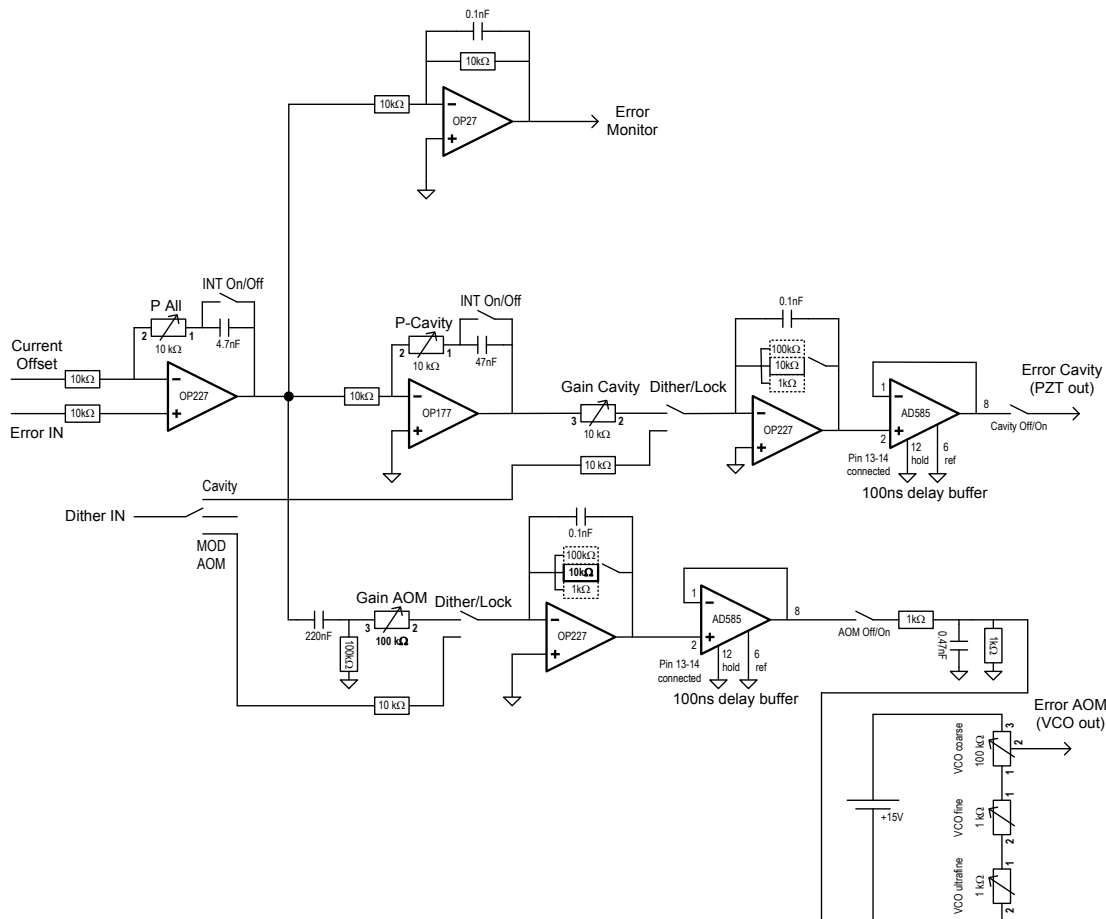


Figure A.2: Cavity-lock servo 2: This cavity-lock servo locks our science cavity to the low-noise probe light (Fig. 3.9) or stabilize the low-noise probe light to the science cavity (Fig. 3.12, 3.13).

# Bibliography

- [1] J. Lee, et al., and M. A. Kasevich, “Many-Atom Cavity-QED System with Identically Coupled Atoms,” (in progress).
- [2] J. Lee, et al., and M. A. Kasevich, “Macroscopic self-trapping of two hyperfine levels by collective atom-cavity interaction in a dual-wavelength cavity QED system,” (in progress).
- [3] G. Vrijsen, O. Hosten, J. Lee, S. Bernon, and M. A. Kasevich, “Raman Lasing with a Cold Atom Gain Medium in a High-Finesse Optical Cavity,” Phys. Rev. Lett. 107, 063904 (2011).
- [4] I. Teper, G. Vrijsen, J. Lee, and M. A. Kasevich, “Backaction noise produced via cavity-aided nondemolition measurement of an atomic clock state,” Phys. Rev. A **78**, 5, 051803 (2008).
- [5] A. K. Tuchman, R. Long, G. Vrijsen, J. Boudet, J. Lee, and M. A. Kasevich, “Normal-mode splitting with large collective cooperativity,” Phys. Rev. A **74**, 5, 053821 (2006).
- [6] R. Long, A. K. Tuchman, and M. A. Kasevich, “Multiple frequency modulation for low-light atom measurements in an optical cavity,” Opt. Lett. **32**, 17, 2502 (2007).
- [7] C. M. Caves, “Quantum-mechanical noise in an interferometer,” Phys. Rev. D **23**, 8, 1693 (1981).

- [8] D. J. Wineland, J. J. Bollinger, W. M. Itano, F. L. Moore, and D. J. Heinzen, "Spin squeezing and reduced quantum noise in spectroscopy," *Phys. Rev. A* **46**, 11, R6797 (1992).
- [9] M. Kitagawa and M. Ueda, "Squeezed spin states," *Phys. Rev. A* **47**, 6, 5138 (1993).
- [10] D. J. Wineland, J. J. Bollinger, W. M. Itano, and D. J. Heinzen, "Squeezed atomic states and projection noise in spectroscopy," *Phys. Rev. A* **50**, 1, 67 (1994).
- [11] J. Hald, J. L. Sorensen, C. Schori, and E. S. Polzik, "Spin Squeezed Atoms: A Macroscopic Entangled Ensemble Created by Light," *Phys. Rev. Lett.* **83**, 7, 1319 (1999).
- [12] A. Kuzmich, L. Mandel, and N. P. Bigelow, "Generation of Spin Squeezing via Continuous Quantum Nondemolition Measurement," *Phys. Rev. Lett.* **85**, 8, 1594 (2000).
- [13] D. Oblak, P. G. Petrov, C. L. Garrido Alzar, W. Tittel, A. K. Vershovski, J. K. Mikkelsen, J. L. Sorensen, and E. S. Polzik, "Quantum-noise-limited interferometric measurement of atomic noise: Towards spin squeezing on the Cs clock transition," *Phys. Rev. A* **71**, 4, 043807 (2005).
- [14] S. Chaudhury, G. A. Smith, K. Schulz, P. S. Jessen, "Continuous Nondemolition Measurement of the Cs Clock Transition Pseudospin," *Phys. Rev. Lett.* **96**, 4, 043001 (2006).
- [15] M. H. Schleier-Smith, I. D. Leroux, and V. Vuletic, "Squeezing the collective spin of a dilute atomic ensemble by cavity feedback," *Phys. Rev. A* **81**, 021804(R) (2010).
- [16] G. Santarelli, Ph. Laurent, P. Lemonde, A. Clairon, A. G. Mann, S. Chang, A. N. Luiten, and C. Salomon, "Quantum Projection Noise in an Atomic Fountain: A High Stability Cesium Frequency Standard," *Phys. Rev. Lett.* **82**, 23, 4619-4622 (1999).
- [17] A. Kuzmich, N. P. Bigelow, and L. Mandel, "Atomic quantum non-demolition measurements and squeezing," *Europhys. Lett.* **42**, 481 (1998).

- [18] A. Andre and M. D. Lukin, "Atom correlations and spin squeezing near the Heisenberg limit: Finite-size effect and decoherence," *Phys. Rev. A* **65**, 5, 053819 (2002).
- [19] A. S. Sorensen and K. Molmer, "Entangling atoms in bad cavities," *Phys. Rev. A* **66**, 2, 022314 (2002).
- [20] P. Berman, *Cavity Quantum Electrodynamics* (Academic Press, California, 1994).
- [21] G. Rempe, R. J. Thompson, R. J. Brecha, W. D. Lee, and H. J. Kimble, "Optical bistability and photon statistics in cavity quantum electrodynamics," *Phys. Rev. Lett.* **67**, 1727 (1991).
- [22] R. J. Thompson, G. Rempe, and H. J. Kimble, "Observation of normal-mode splitting for an atom in an optical cavity," *Phys. Rev. Lett.* **68**, 8, 1132 (1992).
- [23] G. S. Agarwal, "Vacuum-Field Rabi Splittings in Microwave Absorption by Rydberg Atoms in a Cavity," *Phys. Rev. Lett.* **53**, 18, 1732 (1984).
- [24] M. G. Raizen, L. A. Orozco, M. Xiao, T. L. Boyd, and H. J. Kimble, "Squeezed-state generation by the normal modes of a coupled system," *Phys. Rev. Lett.* **59**, 2, 198 (1987).
- [25] F. Bernardot, P. Nussenzveig, M. Brune, J. M. Raimond and S. Haroche, "Vacuum Rabi Splitting Observed on a Microscopic Atomic Sample in a Microwave Cavity," *Europhys. Lett.* **17**, 1, 33 (1992).
- [26] H. J. Kimble (editor P. Berman), *Cavity Quantum Electrodynamics, "Structure and Dynamics in Cavity Quantum Electrodynamics"* (Academic Press, California, 1994).
- [27] R. J. Brecha, L. A. Orozco, M. G. Raizen, M. Xiao, and H. J. Kimble, "Observation of oscillatory energy exchange in a coupled-atom-cavity system," *J. OSA B* **12**, 12, 2329 (1995).
- [28] H. Mabuchi, J. Ye, and H. J. Kimble, "Full observation of single-atom dynamics in cavity QED," *Appl. Phys. B* **68**, 6, 1095 (1999).

- [29] J. Ye, D. W. Verhaar, and H. J. Kimble, “Trapping of Single Atoms in Cavity QED,” *Phys. Rev. Lett.* **83**, 4987 (1999).
- [30] A. Boca, R. Miller, K. M. Birnbaum, A. D. Boozer, J. McKeever, and H. J. Kimble, “Observation of the Vacuum Rabi Spectrum for One Trapped Atom,” *Phys. Rev. Lett.* **93**, 23, 233603 (2004).
- [31] S. Deléglise, I. Dotsenko, C. Sayrin, J. Bernu, M. Brune, J.-M. Raimond, and S. Haroche, “Reconstruction of non-classical cavity field states with snapshots of their decoherence,” *Nature* **455**, 510 (2008).
- [32] Q. A. Turchette, C. J. Hood, W. Lange, H. Mabuchi, and H. J. Kimble, “Measurement of Conditional Phase Shifts for Quantum Logic,” *Phys. Rev. Lett.* **75**, 4710 (1995).
- [33] S. J. van Enk, H. J. Kimble, J. I. Cirac, and P. Zoller, “Quantum communication with dark photons,” *Phys. Rev. A* **59**, 2659 (1999).
- [34] L. M. Duan and H. J. Kimble, “Scalable Photonic Quantum Computation through Cavity-Assisted Interactions,” *Phys. Rev. Lett.* **92**, 12, 127902 (2004).
- [35] T. Chaneliere, D. N. Matsukevich, S. D. Jenkins, S. Y. Lan, T. A. B. Kennedy, and A. Kuzmich, “Storage and retrieval of single photons transmitted between remote quantum memories,” *Nature* **438**, 7069, 833 (2005).
- [36] K. S. Choi, H. Deng, J. Laurat, and H. J. Kimble, “Mapping photonic entanglement into and out of a quantum memory,” *Nature* **452**, 7183, 67 (2008).
- [37] J. Simon, H. Tanji, S. Ghosh and V. Vuletic, “Single-photon bus connecting spin-wave quantum memories,” *Nature Phys.* **3**, 11, 765-769 (2007).
- [38] C. J. Hood, T. W. Lynn, A. C. Doherty, A. S. Parkins and H. J. Kimble, “The Atom-Cavity Microscope: Single Atoms Bound in Orbit by Single Photons,” *Science* **287**, 1447 (2000).

- [39] S. Gleyzes, S. Kuhr, C. Guerlin, J. Bernu, S. Deleglise, U. B. Hoff, M. Brune, J.-M. Raimond, and S. Haroche, “Quantum jumps of light recording the birth and death of a photon in a cavity,” *Nature* **446**, 297 (2007).
- [40] A. Wallraff, D. Schuster, A. Blais, L. Frunzio, R.-S. Huang, J. Majer, S. Kumar, S. M. Girvin, and R. J. Schoelkopf, “Circuit quantum electrodynamics: Coherent coupling of a single photon to a Cooper pair box,” *Nature* **431**, 162 (2004).
- [41] M. Pelton, C. Santori, J. Vuckovic, B. Zhang, G. S. Solomon, J. Plant, and Y. Yamamoto, “Efficient source of single photons: A single quantum dot in a micropost microcavity,” *Phys. Rev. Lett.* **89**, 233602 (2002).
- [42] O. Painter, R. K. Lee, A. Scherer, A. Yariv, J. D. O’Brien, P. D. Dapkus and I. Kim, “Two-dimensional photonic band-gap defect mode laser,” *Science* **284**, 1819 (1999).
- [43] D. A. Steck, Rubidium 87 D Line Data (2001).
- [44] J. B. Fixler, G. T. Foster, J. M. McGuirk, and M. A. Kasevich, “Atom Interferometer Measurement of the Newtonian Constant of Gravity,” *Science* **315**, 5808, 74 (2007).
- [45] J. K. Stockton, Continuous quantum measurement of cold alkali-atom spins, Ph.D. thesis, California Institute of Technology (Pasadena, CA, 2007).
- [46] H. M. Wiseman and G. J. Milburn, “Interpretation of quantum jump and diffusion processes illustrated on the Bloch sphere,” *Phys. Rev. A* **47**, 1652 (1993).
- [47] A. Barchielli and V. P. Belavkin, “Measurements continuous in time and a posteriori states in quantum mechanics,” *J. Phys. A* **24**, 1495 (1991).
- [48] J. Dalibard et al., *Phys. Rev. Lett.* **68**, 580 (1992); C. W. Gardiner et al., *Phys. Rev. A* **46**, 4363 (1992); H. J. Carmichael, *An Open Systems Approach to Quantum Optics* (Springer, Berlin, 1993); N. Gisin and I. C. Percival, *J. Phys. A* **25**, 5677 (1992).
- [49] P. Marte, R. Dum, R. Taïeb, P. D. Lett, and P. Zoller, “Quantum wave function simulation of the resonance fluorescence spectrum from one-dimensional optical molasses,” *Phys. Rev. Lett.* **71**, 1335 (1993); P. Marte, R. Dum, R. Taïeb, and P. Zoller,

- "Resonance fluorescence from quantized one-dimensional molasses," Phys. Rev. A **47**, 1378 (1993); Y. Castin and K. Molmer, "Monte Carlo Wave-Function Analysis of 3D Optical Molasses," Phys. Rev. Lett. **74**, 3772 (1995).
- [50] N. Gisin and I. C. Percival, "Wave-function approach to dissipative processes: are there quantum jumps?" Phys. Lett. A **167**, 315 (1992); B. M. Garraway and P. L. Knight, "Comparison of quantum-state diffusion and quantum-jump simulations of two-photon processes in a dissipative environment," Phys. Rev. A **49**, 1266 (1994).
- [51] V. B. Braginski and F. Y. Khalili, Quantum Measurement, K. S. Thorne (Cambridge University Press, Cambridge, 1992); S. M. Tan and D. F. Walls, Phys. Rev. A **47**, 4663 (1993); T. Pfau et al., Phys. Rev. Lett. **73**, 1223 (1994).
- [52] M. Holland, S. Marksteiner, P. Marte, and P. Zoller, "Measurement Induced Localization from Spontaneous Decay," Phys. Rev. Lett. **76**, 3683 (1996).
- [53] T. Pellizzari, S. A. Gardiner, J. I. Cirac, and P. Zoller, "Decoherence, Continuous Observation, and Quantum Computing: A Cavity QED Model," Phys. Rev. Lett. **75**, 21, 3788 (1995).
- [54] C. W. Gardiner and P. Zoller, Quantum Noise (Springer, 2004).
- [55] S. M. Tan, "A computational toolbox for quantum and atomic optics," J. Opt. B: Quantum Semiclass. Opt. **1**, 424 (1999).
- [56] D. F. Walls and G. J. Milburn, Quantum Optics (Springer, 2008).
- [57] C. Monroe, W. Swann, H. Robinson, and C. Wieman, "Very cold trapped atoms in a vapor cell," Phys. Rev. Lett. **65**, 13, 1571-1574, (1990).
- [58] P. S. Jessen, C. Gerz, P. D. Lett, W. D. Phillips, S. L. Rolston, R. J. C. Spreeuw, and C. I. Westbrook, "Observation of quantized motion of Rb atoms in an optical field," Phys. Rev. Lett. **69**, 49 (1992).
- [59] Z. Hu and H. J. Kimble, "Observation of a single atom in a magneto-optical trap," Opt. Lett. **19**, 1888 (1994).

- [60] C. S. Adams, H. Lee, N. Davidson, M. Kasevich, and S. Chu, “Evaporative cooling in a crossed dipole trap,” *Phys. Rev. Lett.* **74**, 18, 3577 (1995)
- [61] S. Marksteiner, K. Ellinger, and P. Zoller, “Anomalous diffusion and Lévy walks in optical lattices,” *Phys. Rev. A* **53**, 3409 (1996); F. Bardou, J. P. Bouchaud, O. Emile, A. Aspect, and C. Cohen-Tannoudji, “Subrecoil laser cooling and Lévy flights,” *Phys. Rev. Lett.* **72**, 203 (1994).
- [62] J. McKeever, J. R. Buck, A. D. Boozer, A. Kuzmich, H.-C. Nägerl, D. M. Stamper-Kurn, and H. J. Kimble, “State-Insensitive Cooling and Trapping of Single Atoms in an Optical Cavity,” *Phys. Rev. Lett.* **90**, 133602 (2003).
- [63] A. Bertoldi, S. Bernon, T. Vanderbruggen, A. Landragin, and P. Bouyer, “In situ characterization of an optical cavity using atomic light shift,” *Opt. Lett.* **35**, 3769 (2010).
- [64] C. J. Foot, *Atomic Physics* (Oxford University Press, 2006).
- [65] T. W. Hodapp, C. Gerz, C. Furtelehner, C. I. Westbrook, W. D. Phillips and J. Dalibard, “Three-dimensional spatial diffusion in optical molasses,” *Appl. Phys. B* **60**, 135 (1995).
- [66] H. J. Metcalf and P. van der Straten, *Laser Cooling and Trapping* (Springer, 1999).
- [67] A. E. Siegman, *Lasers* (University Science Books, 1986).
- [68] A. Schoof, J. Grünert, S. Ritter, and A. Hemmerich, “Reducing the linewidth of a diode laser below 30 Hz by stabilization to a reference cavity with a finesse above  $10^5$ ,” *Opt. Lett.* **26**, 20, 1562 (2001).
- [69] R. W. P. Drever, J. L. Hall, F. V. Kowalski, J. Hough, G. M. Ford, A. J. Munley, and H. Ward, “Laser phase and frequency stabilization using an optical resonator,” *Appl. Phys. B* **31**, 2, 97 (1983).
- [70] R. G. DeVoe and R. G. Brewer, “Laser-frequency division and stabilization,” *Phys. Rev. A* **30**, 5, 2827 (1984).

- [71] J. Ye, L.-S. Ma, and J. L. Hall, "Ultrasensitive detections in atomic and molecular physics: demonstration in molecular overtone spectroscopy," *J. OSA B* **15**, 1, 6, (1998).
- [72] C. W. Oates, F. Bondu, R. W. Fox, and L. Hollberg, "A diode-laser optical frequency standard based on laser-cooled Ca atoms: Sub-kilohertz spectroscopy by optical shelving detection," *Euro. Phys. J. D* **7**, 449 (1999).
- [73] Eric D. Black, "An introduction to Pound-Drever-Hall laser frequency stabilization," *Am. J. of Phys.* **69**, 1, 79 (2001).
- [74] J. Ye and J. L. Hall, (Editor: Van Zee, R.D. and Looney, J.P.), *Cavity-Enhanced Spectroscopies, Absorption Detection at the Quantum Limit: Probing High-Finesse Cavities with Modulation Techniques* (Academic Press, San Diego, CA, 2002).
- [75] K. Numata, A. Kemery, and J. Camp, "Thermal-Noise Limit in the Frequency Stabilization of Lasers with Rigid Cavities," *Phys. Rev. Lett.* **93**, 25, 250602 (2004).
- [76] Y. Yamamoto and A. Imamoglu, *Mesoscopic Quantum Optics* (John Wiley and Sons, New York, 1999).
- [77] S. Leslie, N. Shenvi, K. R. Brown, D. M. Stamper-Kurn, and K. Birgitta Whaley, "Transmission spectrum of an optical cavity containing N atoms," *Phys. Rev. A* **69**, 4, 043805 (2004).
- [78] J. Gripp, S. L. Mielke, L. A. Orozco, and H. J. Carmichael, "Anharmonicity of the vacuum Rabi peaks in a many-atom system," *Phys. Rev. A* **54**, 5, R3746 (1996).
- [79] Y. Zhu, D. J. Gauthier, S. E. Morin, Q. Wu, H. J. Carmichael, and T. W. Mossberg, "Vacuum Rabi splitting as a feature of linear-dispersion theory: Analysis and experimental observations," *Phys. Rev. Lett.* **64**, 21, 2499 (1990).
- [80] M. G. Raizen, R. J. Thompson, R. J. Brecha, H. J. Kimble, and H. J. Carmichael, "Normal-mode splitting and linewidth averaging for two-state atoms in an optical cavity," *Phys. Rev. Lett.* **63**, 3, 240 (1989).

- [81] J. Klinner, M. Lindholdt, B. Nagorny, and A. Hemmerich, “Normal Mode Splitting and Mechanical Effects of an Optical Lattice in a Ring Cavity,” *Phys. Rev. Lett.* **96**, 2, 023002 (2006).
- [82] M. Tavis and F. W. Cummings, “Exact Solution for an N-Molecule, Radiation-Field Hamiltonian,” *Phys. Rev.* **170**, 2, 379 (1968).
- [83] S. Bize, P. Laurent, M. Abgrall, H. Marion, I. Maksimovic, L. Cacciapuoti, J. Grunert, C. Vian, F. Pereira dos Santos, P. Rosenbusch, P. Lemonde, G. Santarelli, P. Wolf, and A. Clairon, A. Luiten, M. Tobar, and C. Salomon, “Advances in atomic fountains,” *Comptes Rendus Physique*, **5**, 8, 829 (2004).
- [84] H. Mabuchi, and A. C. Doherty, *Science* **298**, 1372 (2002).
- [85] H. J. Kimble, *Physica Scripta* **T76**, 127 (1998).
- [86] R. Miller, T. E. Northup, K. M. Birnbaum, A. Boca, A. D. Boozer, and H. J. Kimble, *J Phys. B* **38**, S551 (2005).
- [87] M. H. Schleier-Smith, I. D. Leroux, and V. Vuletic, “States of an Ensemble of Two-Level Atoms with Reduced Quantum Uncertainty,” *Phys. Rev. Lett.* **104**, 073604 (2010).
- [88] I. D. Leroux, M. H. Schleier-Smith, and V. Vuletic, “Implementation of Cavity Squeezing of a Collective Atomic Spin,” *Phys. Rev. Lett.* **104**, 073602 (2010).
- [89] T. P. Purdy, D. W. C. Brooks, T. Botter, N. Brahms, Z. Y. Ma, and D. M. Stamper-Kurn, “Tunable Cavity Optomechanics with Ultracold Atoms,” *Phys. Rev. Lett.* **105**, 133602 (2010).
- [90] H. Tanji, S. Ghosh, J. Simon, B. Bloom, and V. Vuletic, *Phys. Rev. Lett.* **103**, 043601 (2009).
- [91] D. Meiser, J. Ye, D. R. Carlson, and M. J. Holland, “Prospects for a Millihertz-Linewidth Laser,” *Phys. Rev. Lett.* **102**, 163601 (2009).

- [92] F. Brennecke, T. Donner, S. Ritter, T. Bourdel, M. Köhl and T. Esslinger, *Nature* **450**, 268 (2007).
- [93] Y. Colombe, T. Steinmetz, G. Dubois, F. Linke, D. Hunger and J. Reichel, *Nature* **450**, 272 (2007).
- [94] T. P. Purdy, N. Brahms, D. W. C. Brooks, T. Botter, D. M. Stamper-Kurn, “Cavity-aided magnetic-resonance microscopy of atoms in optical lattices,” *Nature Physics* **7**, 604–607 (2011).
- [95] D. Leibfried, M. D. Barrett, T. Schaetz, J. Britton, J. Chiaverini, W. M. Itano, J. D. Jost, C. Langer and D. J. Wineland, “Toward Heisenberg-Limited Spectroscopy with Multiparticle Entangled States,” *Science* **304**, 1476 (2004).
- [96] M. Albiez, R. Gati, J. Folling, S. Hunsmann, M. Cristiani, and M. K. Oberthaler, “Direct Observation of Tunneling and Nonlinear Self-Trapping in a Single Bosonic Josephson Junction,” *Phys. Rev. Lett.* **95**, 010402 (2005).
- [97] S. Raghavan, A. Smerzi, S. Fantoni, and S. R. Shenoy, “Coherent oscillations between two weakly coupled Bose-Einstein Condensates: Josephson effects,  $\pi$ -oscillations, and macroscopic quantum self trapping,” arXiv:cond-mat/9706220v2 [cond-mat.soft] (1998).
- [98] J. Larson, and J. Martikainen, “Ultracold atoms in a cavity mediated double-well system,” *Phys. Rev. A* **82**, 033606 (2010).
- [99] G. S. Pati, M. Salit, K. Salit, and M. S. Shahriar, “Demonstration of a Tunable-Bandwidth White-Light Interferometer Using Anomalous Dispersion in Atomic Vapor,” *Phys. Rev. Lett.* **99**, 133601 (2007).
- [100] M. S. Shahriar, G. S. Pati, R. Tripathi, V. Gopal, M. Messall, and K. Salit, “Ultrahigh enhancement in absolute and relative rotation sensing using fast and slow light,” *Phys. Rev. A* **75**, 053807 (2007).
- [101] W. W. Chow, J. Gea-Banacloche, L. M. Pedrotti, V. E. Sanders, W. Schleich, and M. O. Scully, *Rev. of Mod. Phys.* **57**, 61 (1985).

- [102] P. Kumar and J. H. Shapiro, "Observation of Raman-shifted oscillation near the sodium D lines," *Opt. Lett.* **10**, 226 (1985).
- [103] L. Hilico, C. Fabre, and E. Giacobino, "Operation of a Cold-Atom Laser in a Magneto-Optical Trap," *Europhys. Lett.* **18**, 685 (1992).
- [104] W. Guerin, F. Michaud, and R. Kaiser, "Mechanisms for Lasing with Cold Atoms as the Gain Medium," *Phys. Rev. Lett.* **101**, 093002 (2008).
- [105] M. P. van Exter, S. J. M. Kuppens, and J. P. Woerdman, "Excess phase noise in self-heterodyne detection," *IEEE J. Quant. Electron.* **28**, 580 (1992).
- [106] A. E. Lita, A. J. Miller, and S. W. Nam, "Counting near-infrared single-photons with 95% efficiency," *Opt. Express* **16**, 3032 (2008).
- [107] R. W. Boyd, *Nonlinear Optics* (Academic Press, San Diego, CA, 2003).